SEARCH FOR A HEAVY GAUGE BOSON W' IN THE FINAL STATE WITH AN ELECTRON AND LARGE MISSING TRANSVERSE ENERGY IN PP COLLISIONS AT SQRT(S) = 7 TEV

A Dissertation

Presented to the Faculty of the Graduate School

of Cornell University

in Partial Fulfillment of the Requirements for the Degree of

Doctor of Philosophy

by

Darren Michael Puigh

January 2012

SEARCH FOR A HEAVY GAUGE BOSON W' IN THE FINAL STATE WITH AN ELECTRON AND LARGE MISSING TRANSVERSE ENERGY IN PP COLLISIONS AT SQRT(S) = 7 TEV

Darren Michael Puigh, Ph.D.

Cornell University 2012

A search for a heavy gauge boson W' has been conducted by the CMS experiment at the LHC in the decay channel with an electron and large transverse energy imbalance, $\not{E}_{\mathrm{T}}$, using proton-proton collision data corresponding to an integrated luminosity of 36 pb^{-1}. No excess above standard model expectations is seen in the transverse mass distribution of the electron-$\not{E}_{\mathrm{T}}$ system. Assuming standard-model-like couplings and decay branching fractions, a W' boson with a mass less than 1.32 TeV/c^2 is excluded at the 95% confidence level.

BIOGRAPHICAL SKETCH

Darren Puigh was born on September 23, 1982 in Richland, Washington. He graduated from Hanford High School in 2001 as co-valedictorian. After high school, Darren attended the University of Washington in Seattle. While searching for a major, his curiosity about the world quickly drew him to the field of Physics. Also interested in topics related to astrophysics and cosmology, Darren decided to pursue a double major in both Physics and Astronomy. He received a Bachelor of Science degree in both fields in 2005, graduating *summa cum laude*.

In 2005, Darren began his graduate career in the physics Ph.D. program at Cornell University. After taking two years of intensive course work, he joined the CMS group at Cornell in the Spring of 2007. Initially, Darren spent the majority of his time working on corrections to missing transverse energy, and his physics research was centered on searches for supersymmetry using events with leptons.

In October of 2008, he moved to France to work at CERN. This allowed him close access to the CMS detector and a large number of CMS colleagues. During his time at CERN, Darren took many data quality monitoring shifts, he worked on data quality monitoring of the level-1 hardware trigger, and he contributed to a search for new heavy gauge bosons W' (the subject of this dissertation). The search was published in early 2011.

In February of 2011, Darren returned to Ithaca, NY, to focus on writing this dissertation and applying for postdoctoral research positions in high energy particle physics. After graduating from Cornell University, Darren Puigh will continue his work with the CMS collaboration at the Ohio State University in Columbus, Ohio.

To those who cannot help but ask the difficult questions

ACKNOWLEDGEMENTS

The research that I present in this dissertation owes itself to a great number of people. Without their work, help, and support, this dissertation would not have been possible. It is as strong as it is thanks to those people, and I want to acknowledge them all here. Without doubt, I will forget to mention someone important. If that person is you, I apologize for my poor memory. Any mistakes contained in this dissertation are completely my own.

My research could not have been done without the decades of work by thousands of experts who built, maintained, and operated the CMS detector. Being a part of such a large and helpful collaboration was critical to my success. Not only did my collaborators lay the groundwork for me, there were many experts who went out of their way to answer my questions. In addition to the people of CMS, none of the data used in my analysis would have been possible without the scientists, engineers, and technicians behind the LHC. The great success and fast accomplishments of this machine were critical for all of the scientific content coming from the collider experiments at CERN.

In addition, I would like to thank the particle physics faculty at Cornell University for their support, particularly Anders Ryd, Lawrence Gibbons, and Ritchie Patterson. To Julia Thom and Werner Sun, I really appreciate all the feedback and help you have both provided me over the years. I owe many thanks to Jim Alexander. Not only did he go out of his way to make me feel welcome in the group, but he also helped teach me about the best way to get real science done in our field, and he played an essential role in my obtaining a postdoctoral position after graduate school.

On a more personal note, I would like to thank my advisor, Peter Wittich, for being my mentor since joining the CMS group at Cornell. He understood what

sort of collaborating worked best with me and how different advising styles were important at different times. Peter would never patronize or talk down to me. He would always make time for me if I needed it. There were times when I felt like I was asking stupid questions, and he would patiently help lead me in the right direction. He has always treated me with respect, as a collaborator. Over time, this collaboration between us only strengthened. Conducting novel physics research can be challenging, but the guidance I received from Peter has helped to prepare me for a future career in this field. I can hardly imagine a better research advisor.

For our CMS analysis on the search for a heavy gauge boson W', Peter and I did not work on this analysis alone. We were able to get the CMS analysis approved and published thanks to the help of Kerstin Hoepfner, Martina Malberti, and Federico De Guio.

Many people helped make my time spent in Europe easier, more enjoyable, and more fruitful. I want to thank Lorenzo, Avi, Ben, Josh, Evonne, Jimmy, Tia, Emmanuele, Imai, Souvik, and Xiaohang. I will never forget the time spent in the cafe above our office, the potlucks, the Monday margherita pizza lunches, the climbing on roofs, the going through basements, the evening movie sessions, the many great conversations, the festivals by the lake, and the many other experiences we shared while I was living in St. Genis-Pouilly, France. These all contributed to my fond memories of living at CERN.

Apart from those at CERN, many Cornell graduate students assisted me while I was in Ithaca. Flip, you were of immense help when going through the theory of new gauge bosons; I learned more about model building and what it is like to be a phenomenologist than I expected. I also want to thank the HEP graduate students at Cornell: Don, Stephen, Yao, Nic, Xin, and Gala. Further-

more, I would like to extend many thanks to Carolyn, Sheryl, Sarah, Ethan, Sarah, Chris, Jen, and Dave who made me feel welcome in Ithaca after returning from CERN. I also want to thank Yvonne for always lending a sympthatic ear. I extend my deepest thanks to Mohammad and Erin; your friendship with me has helped me in every aspect of my life.

I also want to thank my family for their love and support while I was pursuing my Ph.D.: Barb, Ray, Chris (+ family), and Julie (+ family). Most of all, I owe thanks to my wife Tien. Throughout it all, she has remained devoted and in love with me, even though my graduate career has introduced great stress and sometimes placed the two of us on different continents. Her patience with me is always inspiring.

TABLE OF CONTENTS

LIST OF TABLES

LIST OF FIGURES

CHAPTER 1

INTRODUCTION

As we look up at the sky and into space, what do we see? There are planets in our solar system orbiting around the sun. Our solar system, in turn, orbits around the center of our galaxy, the Milky Way. Looking further, we can see galaxies, clusters of galaxies, and so on. Due to the finite speed that light travels, seeing an object further away means that you are seeing it earlier in time. For example, consider an object that is one light-year away (1 ly $\sim 9.5 \times 10^{12}$ km). Since it took the light from the object a year to get to us, we are actually seeing how it looked one year ago. As we look deeper into space, we are seeing the Universe at earlier and earlier times.

It is also interesting to note that the temperature of outer space is not zero. This is due to the background radiation (heat) remaining from the Big Bang. The current black-body temperature of this radiation is 2.7 K, and the temperature continues to decrease as the Universe expands. Running the clock backwards, the Universe was a warmer place at earlier times. However, there is a limit to how far back we can directly look. There is a veil of radiation from 13.7 billion years ago, when the Universe was 380,000 years old and at a temperature of 3000 K. Before this time, the Universe was so hot that atoms did not have a chance to form; space was a plasma of electrons, photons, and baryons, and the Universe was opaque. When the Universe expanded and cooled enough for electrons and protons to form atoms, the photons were free to travel through space. These photons are the cosmic microwave background radiation that we see today.

To investigate earlier times, we must create conditions that are hot, dense,

and energetic. By probing higher energies, we are peering further back into the history of the Universe. Indeed, using the famous Einstein relation[1] $E = mc^2$, we see that energy and mass are two sides of the same coin; mass can transform into energy, and energy can transform into mass. The more energy that we have available, the more massive particles we can create.

Although nature does provide us with ultra high energy particles from outer space, we choose to study more controlled environments and create the high energy particles ourselves in the laboratory. We accomplish this by building ever larger particle accelerators. The idea is simple: accelerate particles to higher and higher energy, collide the particles together, and study what comes out of the wreckage. This has been the *modus operandi* for particle physics since the early 20^{th} century.

The observations at particle colliders over the past century have been described by the modern theory of particle physics, called the standard model. The standard model is a quantum field theory that describes the fundamental constituents of matter and the interactions which mediate the dynamics of those fundamental particles. The fundamental particles of the standard model come in two different varieties: (1) spin-$\frac{1}{2}$ fermions that describe the matter, such as quarks and leptons, and (2) integer spin bosons, such as the spin-1 gauge bosons that mediate the strong, weak, and electromagnetic forces.

So far, the standard model has stood up to intense experimental scrutiny. However, as Newtonian dynamics are the low speed limit of special relativity, the standard model may be a low energy limit of some new theory. There are

[1] This is the energy of a massive particle in its rest-frame. In general, the energy of a particle (E) is related to its momentum (p) and mass (m) by the speed of light (c) and the relation: $E^2 = p^2c^2 + m^2c^4$.

many possibilities: supersymmetry, extra dimensions, hidden valleys, new particles, and new forces. This issue is more relevant now than it has ever been in the past, because we have entered the era of the Large Hadron Collider. Currently the world's highest energy collider, this machine is exploring an energy regime we have never before been able to probe in the lab. It is an amazing age of exploration. In truth, no one knows what we may find, which is part of what makes it so exciting.

In this dissertation, we present a search for physics beyond the standard model in the form of new, heavy gauge bosons. Chapter 2 provides a review of the standard model in greater detail and gives some theoretical motivations for searching for these new particles. Chapter 3 describes the Large Hadron Collider machine that produces the proton collisions and the Compact Muon Solenoid detector that records those collisions. Chapter 4 describes work done to ensure the data are suitable to use in our physics analyses. Chapter 5 discusses the data and Monte Carlo simulation used for this study. Chapter 6 describes the reconstruction of physics objects relevant for this analysis. Chapter 7 details the search procedure, Chapter 8 gives the results of the search, and Chapter 9 presents the conclusion.

CHAPTER 2

THE STANDARD MODEL AND BEYOND

2.1 The Standard Model of Particle Physics

In this Section, we give an overview of the standard model of particle physics, the theory describing the electromagnetic, weak, and strong interactions.

2.1.1 Particles and Forces

How can we best describe the world of particle physics? In nature, we see many particles and the forces that act on them. The most obvious force in our daily lives is gravity. It is responsible for objects falling to the ground on Earth and the motions of the planets around the sun. The next most familiar force is electromagnetism. It is the long-range interaction between charged particles. Along with gravity, it is responsible for nearly all the phenomena we experience in daily life. Gravity pulls us toward the center of the Earth and electromagnetism (in the form of the electrostatic repulsion between our feet and the floor) pushes back; the two keep us on the surface of the Earth. The two other forces, the strong and the weak force, are less familiar to us, but they are no less important. The strong force holds the quarks and gluons together inside of the proton and neutron, and it also binds protons and neutrons together to form atomic nuclei. The weak force is responsible for radioactive decay and provides the mechanism for hydrogen fusion in stars.

In the standard model, the fundamental matter particles are spin-$\frac{1}{2}$ fermions

Table 2.1: The fermions of the standard model. Mass values and limits taken from the Particle Data Group [1]. Quark masses are given in the $\overline{\text{MS}}$ scheme. The top quark mass is from direct observation of top quark decay events. Cosmological measurements put a limit on the total mass of neutrinos, $\sum m_\nu \leq 0.58$ eV (95% CL) [2].

Fermions	Generation			Charge (e)
	1	2	3	
quarks	u	c	t	$+\frac{2}{3}$
	$2.49^{+0.81}_{-0.79}$ MeV	$1.27^{+0.07}_{-0.09}$ GeV	$172.0 \pm 0.9 \pm 1.3$ GeV	
	d	s	b	$-\frac{1}{3}$
	$5.05^{+0.75}_{-0.95}$ MeV	101^{+29}_{-21} MeV	$4.19^{+0.18}_{-0.06}$ GeV	
leptons	ν_e	ν_μ	ν_τ	0
	< 2 eV	< 0.19 MeV	< 18.2 MeV	
	e	μ	τ	-1
	0.5110 MeV	105.6 MeV	1.777 GeV	

(they obey Fermi-Dirac statistics) and come in two different varieties: leptons and quarks. The most common and well-known lepton is the electron. It is stable, and the magnitude of its electrical charge is used as the standard measure of charge for particles ($q_e = -1.60217646 \times 10^{-19}$ coulombs). The other charged leptons are the muon (μ) and the tau (τ). They are more massive versions of the electron and, as such, are unstable (they decay via the weak interaction). In addition to the charged leptons, there are also three electrically neutral leptons called neutrinos. These particles only interact via the weak force, and there is one neutrino associated with each charged lepton: ν_e, ν_μ, ν_τ.

The quarks come in six different flavors: up (u), down (d), charm (c),

strange (/s/), top (t), and bottom (b). Like leptons, the quarks come in three different generations. Although we do not know why there are three generations (and not more or less), we do know that the number of quark and lepton generations must be the same to cancel anomalies in the standard model. The major difference between leptons and quarks is that quarks can interact via the strong force while leptons cannot. They carry both electrical charge ($q = \frac{2}{3}e$ or $-\frac{1}{3}e$) and color charge (red, green, blue)[1]. Although quarks are colored, we do not observe free colored objects. The quarks form bound states that are color singlets; we call these bound states hadrons. The bound states can be made of quark-antiquark pairs ($q_i\bar{q}_i$) or three quarks ($q_iq_jq_k$). The former are bosons called mesons, while the latter are fermions called baryons. Most hadrons are unstable and decay very quickly. One notable exception is the proton, comprising of two up quarks and one down quark, that has a mean life larger than 10^{31} years (many times the age of the Universe) [1]. A brief summary of the properties of the quarks and leptons of the standard model is given in Tab. 2.1.

As stated in the previous chapter, the standard model describes three of the fundamental interactions of nature: the electromagnetic, the strong, and the weak interactions. Gravitational interactions are not a part of the theory. The forces are due to the production and exchange of gauge bosons. Gauge bosons are spin-1 bosons (they obey Bose-Einstein statistics). The carrier of the electromagnetic interaction is the photon (γ), which is massless. Similar to gravity, electromagnetism is a long-range interaction. For the strong interaction, the carrier is the gluon (g). Although the gluon is massless, it carries color charge (in contrast, the photon does not carry electric charge). Since the gluon is colored, the strong interaction is confining (we do not observe colored objects), and it is

[1]Color is a convenient name for the additional quantum number that quarks carry; it has no relation to our visual perception of color.

Table 2.2: The gauge bosons of the standard model. Mass values are taken from the Particle Data Group [1]. Here, charge refers to the electromagnetic charge.

Force carriers	Symbol	Interaction	Charge	Mass (GeV)
photon	γ	Electromagnetic	0	0
gluon	g	Strong	0	0
W boson	$W^{\pm}$	Weak	± 1	80.399 ± 0.023
Z boson	Z	Weak	0	91.1876 ± 0.0021

a short-range interaction. The carriers of the weak interaction are the $W^{\pm}$ and Z bosons, which are both massive ($\sim$ 100 GeV). Therefore, it is a short range interaction. We also observe that the $W^{\pm}$ bosons only interact with left-handed particles[2]. For this reason, the weak interaction violates parity symmetry (maximally), and it violates CP symmetry (the product of charge conjugation and parity). The properties of the standard model gauge bosons are given in Tab. 2.2.

2.1.2 Mathematical Formulation

We can describe the standard model as a quantum field theory in four-dimensional Minkowski space. We work in the language of "action" and "Lagrangian". The action is given by

$$\mathcal{S} = \int d^4x \, \mathcal{L}\left[\phi(x), \partial_\mu \phi(x)\right] \tag{2.1}$$

[2]Note that we are not being careful here about the distinction between chirality and helicity. For massless particles, the two are identical. For massive particles, a left-chiral particle could have either left- or right-helicity, depending on your reference frame relative to the particle. To be exact, we say that the W boson couples to left-chiral fermions. In the rest of the text, we will stick to the notation of left- and right-handedness.

where d^4x is the integration measure in 4d Minkowski space, $\mathcal{L}$ is the Lagrangian density (hereafter referred to as the Lagrangian), and ϕ(x) is a generic field. Particles are the quantizations (or excitations) of these fields. The Lagrangian summarizes the dynamics of the system. Requiring that the action remain stationary ($\delta\mathcal{S} = 0$) as one varies the fields leads to the equations of motions

$$\partial_\mu \left(\frac{\partial \mathcal{L}}{\partial(\partial_\mu \phi)} \right) = \frac{\partial \mathcal{L}}{\partial \phi} \tag{2.2}$$

for each field ϕ.

What are the symmetries of the Lagrangian of the standard model? Specifically, what is the internal symmetry group under which the standard model is invariant? The structure of the standard model is based upon the gauge group

$$SU(3)_C \otimes SU(2)_L \otimes U(1)_Y \tag{2.3}$$

where C denotes color (the "charge" of the strong interaction), L refers to left-handed fields (to indicate the parity-violating nature of the weak interaction), and Y denotes hypercharge. The gauge group determines the forces. For example, the $SU(3)_C$ group corresponds to the strong force. There are three generations (or flavors) of fermions, and each generation consists of five representations of the gauge group of (2.3):

$$L_L^i(1,2)_{-1/2}, \quad E_R^i(1,1)_{-1}, \quad Q_L^i(3,2)_{1/6}, \quad U_R^i(3,1)_{2/3}, \quad D_R^i(3,1)_{-1/3} \tag{2.4}$$

where the first and second numbers in parentheses indicates the $SU(3)_C$ and $SU(2)_L$ representation of the field, respectively. The first subscript indicates whether it is a left- or right-handed fermion, and the second index is the $U(1)_Y$ hypercharge. The i superscript is the flavor index indicating the generation,

with $i = 1, 2, 3$. In addition to Eq. (2.4), the standard model contains a scalar field, $\phi(1,2)_{1/2}$. This field is responsible for the spontaneous symmetry breaking (SSB) of the electroweak interaction

$$SU(2)_L \otimes U(1)_Y \xrightarrow{SSB} U(1)_{\text{EM}} \tag{2.5}$$

into the standard electromagnetic interaction with which we are familiar. The Higgs boson is the particle excitation of this hypothetical field, and it serves as an agent by which the weak gauge bosons ($W^{\pm}$ and Z) and the fermions (quarks and leptons) gain their mass. For the rest of this section, we focus on the electroweak sector of the standard model and the process of spontaneous symmetry breaking. The full Lagrangian of the standard model is given in Sec. A.

Before electroweak symmetry breaking, we can obtain gauge invariance of the standard model with respect to a local $SU(2)_L \otimes U(1)_Y$ symmetry by exchanging partial derivatives (∂_μ) in the Lagrangian with the covariant derivative

$$D_\mu = \partial_\mu - ig_L W_\mu^a T_a - ig_Y B_\mu Y \tag{2.6}$$

where the first term is the standard partial derivative, and the constants g_L and g_Y are the gauge couplings of the $SU(2)_L$ and $U(1)_Y$ groups, respectively. There are four vector fields associated with the $SU(2)_L \otimes U(1)_Y$ group in Eq. (2.6). Three of them are associated with the $SU(2)_L$ group: W_μ^1, W_μ^2, and W_μ^3. The vector field B_μ is associated with the $U(1)_Y$ group. There is one vector field for each of the group generators. For singlets of $SU(2)_L$, the generators are zero, $T_a = 0$. For doublets of $SU(2)_L$, $T_a = \frac{\sigma_a}{2}$, where σ_a are the Pauli matrices. There is a single generator for $U(1)_Y$, Y, which is a commuting number. We have the following commutation relations:

$$[T_a, T_b] = i\epsilon_{abc} T_c, \qquad [T_a, Y] = 0. \tag{2.7}$$

Table 2.3: The fermions of the standard model and their representations.

Field	$SU(3)_C$	$SU(2)_L$	T_3	Y	Q
$Q_L = \begin{pmatrix} u_L \\ d_L \end{pmatrix}$	**3**	**2**	$\begin{pmatrix} \frac{1}{2} \\ -\frac{1}{2} \end{pmatrix}$	$\frac{1}{6}$	$\begin{pmatrix} \frac{2}{3} \\ -\frac{1}{3} \end{pmatrix}$
u_R	**3**	**1**	0	$\frac{2}{3}$	$\frac{2}{3}$
d_R	**3**	**1**	0	$-\frac{1}{3}$	$-\frac{1}{3}$
$L_L = \begin{pmatrix} \nu_L \\ e_L \end{pmatrix}$	**1**	**2**	$\begin{pmatrix} \frac{1}{2} \\ -\frac{1}{2} \end{pmatrix}$	$-\frac{1}{2}$	$\begin{pmatrix} 0 \\ -1 \end{pmatrix}$
e_R	**1**	**1**	0	-1	-1
$\phi = \begin{pmatrix} \phi^+ \\ \phi^0 \end{pmatrix}$	**1**	**2**	$\begin{pmatrix} \frac{1}{2} \\ -\frac{1}{2} \end{pmatrix}$	$\frac{1}{2}$	$\begin{pmatrix} 1 \\ 0 \end{pmatrix}$

The actions of the generators on the fermion fields are determined by the representations and hypercharge assignments given in Eq. (2.4). Explicitly, their actions on the lepton fields are

$$T_a L_L^i = \frac{\sigma_a}{2} L_L^i, \qquad T_a E_R^i = 0, \qquad Y L_L^i = -\frac{1}{2} L_L^i, \qquad Y E_R^i = -E_R^i \tag{2.8}$$

with similar expressions for the quark fields. The matter fields, their representations, and their quantum numbers are given explicitly in Tab. 2.3.

We can write down the Lagrangian of the electroweak sector of the standard model before spontaneous symmetry breaking as the sum of four components:

$$\mathcal{L}_{\text{EWK}} = \mathcal{L}_{\text{gauge}} + \mathcal{L}_{\text{fermion}} + \mathcal{L}_{\text{higgs}} + \mathcal{L}_{\text{yukawa}}. \tag{2.9}$$

The first term, $\mathcal{L}_{\text{gauge}}$, describes the interactions of the gauge bosons

$$\mathcal{L}_{\text{gauge}} = -\frac{1}{4} W_{\mu\nu}^a W_a^{\mu\nu} - \frac{1}{4} B_{\mu\nu} B^{\mu\nu} \tag{2.10}$$

where the field strength tensors are given by

$$\begin{aligned} W^a_{\mu\nu} &= \partial_\mu W^a_\nu - \partial_\nu W^a_\mu + g_L \epsilon^{abc} W^b_\mu W^c_\nu \\ B_{\mu\nu} &= \partial_\mu B_\nu - \partial_\nu B_\mu \end{aligned} . \tag{2.11}$$

The second term in Eq. (2.9) is the kinetic term for fermions

$$\mathcal{L}_{\text{fermion}} = \sum_k i\bar{\psi}_k \gamma^\mu D_\mu \psi_k \tag{2.12}$$

where the sum runs over the 5 fermion fields given in Eq. (2.4). The third term in Eq. (2.9) describes the Higgs field

$$\mathcal{L}_{\text{higgs}} = \left|D_\mu \phi\right|^2 - \lambda\left(|\phi|^2 - \frac{\upsilon^2}{2}\right)^2 \tag{2.13}$$

where $\upsilon^2 > 0$. Finally, the fourth term in Eq. (2.9) gives the Yukawa interaction between the Higgs field and the fermion fields

$$\mathcal{L}_{\text{yukawa}} = -\lambda^\ell_{ij} \bar{L}^i_L E^j_R \phi - \lambda^u_{ij} \bar{Q}^i_L D^j_R \phi - \epsilon_{\text{ab}} \lambda^d_{ij} \bar{Q}^{i\text{a}}_L U^j_R \phi^{\dagger\text{b}} + h.c. \tag{2.14}$$

where the constants λ_{ij} are the strength of coupling between the Higgs and fermion fields. They are not related to λ in Eq. (2.13).

The process of mass generation begins with the gauged Lagrangian of the Higgs sector. The single scalar field in the standard model is an $SU(2)_L$ doublet that can be written as two complex scalar component fields ϕ^+ and ϕ^0:

$$\phi = \begin{pmatrix} \phi^+ \\ \phi^0 \end{pmatrix} = \frac{1}{\sqrt{2}} \begin{pmatrix} \phi_1 + i\phi_2 \\ \phi_3 + i\phi_4 \end{pmatrix} \tag{2.15}$$

where the superscripts (+ and 0) on the fields indicate their electromagnetic charge, and the fields $\phi_{1\ldots4}$ are real-valued. From Eq. (2.13), we can see that the

scalar field acquires a non-zero vacuum expectation value (VEV). We use the freedom of $SU(2)_L$ rotations to give a VEV to the neutral component of ϕ

$$\langle \phi_1 \rangle = \langle \phi_2 \rangle = \langle \phi_4 \rangle = 0, \qquad \langle \phi_3 \rangle = \upsilon, \tag{2.16}$$

in order to leave electromagnetism ($U(1)_{\text{EM}}$) unbroken. This is an arbitrary choice to make, but it is a convenient definition given that we want the simplest form of the Lagrangian to describe the electromagnetic interaction. Expanding the Lagrangian about the minimum of the scalar potential, we introduce a fluctuating real-valued field $h(x)$, where $\langle h(x) \rangle = 0$. Then, the scalar field can be written as

$$\phi(x) = \frac{1}{\sqrt{2}} \begin{pmatrix} 0 \\ \upsilon + h(x) \end{pmatrix} \tag{2.17}$$

where we identify $h(x)$ as the standard model Higgs field. Using Eq. (2.6), Eq. (2.17), and the $SU(2)_L$ and $U(1)_Y$ generators, we determine the action of the covariant derivative on the scalar field to be

$$\begin{aligned} D_\mu \phi &= \frac{1}{\sqrt{2}} \begin{pmatrix} \partial_\mu - \frac{i}{2}\left(g_L W_\mu^3 + g_Y B_\mu\right) & -\frac{i g_L}{2}\left(W_\mu^1 - i W_\mu^2\right) \\ -\frac{i g_L}{2}\left(W_\mu^1 + i W_\mu^2\right) & \partial_\mu + \frac{i}{2}\left(g_L W_\mu^3 - g_Y B_\mu\right) \end{pmatrix} \begin{pmatrix} 0 \\ \upsilon + h \end{pmatrix} \\ &= \frac{1}{\sqrt{2}} \begin{pmatrix} -\frac{i g_L}{2}\left(W_\mu^1 - i W_\mu^2\right)(\upsilon + h) \\ \partial_\mu h + \frac{i}{2}\left(g_L W_\mu^3 - g_Y B_\mu\right)(\upsilon + h) \end{pmatrix}. \end{aligned} \tag{2.18}$$

If we then expand $\mathcal{L}_{\text{higgs}}$ in Eq. (2.13) using Eq. (2.17) and Eq. (2.18), we get

$$\begin{aligned} \mathcal{L}_{\text{higgs}} =& \frac{g_L^2 \upsilon^2}{8}\left(W_\mu^1 + W_\mu^2\right)\left(W^{1\,\mu} - W^{2\,\mu}\right)\left(1 + \frac{h}{\upsilon}\right)^2 \\ &+ \frac{\upsilon^2}{8}\left(g_L W_\mu^3 - g_Y B_\mu\right)\left(g_L W^{3\,\mu} - g_Y B^\mu\right)\left(1 + \frac{h}{\upsilon}\right)^2. \\ &+ \frac{1}{2}\left(\partial_\mu h\right)\left(\partial^\mu h\right) - \lambda \upsilon^2 h^2 - \lambda \upsilon h^3 - \frac{\lambda}{4} h^4 \end{aligned} \tag{2.19}$$

Next, we make the following mass eigenstate field definitions

$$\begin{aligned} W_\mu^\pm &= \frac{1}{\sqrt{2}}\left(W_\mu^1 \mp iW_\mu^2\right) \\ Z_\mu &= \frac{1}{\sqrt{g_L^2+g_Y^2}}\left(g_L W_\mu^3 - g_Y B_\mu\right) \\ A_\mu &= \frac{1}{\sqrt{g_L^2+g_Y^2}}\left(g_Y W_\mu^3 + g_L B_\mu\right) \end{aligned} \tag{2.20}$$

which we can substitute into Eq. (2.19) to obtain

$$\mathcal{L}_{\text{higgs}} = \left(m_w^2 W_\mu^- W^{+\,\mu} + \frac{m_Z^2}{2} Z_\mu Z^\mu\right)\left(1+\frac{h}{\upsilon}\right)^2 + \frac{1}{2}\left(\partial_\mu h\right)^2 - \frac{m_h^2}{2}h^2 - \frac{\xi}{3!}h^3 - \frac{\eta}{4!}h^4 \tag{2.21}$$

where

$$\begin{aligned} m_w^2 = \frac{1}{4}g_L^2\upsilon^2, \qquad m_Z^2 = \frac{1}{4}\left(g_L^2+g_Y^2\right)\upsilon^2, \\ m_h^2 = 2\lambda\upsilon^2, \qquad \xi = 6\lambda\upsilon = \frac{3m_h^2}{\upsilon}, \qquad \eta = 6\lambda = \frac{3m_h^2}{\upsilon^2}. \end{aligned} \tag{2.22}$$

There is no term that looks like $m_A^2 A_\mu A^\mu$, indicating that the A_μ field remains massless ($m_A^2 = 0$). We identify the A field as the electromagnetic field with its massless photon. The gauge bosons $W^\pm$ and Z have gained mass due to spontaneous symmetry breaking. These are the gauge bosons of the weak interaction. If we define the Weinberg angle, θ_W, as

$$\tan\theta_W \equiv \frac{g_Y}{g_L} \tag{2.23}$$

then we have a rotation for the neutral gauge bosons from the interaction basis (W^3 and B) to the mass basis (Z and A)

$$\begin{pmatrix} Z \\ A \end{pmatrix} = \begin{pmatrix} \cos\theta_w & -\sin\theta_w \\ \sin\theta_w & \cos\theta_w \end{pmatrix}\begin{pmatrix} W^3 \\ B \end{pmatrix}. \tag{2.24}$$

What happened to scalar fields $\phi_{1,2,4}$ in Eq. (2.15)? These correspond to the three massless Goldstone bosons that we gauged away using our freedom of $SU(2)$ rotations. From Goldstone's theorem, we know that there is one Goldstone boson for each of the generators that are broken (e.g., three in the case of $SU(2)$). These three scalar particles became the longitudinal components of the W^+, W^-, and Z fields. In this way, it is often said that these gauge bosons "eat" the Goldstone bosons to gain mass. The scalar Higgs boson also has a mass. For all of the bosons, their masses are proportional to the non-zero VEV, v.

The quarks and leptons also get their mass through their coupling with the Higgs. For the fermions, the coupling comes through their Yukawa interaction in Eq. (2.14). Focusing on the leptonic part of the Yukawa Lagrangian, the only possible coupling is

$$\mathcal{L}_{\text{yukawa,lep}} = -\lambda_\ell^{ij} \bar{L}_L^i E_R^j \phi + h.c. \tag{2.25}$$

Since there are no right-handed neutrinos, we can diagonalize this coupling in flavor space by introducing the unitary matrices U and W and representing λ_ℓ as

$$\lambda_\ell = U D_\ell W^\dagger \tag{2.26}$$

At the same time, we can eliminate the U and W matrices by redefining the fields as

$$e_L^i \to U^{ij} e_L^j, \qquad \nu_L^i \to U^{ij} \nu_L^j, \qquad e_R^i \to W^{ij} e_R^j. \tag{2.27}$$

Since we are making the same change of variables to the doublet L_L, this change of basis commutes with the $SU(2)_L$ interactions in the covariant derivative. Therefore, both U and W disappear from the standard model theory without

any loss of generality. The Yukawa interaction for leptons then becomes

$$\begin{aligned}
\mathcal{L}_{\text{yukawa,lep}} &= -\lambda_\ell^i \bar{L}_L^i E_R^i \phi + h.c. \\
&= -\frac{\lambda_\ell}{\sqrt{2}} \begin{pmatrix} \bar{\nu}_L & \bar{\ell}_L \end{pmatrix} \begin{pmatrix} 0 \\ \upsilon + h \end{pmatrix} \ell_R + h.c. \\
&= -\frac{\lambda_\ell \upsilon}{\sqrt{2}} \left(\bar{\ell}_L \ell_R + \bar{\ell}_R \ell_L \right) - \frac{\lambda_\ell}{\sqrt{2}} h \left(\bar{\ell}_L \ell_R + \bar{\ell}_R \ell_L \right) \\
&= -\left(m_e \bar{e} e + m_\mu \bar{\mu} \mu + m_\tau \bar{\tau} \tau \right) \left(1 + \frac{h}{\upsilon} \right)
\end{aligned} \tag{2.28}$$

where

$$m_e = \frac{\lambda_e \, \upsilon}{\sqrt{2}}, \qquad m_\mu = \frac{\lambda_\mu \, \upsilon}{\sqrt{2}}, \qquad m_\tau = \frac{\lambda_\tau \, \upsilon}{\sqrt{2}}. \tag{2.29}$$

Again, we see that the masses of the fermions are also proportional to the VEV of the Higgs.

Once the Yukawa coupling is diagonal, the theory predicts that the lepton number of each generation is conserved (no direct mixing between the charged leptons). This has been tested experimentally, and there is no evidence of lepton family number violation from charged leptons: $\mathcal{B}(\mu^- \to e^- \gamma) < 10^{-11}$ and $\mathcal{B}(\mu^- \to e^- e^+ e^-) < 10^{-12}$ [1]. In addition, there is no CP symmetry violation in the lepton sector. In the standard model, the neutrinos are massless. However, there have been observations of one neutrino flavor oscillating into another [11], which is only possible if the neutrinos have mass. Neutrino oscillations do provide a mechanism for leptons to change flavor. For the quark sector, there is a right-handed field analog for both the upper and lower component of the $SU(2)_L$ doublet Q_L (u_R and d_R). In general, the upper and lower components will transform differently; a change from the mass basis (the physical quarks) to the interaction basis (that couples to $W^\pm$) requires the introduction of a unitary matrix, V^{ij}. This is the Cabibbo-Kobayashi-Maskawa (CKM) matrix, and it is the

source of flavor changing neutral currents (FCNCs) and CP symmetry violation in the standard model. For more information on the CKM matrix, see [12].

With the field definitions in the mass basis given in Eq. (2.20), we can write the covariant derivative in Eq. (2.6) as

$$\begin{aligned} D_\mu = \partial_\mu - i\frac{g_L}{\sqrt{2}}\left(W_\mu^+ T^+ + W_\mu^- T^-\right) - i\frac{1}{\sqrt{g_L^2 + g_Y^2}} Z_\mu \left(g_L^2 T_3 - g_Y^2 Y\right) \\ - i\frac{g_L g_Y}{\sqrt{g_L^2 + g_Y^2}} A_\mu \left(T_3 + Y\right) \end{aligned} \tag{2.30}$$

where the the raising and lowering operators, $T^\pm$, are

$$T^\pm = T_1 \pm iT_2 = \frac{1}{2}\left(\sigma_1 \pm i\sigma_2\right) = \sigma^\pm. \tag{2.31}$$

Since we know that the photon field, A_μ, couples to electric charge, we identify the electron charge, e, as

$$e = \frac{g_L g_Y}{\sqrt{g_L^2 + g_Y^2}} \tag{2.32}$$

and the electric charge quantum number as

$$Q = T_3 + Y \tag{2.33}$$

with the notation that Q = -1 for the electron. Combining these with the definition of the Weinberg angle in Eq. (2.23), we rewrite Eq. (2.30) as

$$D_\mu = \partial_\mu - i\frac{g_L}{\sqrt{2}}\left(W_\mu^+ T^+ + W_\mu^- T^-\right) - i\frac{g_L}{\cos\theta_w} Z_\mu \left(T_3 - \sin^2\theta_w Q\right) - ieA_\mu Q \quad . \tag{2.34}$$

This form of the covariant derivative is very useful in determining the interaction between the gauge bosons and the fermions. Using this covariant derivative with Eq. (2.12), the interaction between the W bosons and the fermions is

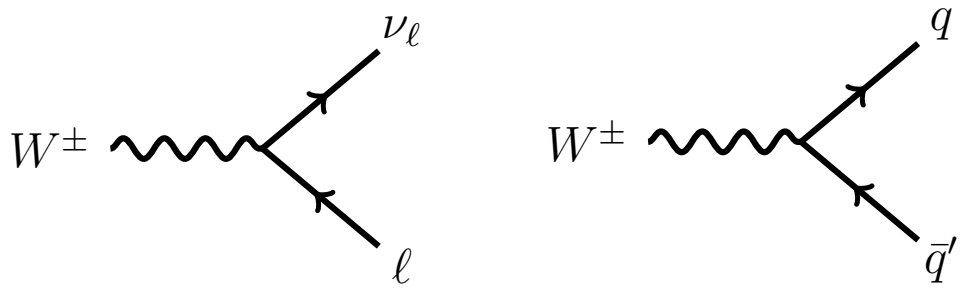

Figure 2.1: Feynman diagrams of the interaction between the W boson and fermions. Left: $W \to \ell\nu$. Right: $W \to q\bar{q}'$.

$$\mathcal{L}_{\psi,W} = \frac{g_L}{\sqrt{2}}\left(\bar{\nu}_L^i \gamma^\mu W_\mu^+ e_L^i + V^{ij}\bar{u}_L^i \gamma^\mu W_\mu^+ d_L^j\right) + h.c. \tag{2.35}$$

where i, j indicate the generation and V^{ij} is the CKM matrix, mentioned above. Instead of working with the left-handed fields, we can insert the projection operator directly and express the interaction term as

$$\mathcal{L}_{\psi,W} = \frac{g_L}{2\sqrt{2}}\bar{\nu}^i \gamma^\mu \left(1-\gamma^5\right) W_\mu^+ e^i + V^{ij}\frac{g_L}{2\sqrt{2}}\bar{u}^i \gamma^\mu \left(1-\gamma^5\right) W_\mu^+ d^j + h.c. \tag{2.36}$$

Figure 2.1 shows the Feynman diagrams for interactions between the W boson and the fermions.

The standard model described above has 19 free parameters. The parameters are the Yukawa couplings that give the quarks and leptons mass (9 parameters), the CKM mixing angles and CP-violating phase (4 parameters), the coupling constants of the gauge sector (3 parameters), the constants of the Higgs sector (2 parameters), and a parameter related to the vacuum structure of the strong interaction (1 parameter). These are not determined by the theory in any way; they must be determined experimentally. The value of the Higgs self-coupling (λ), or, equivalently, the mass of the Higgs boson (m_h) is the only parameter of

the standard model that has yet to be measured.

2.1.3 Success of the Standard Model

Instead of trying to determine directly the value of the input parameters of the standard model (e.g., g_L, g_Y, υ, etc.), it is more convenient to rewrite the parameters in terms of observables (e.g., m_W, m_Z, G_F, etc.) For example, what is the value of υ, the VEV of the scalar Higgs field, and how is it related to the Fermi constant, G_F? From muon decay, the lifetime of the muon (the inverse of its decay width) can be written to leading order as

$$\tau_\mu^{-1} = \frac{G_F^2 m_\mu^5}{192\pi^3}\left[1 + O\left(\frac{m_e^2}{m_\mu^2}\right)\right]\left[1 + O\left(\frac{m_\mu^2}{m_W^2}\right)\right] \tag{2.37}$$

whereas the tree-level prediction of the standard model is

$$\tau_\mu^{-1} = \frac{g_L^4 m_\mu^5}{192 \cdot 32\pi^3 m_W^4}. \tag{2.38}$$

Combining Eq. (2.22), Eq. (2.37), and Eq. (2.38), we find

$$G_F = \frac{1}{\sqrt{2}\upsilon^2} \tag{2.39}$$

and we find that G_F depends only on the value of υ (at leading order). This quantity was measured to be $G_F = 1.16637(1)\times10^{-5}\text{GeV}^{-2}$ [1], which corresponds to $\upsilon \approx 246$ GeV. This is the only parameter in the Lagrangian of the standard model that is not dimensionless. Theoretically, we expect that the mass of the Higgs boson will be around this value, and it should be observable at the LHC, if it exists.

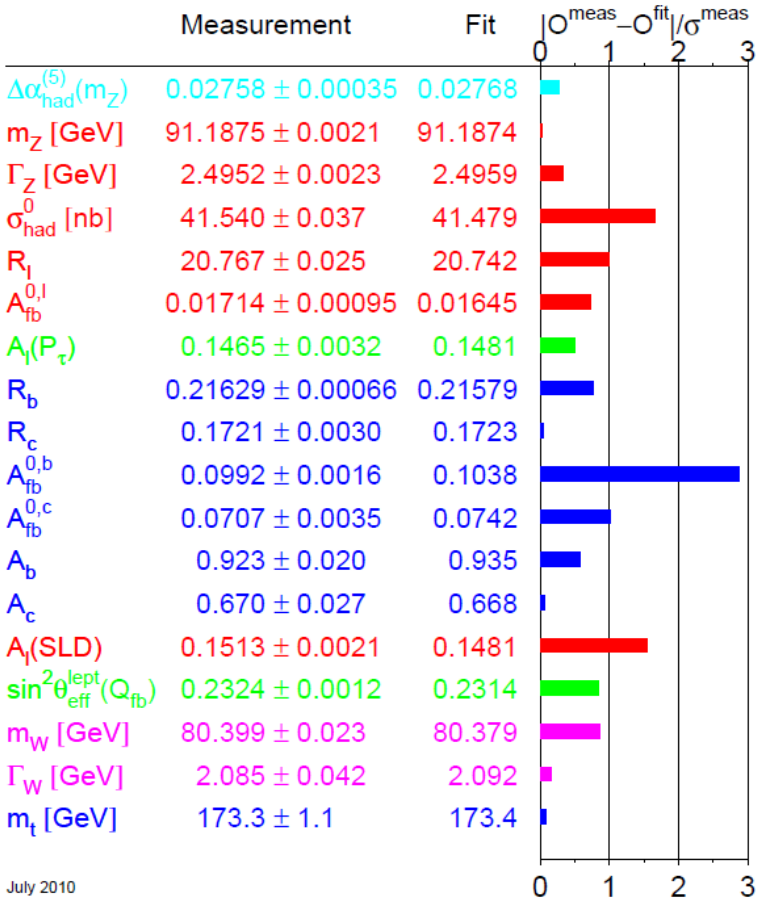

Figure 2.2: Comparison between standard model fit of observables and their measured values, as of July 2010 [3]. Overall, there is very good agreement between the two and no significant evidence for new physics.

To test the standard model, it would suffice to measure each of these parameters individually. Then, one could use those input values to make predictions that you can compare with the experimental measurements. However, a better approach is to use all measurements at the same time to overconstrain the standard model. In this way, one can compare each measured observable to the best-fit prediction of all observables.

At the time that this dissertation was written, most of the experimental results obtained thus far have been in very good agreement with theoretical predictions. Figure 2.2 shows the pull of several standard model measurements compared to theoretical predictions from the simultaneous fit. Agreement is often at the 0.1% level, and it is sometimes much better (in the case of the Z boson mass, for example). For more details on the compatibility of experimental results and standard model predictions, see [1, 13, 14]. However, there are also problems and inconsistencies of the standard model, such as neutrinos having mass, that force us to go beyond the standard model.

2.1.4 Problems of the Standard Model

Despite the great success of this established theory in explaining a wide array of experimental results, we know that it cannot be the ultimate description of our Universe. From measurements of neutrino experiments, we know that neutrinos can oscillate from one type to another. This is only possible if neutrinos have non-zero mass, contrary to the current formulation of the standard model. From cosmological measurements, we know that ordinary baryonic matter can only account for 4.6% of the energy-density of the Universe; the rest of the energy density that the standard model cannot explain comes from dark matter (22.7%) and dark energy (72.6%)[2]. Dark matter can only be inferred from its gravitational interactions with other matter. It does not interact electromagnetically like normal matter and, thus, appears "dark" to our telescopes. Dark energy is a hypothetical form of energy that permeates all space, resulting in an increase in the expansion rate of the Universe. The two are not related (or, we do not believe them to be, at this time). Furthermore, the standard model is

unable to explain the matter-antimatter asymmetry that we see today. That is, if there existed equal amounts of matter and antimatter after the big bang, and if everything around us is (mostly) matter, what happened to all the antimatter?

In addition to an inability to explain some of the particle physics phenomena we see in nature, the standard model also suffers from a number of deficiencies. The most obvious lack of the standard model is that it does not provide an explanation for the force of gravity. Apart from this, the standard model possesses other theoretical features that imply that it is only an approximate theory. The Higgs boson itself has mass, and this mass receives large quantum corrections that are related to the scale up to which the standard model is assumed to be valid. The two most common scales at which the standard model is expected to break down are the Planck scale and the grand unification scale. The Planck scale is the scale at which the quantum effects of gravity are expected to be large, and it corresponds to an energy of roughly 10^{19} GeV. The grand unification energy scale is the scale at which the electromagnetic, weak, and strong forces unite and can be described as a single force. This depends on the nature of the grand unified theory, but it is typically at an energy of roughly 10^{16} GeV, a few orders of magnitude below the Planck scale. If there is no new physics between one of these scales and the electroweak scale, then the corrections are many orders of magnitude larger than its actual mass. This is the Hierarchy Problem. In order to keep the mass of the Higgs boson at the right scale (the electroweak scale $\sim$ 100 GeV), the bare mass of the Higgs has to be very precisely tuned to cancel these quantum corrections. This kind of fine-tuning is considered unnatural.

For these reasons, it is expected that some new physics beyond the standard

model will enter at the ~ TeV scale in order to avoid the fine-tuning problem. Some examples of new physics that we may see at the LHC include supersymmetric particles [15], extra dimensions [16, 17], hidden valley particles [18], or new gauge bosons [19]. These new physics models either address a current problem in physics, such as solving the hierarchy problem or providing a dark matter candidate, or they examine the possibility of nature having more particles than those contained in the standard model, such as additional fermions or bosons.

2.2 New Heavy Gauge Boson W'

A possible new physics scenario that may be realized at the TeV scale is the existence of additional heavy gauge bosons, W' and Z', similar to the electroweak gauge bosons, W and Z. Additional gauge bosons appear in many extensions of the standard model. Generically, models that contain a heavy W' also contain a heavy Z', though the reverse is not necessarily true. However, the mass difference between the W' and the Z' depends on the details of the model. Therefore, it is possible that a W' may be discovered before a Z'. Here, we focus on theories that predict heavy W' bosons.

For example, theories with extra dimensions, where the W boson can propagate in that extra dimension naturally give rise to heavy copies of the standard model W boson [20]. These heavy copies correspond to a spectrum of excitations, or Kaluza-Klein modes, of the standard model W boson (the zero-mode). If the extra dimension is of size R, and the dimension is curled up such that

there are periodic boundary conditions, then the mass of the n^{th} excited state is

$$m_W^{n\,2} = m_W^2 + 4m_0^2 \sin^2\left(\frac{n\pi}{2\,(N+1)}\right) \tag{2.40}$$

where N is the total number of states and m_0 is related to the size of the dimension by

$$\frac{m_0}{N+1} = \frac{1}{R} \tag{2.41}$$

to match onto the spectrum of KK modes [20]. Experimentally, we care about the first few modes ($n \ll N$), such that Eq. (2.40) becomes

$$m_W^{n\,2} \approx m_W^2 + \frac{n^2\pi^2}{R^2}. \tag{2.42}$$

Little Higgs models are based on the idea that the Higgs boson is a pseudo-Nambu-Goldstone boson. These models predict the existence of W' bosons. In the simplest Little Higgs model, the standard model electroweak gauge group $SU(2)_L \otimes U(1)_Y$ is extended to $SU(3)_L \otimes U(1)_X$ [21]. This enlarges the $SU(2)$ doublets of the standard model to $SU(2)$ triplets and introduces $SU(3)$ gauge bosons. There are 8 gauge bosons; three of these correspond to the weak gauge bosons, and five new gauge bosons are introduced. The symmetry breaking of $SU(3)_L \otimes U(1)_X \to SU(2)_L \otimes U(1)_Y$ occurs via a Higgs mechanism at a scale f. The five new gauge bosons, two of which correspond to $W'^{\pm}$, all have mass of order the scale f.

In the standard model, the W boson only interacts with left-handed particles. However, it may be that both left- and right-handed charged gauge bosons are realized in nature in a symmetrical way [22, 23, 24]. In these left-right symmetric models, the electroweak gauge group is extended to $SU(2)_L \otimes SU(2)_R \otimes U(1)_X$ where the couplings g_L and g_R can be independent, in general, or they may be

equal in the case of exact left-right symmetry. Although those two couplings are not related, there does exist the relation

$$\frac{1}{g_Y^2} = \frac{1}{g_R^2} + \frac{1}{g_X^2} \tag{2.43}$$

where g_Y is the standard model $U(1)_Y$ coupling, and g_R and g_X are the $SU(2)_R$ and $U(1)_X$ couplings, respectively [25]. This means that $g_R,\ g_X > g_Y$, and the couplings are bounded from below. Thus, they cannot be arbitrarily small.

Similar to the simplest Little Higgs model described above, the symmetry breaking of $SU(2)_L \otimes SU(2)_R \rightarrow SU(2)_L \otimes U(1)_Y$ occurs via a Higgs mechanism at a scale f, and the heavy gauge bosons have a mass of the same order. If the W' boson is, indeed, right-handed, then there must be right-handed neutrinos as well. While indirect limits on right-handed W' bosons can be quite stringent, with lower bounds on the mass of the W' between 1 - 16 TeV, they are also very sensitive to the assumptions of the model [26, 27, 28]. Typically, one can evade some of these limits by assuming that the right-handed neutrinos are massive ($\sim$ GeV), but the subsequent decays of the heavy neutrinos can result in final states that are very different than a standard model W boson decay (e.g., two or more leptons).

In every case, the W' is a gauge boson that is associated with a spontaneously broken symmetry. To obtain a W' that is very similar to the standard model W boson, we consider a simple extension to the standard model where the electroweak gauge group is extended to $SU(2)_1 \otimes SU(2)_2 \otimes U(1)_X$, as described in [25, 29]. We work through this model in some detail in Sec. B. Again, a Higgs mechanism breaks this gauge symmetry down to the electroweak group, and the mass of the W' is at the same scale as this symmetry breaking. The $SU(2)_L$

coupling of the standard model is

$$\frac{1}{g_L^2} = \frac{1}{g_1^2} + \frac{1}{g_2^2} \tag{2.44}$$

where g_1 and g_2 are the $SU(2)_1$ and $SU(2)_2$ couplings, respectively. The coupling of the massive W', $g_{W'}$, is related to the coupling of the W boson by

$$g_{W'} = g_L \cdot \frac{g_1}{g_2} \tag{2.45}$$

Unlike the left-right symmetric models, the coupling $g_{W'}$ can be arbitrarily small. In the special case $g_1 = g_2$, the coupling of the W' is the same as for the W, and the W' behaves like a massive copy of the W (it is a sequential W').

2.3 Searches for W'

Experimentally, we are searching for an excess of events containing an electron and a neutrino. Previously, there have been both direct and indirect searches for evidence of new gauge bosons. The CDF experiment performed a search for W' bosons in events with an electron and large transverse energy imbalance. Using 5.3 fb^{-1} of data, they were able to exclude W' bosons with $m_{W'} < 1.12$ TeV [30]. Using 2.3 fb^{-1} of data, the D0 collaboration was able to exclude W' bosons with $m_{W'} < 863$ GeV in events with a reconstructed top and bottom quark [31].

Complementary to the direct searches, indirect searches for W' bosons can result in much more stringent limits. For example, consider neutral meson mixing between kaons or B-mesons ($K^0 - \bar{K}^0$, $B^0 - \bar{B}^0$). In the standard model, the transitions $K^0 \to \bar{K}^0$ and $\bar{K}^0 \to K^0$ are due to weak interactions. At lowest order, these transitions are described by box diagrams involving two W bosons and

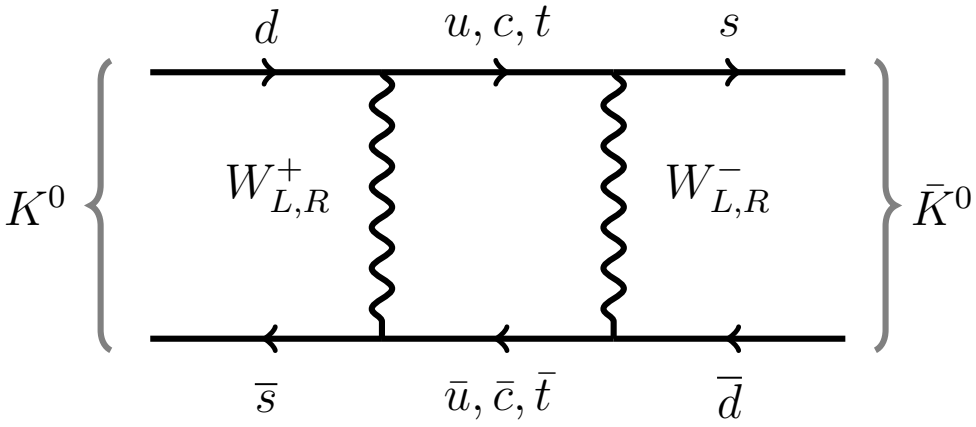

Figure 2.3: One Feynman box diagram showing neutral kaon mixing as mediated by left- and right-handed charged gauge bosons.

two up-type quarks (u, c, t). These box diagrams provide one way in which new physics could be discovered. Left-right symmetric models introduce new, right-handed charged gauge bosons, $W_R^{\pm}$. Figure 2.3 shows a Feynman diagram of the transition $K^0 \to \bar{K}^0$ involving left- and/or right-handed W bosons. This CP-violating process provides one of the best constraints on W_R.

The biggest uncertainty in making theoretical predictions for these models is the right-handed quark mixing matrix (analogous to the CKM matrix of the standard model). Most of the literature focuses on two limiting cases: manifest left-right symmetry and pseudomanifest left-right symmetry. In manifest left-right symmetry, the right-handed quark mixing matrix is identical to the CKM matrix [32, 33]. In pseudomanifest left-right symmetry, the right-handed quark mixing is related to the complex conjugate of the CKM matrix multiplied by additional CP phases [34, 35, 36, 37].

A major constraint on the mass of the W_R boson, m_{W_R}, comes from the $K_L - K_S$ mass difference, Δm_K. This is because the time dependence of the $K^0 - \bar{K}^0$ oscil-

lation depends on Δm_K. Experimentally, the mass difference is

$$\Delta m_K = m_{K_L} - m_{K_S} = (3.483 \pm 0.006) \times 10^{-12} \text{ Mev} \tag{2.46}$$

when assuming CPT symmetry [1]. As a result, there is a very stringent bound of $m_{W_R} > 1.4{-}2.5$ TeV, depending on the theoretical assumptions (e.g., manifest or pseudomanifest left-right symmetry). However, if one makes no assumptions on the right-handed quark mixing matrix, the limit on m_{W_R} can be as low as $m_{W_R} > 300$ GeV [38]. In fact, there are fine-tuned values for the mixing matrix which yield no useful constraint on m_{W_R} [39].

Astrophysical and cosmological measurements also greatly constrain left-right symmetric models. In models with right-handed interactions, one must consider the effect of right-handed neutrinos. Assuming that there are three light ($m_{\nu_R} < 1$ MeV) right-handed neutrinos, they will contribute as relativistic degrees of freedom to big bang nucleosynthesis (BBN). If the ν_R decouple at a temperature T_{dec}, then the limit on m_{W_R} is

$$m_{W_R} > 3.3 \left(\frac{T_{\text{dec}}}{140\text{MeV}} \right)^{3/4} \text{ TeV} \tag{2.47}$$

where $T_{\text{dec}} > 140$ MeV for the ν_R to decouple before the annihilation epoch of pions [40]. In addition, if the ν_R are light ($m_{\nu_R} < 10$ MeV), there is a limit of $m_{W_R} > 16$ TeV from supernova (SN) 1987A data on neutrino emission [41]. Again, limits from indirect searches depend much more heavily on the assumptions of the W' model than direct searches.

As in previous direct searches, we present a search for a heavy W' in events with an electron and a neutrino in the context of the Altarelli benchmark model [19]. Figure 2.4 shows a Feynman diagram for this process. In this model,

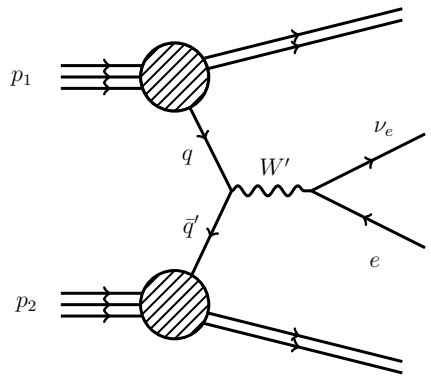

Figure 2.4: Diagram showing the process $pp \to W' \to e\nu$.

the W' is a heavy copy of the standard model W boson; it has the same coupling (current) to fermions. The neutrino to which the W' decays is light and stable. Additionally, the Altarelli benchmark model assumes that the decay width of the W' scales as the square of its mass. Its decay width is related to the decay width of the W boson by

$$\Gamma_{W'} = \frac{4}{3}\frac{m_{W'}^2}{m_W^2}\Gamma_W \tag{2.48}$$

where the factor of $\frac{4}{3}$ comes from the fact that the decay channel $W'^+ \to t\bar{b}$ (+ h.c.) is kinematically allowed for $m_{W'} > 180$ GeV and the quarks can come in any of three color-anticolor combinations. This model also assumes that additional fermions (if they exist) are too heavy to be produced in these decays.

In the gauge sector of the Altarelli model, decays of W' to pairs of gauge bosons, such as the decay $W' \to WZ$, are suppressed. Furthermore, it is assumed that there is no mixing between the W' and the other gauge bosons (no $W - W'$ or $Z' - W'$ mixing). Beyond simply excluding mixing between gauge bosons, the model also ignores interference between the W and W' bosons. If a W' is discovered, such an interference term could be used to determine the helicity of the W' couplings [42, 43, 44].

CHAPTER 3

THE EXPERIMENTAL APPARATUS

In our search for W' bosons, we must first be able to produce W' bosons ($pp \to W'$). To do this, we use proton-proton collisions collected at CERN. Currently, CERN is the facility that is best equipped to accomplish this task, and it is located near Geneva, Switzerland, on the border of France and Switzerland. Figure 3.1 shows an illustration of the particle accelerator complex at CERN. The process begins with a bottle of Hydrogen. The electrons are stripped off the Hydrogen atoms, and the protons are accelerated to an energy of 50 MeV from Linac 2 into the Proton Synchrotron (PS) Booster. From there, the protons are accelerated and focused in the PS and the Super PS (SPS) until they reach an energy of 450 GeV and get injected into the Large Hadron Collider (LHC).

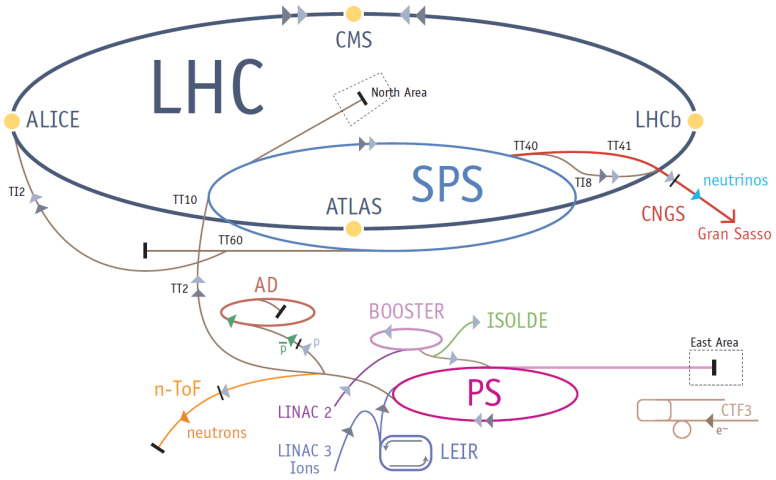

Figure 3.1: CERN accelerator complex showing the Large Hadron Collider, the four main LHC experiments (ALICE, ATLAS, CMS, and LHCb), and the many supporting accelerators that inject protons into the LHC.

3.1 The Large Hadron Collider

The LHC is a particle accelerator that is 26.695 kilometers (16.588 miles) in circumference. It is located at a mean depth of 100 m underground; the depth of the LHC tunnel ranges from 50 m (near Lake Léman) to 174 m (under the Jura), a gradient of 1.4%[45]. There are several reasons why the LHC was built underground. First, the LHC was built in the same tunnel as the Large Electron-Positron Collider (LEP), a lepton collider at CERN operating between 1989 and 2000. Second, the rock above the LHC provides good shielding. It provides plenty of protection from the radiation produced by the LHC when it is running so that it is of no danger to people living nearby. Also, it provides a barrier to natural radiation to keep it from reaching the LHC and the detectors underground; such radiation might mimic signals in the detector, producing a large background source to these precision experiments.

The LHC needs to be large, because the energy of the particle collisions will depend upon the size of the machine and the strength of the magnets used to accelerate and steer the particles. In total, the LHC uses more than 9000 magnets, including dipoles, quadrupoles, sextupoles, octupoles, etc. The 1232 main dipole magnets provide a closed circular path for the protons. Operating at a temperature of 1.9 K (cooled by super-fluid Helium), these 15 m long dipole magnets can reach a maximum magnetic field of 8.3 T (at a current of 11.7 kA). Note that the LHC is a proton-proton collider. Since the Lorentz force on a particle with charge q due to a magnetic field $\vec{B}$ is

$$\vec{F} = q\vec{v} \times \vec{B} \tag{3.1}$$

there must be a different magnetic field for each of the two oppositely circu-

lating proton beams to get them to bend properly. Thus, the LHC has a 2-in-1 magnet design, where there are two beam pipes in each dipole magnet. In addition to the dipole magnets, there are 392 main quadrupole magnets that provide the transverse focusing to get the beams to be as small as possible. The other multipole magnets serve as corrector magnets to assist with beam focusing and small adjustments to account for effects such as gravitational interactions between the protons and the Earth, interactions between the beams, etc.

3.1.1 Proton Collider

As mentioned above, the LHC collides together protons (and lead ions). At high energies, colliding protons is much more energy efficient than colliding electrons and positrons. As charged particles are bent by magnetic fields, they emit electromagnetic radiation. Emitting this synchrotron radiation, as it is called, causes the particles to lose energy. This energy needs to be resupplied by the magnet system of the LHC; thus, more energy emitted translates to a larger energy requirement and a higher cost. A particle of charge q traveling at a velocity β ($\frac{v}{c}$) around a circle of radius ρ loses an amount of energy due to synchrotron radiation of

$$\Delta E = \frac{4\pi}{3}\left(\frac{q^2\beta^3\gamma^4}{\rho}\right) \tag{3.2}$$

where γ is the usual relativistic factor ($\gamma^{-2} = 1 - \beta^2$). For a relativistic particle, its energy and momentum are given by γmc^2 and $\gamma\beta mc$, respectively. If the particles have sufficiently high energy, as they do at the LHC, their mass can be ignored ($E \gg mc^2$). Therefore, for electrons and protons of the same energy ($E_e \approx E_p$,

$|\vec{p}_e| \approx |\vec{p}_p|$), the ratio of energy loss for the two is

$$\frac{\Delta E_p}{\Delta E_e} \approx \left(\frac{m_e}{m_p}\right)^4 \sim 8.8 \times 10^{-14}. \tag{3.3}$$

From Eq. (3.3), we can see why we no longer build circular accelerators to collide electrons and positrons: the energy loss from synchrotron radiation is simply too large. However, one might expect it to be better to collide protons and antiprotons (as is done at the Tevatron collider in Batavia, IL, in the United States) than to collide just protons. Indeed, the LHC would not have needed the 2-in-1 magnet design (described above) were it a proton-antiproton collider. One reason to focus on a proton-proton collider is that it is challenging and expensive to produce an intense beam of antiprotons. Another reason is related to parton distribution functions (PDFs).

Although the proton is, in large part, made up of three valence quarks (*uud*), it also consists of a large virtual sea of quark pairs and gluons (partons). Each parton carries a fraction, x, of the momentum of the proton. The density of quark (or gluon) states that carry a fraction of the momentum of the proton, x_q, is given by the parton distribution function, $f_q(x_q, Q^2)$. These functions depend on the momentum transfer of the parton interaction, Q^2, the energy at which you are probing the proton. Figure 3.2 shows the CTEQ6 PDFs at Q = 2 and 100 GeV [4]. While the LHC is colliding protons together, it is the partons inside that are interacting and producing the interesting physics processes. We can approximate the pp collisions of the LHC as a collision of two partons, with the other particles as spectators. For each event, the fraction of the proton's momentum that each parton carries is given by a PDF. In 2010, the center-of-mass energy for proton-proton collisions was 7 TeV (3.5 TeV per proton). At this energy, gluons are the dominant interacting partons, and the difference between

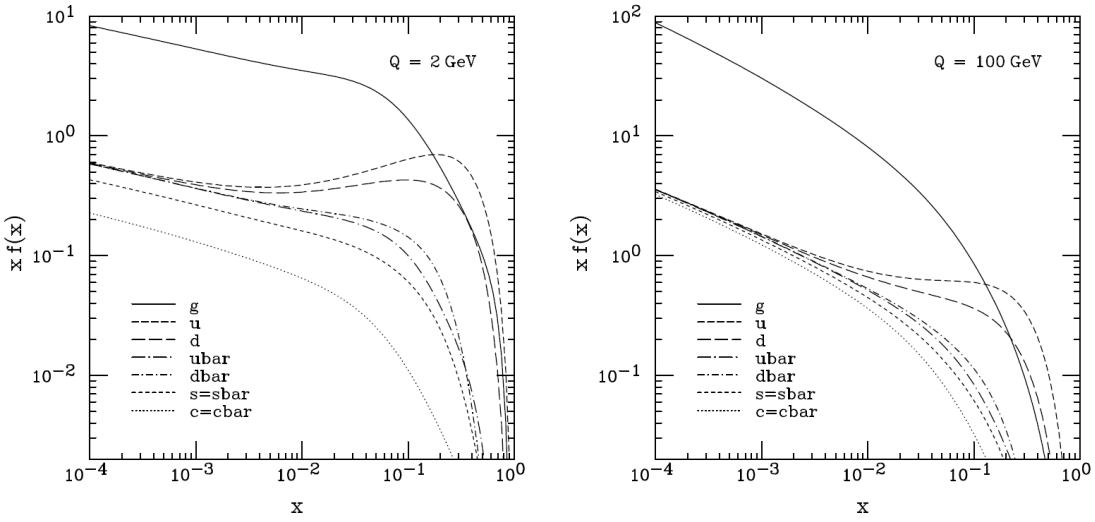

Figure 3.2: The CTEQ6M parton distribution functions when probing the proton at energies of Q = 2 GeV (left) and 100 GeV (right) [4]. For small fractions of the proton momentum, gluons are the dominant interacting partons at these energies.

protons and antiprotons is negligible.

The cross section, σ, is a measure of the probability that an event occurs. For example, the cross section of two protons producing a W' is $\sigma(pp \to W')$. The higher the cross section, the more likely that the two protons will interact. Thus, the cross section behaves like a hypothetical area of the protons. Indeed, cross sections have units of area, and they are typically measured in barns, where 1 barn = 10^{-24} cm^2 and is about the size of a uranium nucleus. The differential cross section for a particular proton-proton process can be written as

$$d\sigma = A \sum_{q,q'} \int_0^1 dx_a \int_0^1 dx_b f_q(x_a, Q^2) f_{q'}(x_b, Q^2) d\hat{\sigma} \tag{3.4}$$

where $d\hat{\sigma}$ is the differential cross section of the parton-parton interaction, f_q and $f_{q'}$ are parton distribution functions (PDFs), and A is a color factor to account for the particle multiplicities in the parton (quarks and gluons) sum. The cross

section will depend on the square of the center-of-mass energy of the proton-proton system (s), which is related to the square center-of-mass energy of the parton-parton system ($\hat{s}$) by $\hat{s} = x_a x_b s$.

3.1.2 Luminosity

To have the best chance of discovering new physics, a particle collider should have a large center-of-mass energy. In this regard, the LHC is at the energy frontier, operating at more than 3 times the energy of the previous highest-energy collider, the Tevatron. At such a high energy, there is a greater probability to produce interesting new physics processes, if they exist. In addition to the cross section, the rate at which a physics process occurs depends on the instantaneous luminosity. The three are related by the equation

$$R(s) = \sigma(s)\mathcal{L}_{\text{inst}} \tag{3.5}$$

where R is the rate of the physics process (e.g., the rate at which new particles are produced) and σ is the cross section of that process, both of which depend on the center-of-mass energy squared (s), and $\mathcal{L}_{\text{inst}}$ is the instantaneous luminosity. Besides the energy of a particle accelerator, the luminosity that an accelerator can deliver is one of the most important properties of that machine. It is a measure of the rate at which the particles collide; more particle collisions means more chances to produce physics of interest.

The instantaneous luminosity is typically given in terms of number per unit area per unit time ($\text{cm}^{-2}s^{-1}$) and can be written as

$$\mathcal{L}_{\text{inst}} = f\frac{N_1 N_2}{4\pi\sigma_x\sigma_y} \tag{3.6}$$

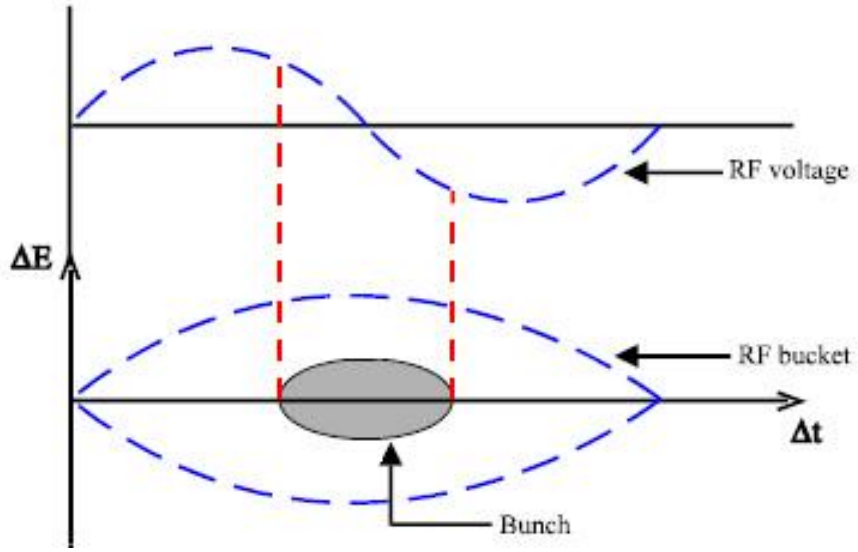

Figure 3.3: The bunch and bucket structure at the LHC created by radio frequency cavities around the LHC ring to ensure high luminosity at the collision points [5].

where N_1 and N_2 are the number of protons in beam 1 and 2, respectively, f is the frequency of revolution for the protons ($\sim$ 11 kHz at the LHC), and σ_x (σ_y) is the width of the proton beam in the x (y) direction. Since the size of the accelerator is fixed and the protons cannot travel faster than the speed of light, the revolution frequency cannot be changed much. The way to increase the luminosity in Eq. (3.6) is to increase the number of protons and/or decrease the size of the beams.

It is important to note that the proton beams are not a steady stream of protons. Instead, the protons come in well-defined bunches of protons, due to the Radio Frequency (RF) cavities. Indeed, the main purpose of the RF cavities is to keep the bunches tightly held together to ensure a high luminosity at the collision points around the LHC. There are 8 RF cavities per beam, and each RF cavity accelerates the protons by delivering 2 MeV of energy to each proton at a

frequency of 400 MHz. The protons that are exactly in sync with the RF cavities are called synchronous particles. Protons that are a little out of sync with the RF cavities will oscillate longitudinally back and forth around the synchronous particles, getting clumped around them, which causes the bunch structure. The PS is responsible for the bunch structure, not the LHC. To make sure that the protons always see an accelerating voltage, the RF frequency is an integer multiple of the revolution frequency ($\sim$ 11 kHz). The integer multiple is called the harmonic number, and it is about 35640. This is the number of segments that can contain bunches of protons, and these segments are called buckets. Figure 3.3 illustrates the bunch and bucket structure created by the RF cavities. Although there are 35640 buckets, not all of these are filled with bunches. The LHC machine only had 368 bunches (348 colliding together) for the 2010 run, and the nominal number of bunches (occupied buckets) it plans to use is 2808. Only a fraction of the buckets can be filled, because there has to be a sufficiently large gap, called the abort gap, to allow enough time to switch on kicker magnets to divert the beam out of the LHC in case the beam needs to be dumped. Increasing the number of bunches and the number of protons per bunch will yield a higher luminosity, but this option is limited by beam-beam interactions that begin to become important when the number of protons becomes large. This can be mitigated somewhat by having the beams crossing and colliding at an angle, as shown in Fig. 3.4.

As the beams become more and more focused, the protons in each beam become more densely packed, and the protons in the opposing beams are more likely to collide[1]. The size of the beam depends on the transverse emittance, ϵ,

[1]Imagine two swarms of bees flying towards one another. The more tightly that each group of bees fly together, the greater the chance that individual bees in opposing swarms will run into one another.

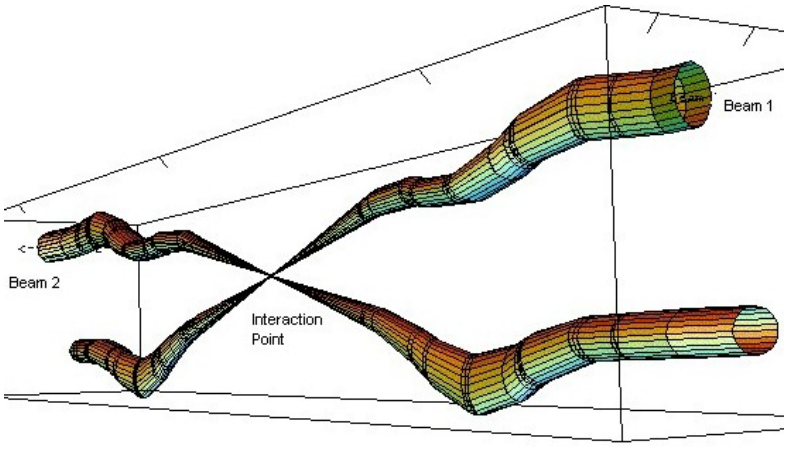

Figure 3.4: Illustration of the beams of the LHC colliding at an angle to one another [5]. This is done to reduce long-range interactions between the beams.

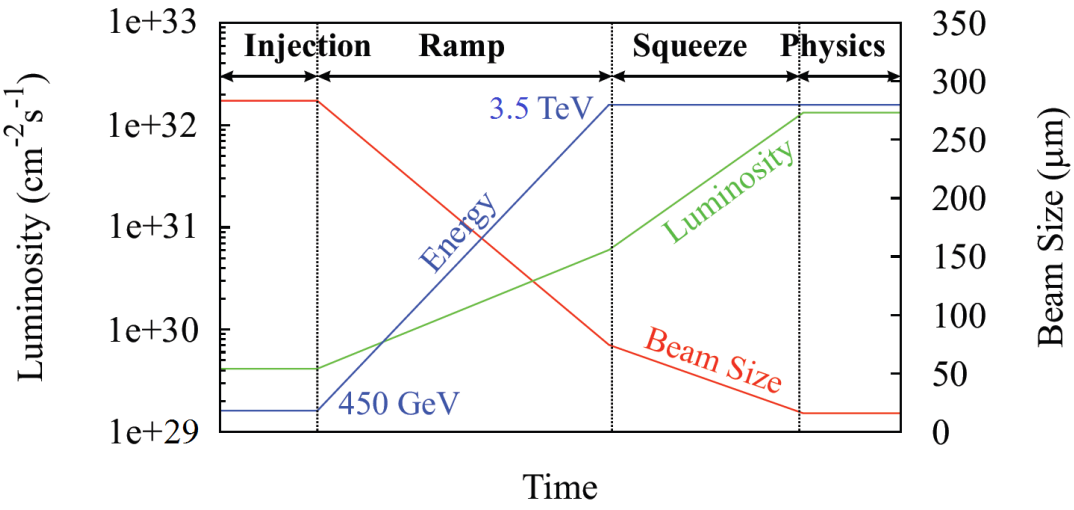

Figure 3.5: Evolution of beam parameters through different operation stages [6]. The SPS injects proton beams into the LHC. The LHC accelerates the protons to the desired energy, squeezes the beams to achieve a higher luminosity, and stabilizes the beams for physics use.

and the betatron function, β(s). The emittance is a measure of how effectively the protons travel in a straight and narrow line; it is constant along the ring and defined at a fixed proton momentum. A smaller emittance means that protons

in a bunch will stay together better. The normalized emittance, $\epsilon_n = \gamma\beta\epsilon$, is independent of momentum. Due to electromagnetic interactions of the colliding bunches, the protons in a bunch will oscillate around an ideal circular trajectory as they travel around the accelerator. These are called betatron oscillations. The tune of the machine is the number of betatron oscillations per machine revolution. To prevent a tune resonance from occurring, which can cause damage to the machine, the tune should not be an integer. The betatron function at a given point s along the ring, $\beta(s)$, is the amplitude of the transverse envelope of the betatron oscillation at that point. The value of $\beta(s)$ depends upon the optics of the machine and how well the beams can be "squeezed" and focused at the intersection points. The important quantity for the highest luminosity is the value of the betatron function at the interaction point, β^*. Figure 3.5 shows how the luminosity, beam energy, and beam size evolve during a typical machine cycle from bunch injection to a stable beam state appropriate for recording the collisions.

Using the information above, we can write the instantaneous luminosity as

$$\mathcal{L}_{\text{inst}} = f\frac{n^2 k_b \gamma}{4\pi\epsilon_n\beta^*}F \tag{3.7}$$

where n is the number of protons per bunch, k_b is the number of bunches, γ is a relativistic Lorentz factor (E/mc^2) and F is a crossing angle factor (always less than 1) given by

$$F = 1/\sqrt{1+\left(\frac{\theta_c\,\sigma_z}{2\sqrt{\epsilon_n\,\beta^*}}\right)^2} \tag{3.8}$$

that measures the geometric loss of overlap between two bunches that cross at an angle θ_c to one another [46]. Table 3.1 gives the parameters of LHC that were achieved during the 2010 run and their design values. To compare the LHC to

Table 3.1: LHC machine and proton collision parameters. We give both the design values of the parameters and those used by the end of 2010.

Symbol	Parameter	End of 2010	Design
f (kHz)	Frequency for proton to circle ring	11.245	11.245
N ($\times 10^{11}$)	Number of protons per bunch	1.2	1.15
k_b	Number of bunches	368	2808
β^* (m)	Betatron parameter at IP	1.5	0.55
ϵ_n (μm)	Normalized beam emittance	2.4 - 4.0	3.75
σ^* (μm)	Transverse beam size at IP	45 - 60	16
σ_z (μm)	Bunch length	7.5	7.5
θ_c (μrad)	Crossing angle	100	285
$\langle n \rangle$	Interactions per crossing	3	20
Δt_{bunch} (ns)	Time between collisions	150	25
E_{stored} (MJ)	Stored energy per beam	25	360
E_{proton} (TeV)	Energy per proton	3.5	7.0
$\mathcal{L}_{\text{inst}}$ (cm^{-2}s^{-1})	Instantaneous luminosity	2×10^{32}	10^{34}

previous colliders, it is useful to consider energy stored in the beam versus the beam momentum, as shown in Fig. 3.6. At design running, the LHC machine will achieve a factor 2 in magnetic field (dipole magnets), a factor 7 in beam energy, a factor 30 in luminosity, and a factor 200 in stored energy improvement over existing accelerators.

For the experiments that are collecting and recording these collisions, the goal is to record the largest possible number of collision events (not just have the largest rate). The instantaneous luminosity is not constant with time; the

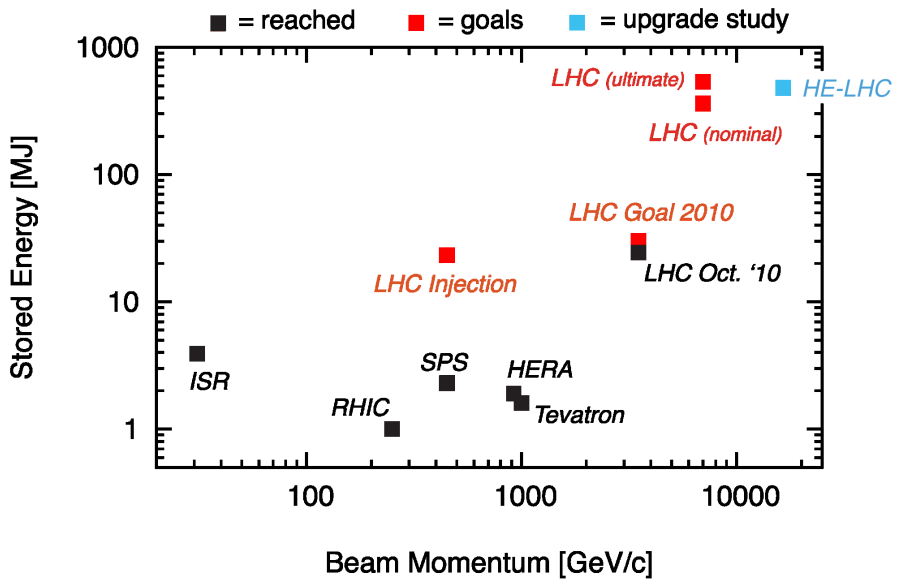

Figure 3.6: Stored energy versus beam momentum for several different particle colliders, including the LHC and the Tevatron [1]. The LHC operating at nominal conditions will surpass previous accelerators by an order of magnitude in beam momentum and several orders of magnitude in stored energy.

beams decrease in intensity (roughly exponentially) over time due to losses from the protons that are destroyed by collisions each revolution around the circumference of the LHC. The amount of data delivered to and recorded by an experiment depends on the *integrated luminosity*, L, which can be written as

$$L = \int \mathcal{L}_{\text{inst}}(t)\, dt \approx \mathcal{L}_0\, \tau \left(1 - e^{-t_{sb}/\tau}\right) \tag{3.9}$$

where $\mathcal{L}_0$ is the peak instantaneous luminosity, τ is the decay constant (usually between 5 and 15 hours), and t_{sb} is the amount of time that the beams are in a stable configuration for collisions. Although the goal is to accumulate the largest amount of integrated luminosity, each path to achieving this comes at some cost. One thing to consider is the number of independent collision events per bunch crossing, called pile-up. These overlapping events make it difficult

for the experiments to reconstruct individual collisions in the detectors, making high pile-up scenarios unfavorable. The amount of time the beams are colliding and the number of bunches do not increase pile-up, while the number of protons, β^*, and ϵ_n do increase pile-up. While there were an average of three collisions per crossing in 2010, the average pile-up is expected to be closer to 20 when the LHC is running at design specifications.

3.2 The Compact Muon Solenoid

The beams cross at four points along the LHC circumference. These points are the locations of the four detectors: ALICE, ATLAS, CMS, and LHCb. The analysis in this dissertation is based on data collected by the Compact Muon Solenoid (CMS) detector.

CMS is one of two general purpose detectors at the LHC. It is cylindrical in shape with a radius of 7.3 m (24 ft) and a length of 21.6 m (71 ft). Although its size could hardly be considered small, the detector weighs a massive 12,500 tons, earning it the "compact" label in its name. Figure 3.7 shows an overview schematic of its various components.

The coordinate system of CMS is very similar to other particle physics detectors, both past and present. The origin is located at the nominal collision point. The beam direction defines the z-axis, the y-axis points upwards, and the x-axis points from the interaction point to the center of the LHC ring. The azimuthal angle, ϕ, is measured around the beam axis, where $\phi = \tan^{-1}(x/y)$. The polar angle, θ, is measured from the z-axis. The pseudorapidity, η, is defined by $\eta = -\ln(\tan(\theta/2))$. Transverse quantities, such as transverse momentum

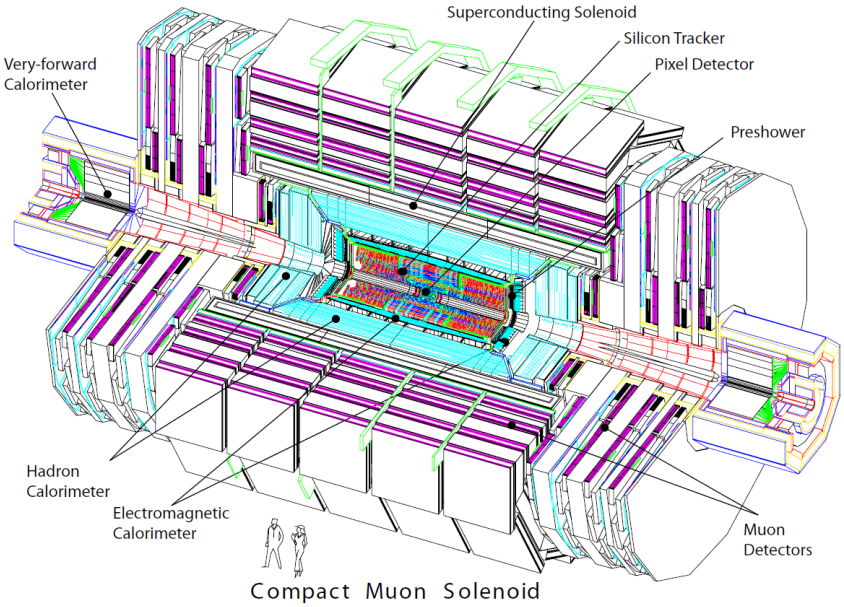

Figure 3.7: An overview of the CMS detector showing the location of each of the subdetectors [7]. The two individuals above give the scale of CMS.

(p_T), transverse energy (E_T), and missing transverse energy ($\not{E}_T$), are determined from x and y coordinates.

Note that energy is a scalar quantity. Therefore, it has no direction associated with it. However, due to the segmentation of the calorimeters, we can determine where the energy was deposited. Thus, we can assign a direction to energy as a vector pointing from the nominal beam spot to the location of the energy deposit.

The detector was built to be sensitive to new physics signatures while maintaining the ability to make high precision measurements of standard model processes. In order to achieve this, it needs to satisfy the following general requirements [7]:

- High-precision muon measurements over a wide range of momenta.

- Good charged particle momentum resolution and reconstruction efficiency in the tracker. Efficient tracking is necessary for electron, muon, and photon identification, as well as τ- and b-jet tagging.
- Very good electromagnetic calorimeter energy resolution for electron and photon identification, π^0 rejection, and di-photon and di-electron mass resolution. This is critical for searches such as a Higgs boson decaying to two photons ($H \to \gamma\gamma$).
- A full-coverage, fine-lateral segmentation hadronic calorimeter to achieve good jet and missing transverse energy resolution.

3.2.1 Trigger and Data Acquisition System

From Eq. (3.5), we see that the rate of physics processes is given by the product of cross section and luminosity. The total proton-proton cross section for inelastic interactions (σ_{in}) is approximately 60 mb (recall: 1 mb = 10^{-3} barn = 10^{-27} cm^2). Figure 3.8 shows the cross section and event rate as a function of center-of-mass energy ($\sqrt{s}$). Note that the cross section for electroweak processes such as W and Z boson production are around the nano-barn scale, nearly 6 orders of magnitude smaller than σ_{in}. The standard model Higgs boson is produced even more infrequently than that with a cross section more than ten orders of magnitude smaller than σ_{in}, depending on the mass of the Higgs boson. If there are new physics processes beyond the standard model yet to be discovered, they almost certainly have an even smaller cross section, typically a few hundred pico-barns or smaller.

At design specifications, the LHC will produce a large rate of collisions. As-

suming a bunch spacing of 25 ns, this corresponds to a peak collision frequency of 40 MHz. Taking into account the abort gaps discussed above, the average bunch-crossing rate will be 31.6 MHz (rate = number of bunches × revolution frequency = 2808 × 11.245 kHz = 31.6 MHz). With 20 interactions per crossing, this amounts to about 600 million interactions per second. However, events can only be stored to disk at a few hundred Hz. This reduction in data is accomplished by triggering on and storing events which meet certain criteria. The trigger must select which events are kept in an intelligent way in order to keep the rare and interesting physics events.

The triggering at CMS is separated into two levels. The first level of triggering (L1 - level 1) uses hardware processors with information from their respective calorimeters (electromagnetic and hadronic) and their muon systems. Events that meet certain threshold requirements on the p_T or E_T of individual physics objects, as well as events with large scalar and vector E_T sums, will be transferred to the next stage of triggering. The L1T uses rough calculations and coarse granularity to identify and save collision events with large momentum transfer (high q^2 interactions). At this first level, the rate is reduced from an average of around 30 MHz down to 50 - 75 kHz.

Similar to the detector as a whole, the L1 trigger is comprised of several subcomponents associated with the different subdetectors: the bunch crossing timing, the L1 muon systems (CSC, DT, RPC), the L1 calorimetry (RCT, GCT), the global trigger (GT), and the L1T emulator, as shown in Fig. 3.9. The L1 trigger is limited to accessing only coarsely segmented data from the calorimeter and muon systems due to the rate requirements at L1 (reducing the 40 MHz LHC rate to around 100 kHz) and the 3 μs latency that the L1 has to decide whether

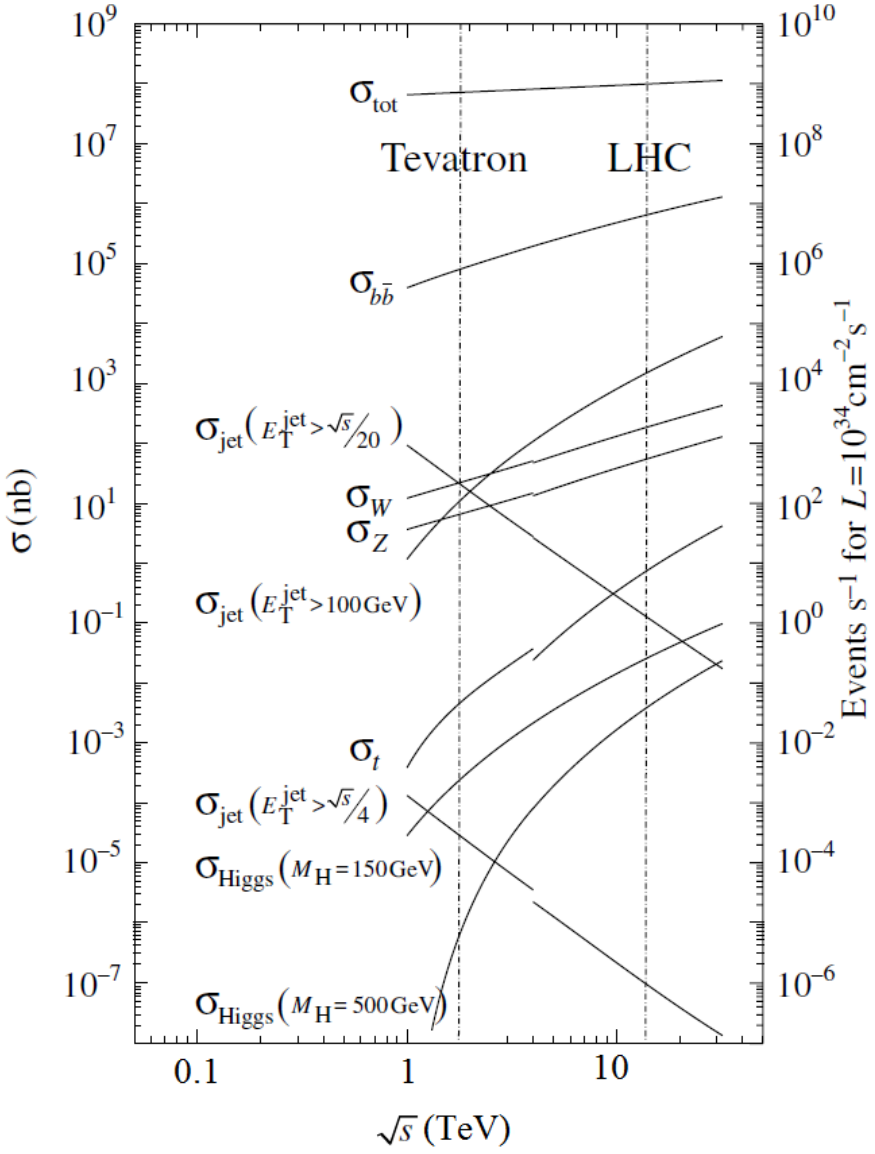

Figure 3.8: Cross section versus center-of-mass energy for several physics processes. The axis on the right gives the approximate number of events produced per second, assuming the LHC design instantaneous luminosity.

an event is kept or not. The GT has the ability to provide up to 128 trigger algorithms to select an event based on logical combinations of L1 objects, such as muons, jets, or calorimetry energy sums. In addition, there are 64 "technical

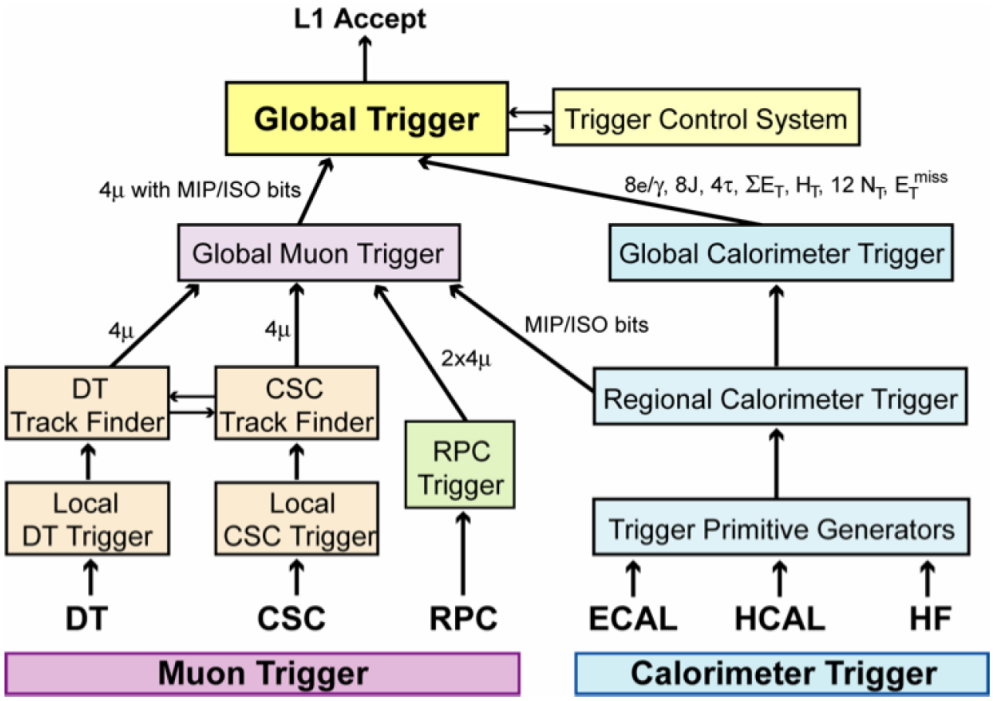

Figure 3.9: Level-1 trigger architecture [7].

triggers" that are used for detector diagnostics or monitoring [47].

The L1 trigger has a latency of 3.2 μs, after which the detector information from the event must either be dropped or sent to the front-end readout buffers [7]. Events that are retained undergo signal processing, zero-suppression, and data compression. As a final step in the online process, events are sent to a farm of CPUs where they perform software analyses from the second stage of triggering, the high-level trigger (HLT). At this stage, a cleaner particle signature is obtained through use of a fine-granularity measurement, which is necessary to achieve the desired rejection of unwanted events. Kinematic variables are calculated using all of the detector subsystems (that are necessary for a particular reconstruction). After the HLT, the total rate of writing data to media for storage should be a few hundred Hz, the maximum rate that

can be archived by the online computer farm.

Events that are accepted by the HLT are sent to the storage manager (SM) system. As the last component in the data-handling chain, the storage manager has two primary tasks [47]. The first function is to collect the events from the processor farm of HLT hardware, called the Filter Farm, and store the events in files for later transfer and processing. These data files are then assigned to different output streams. The files are routed according to which HLT paths are passed by a given event and by the definitions of the different streams. The grouping is usually determined based on offline usage (e.g., "physics" stream, "express" stream, calibration streams, etc.). The second main function of the SM is to act as an event server for calibration and monitoring purposes [47].

3.2.2 Magnetic Field

The magnet system is necessary to meet the detector requirements of achieving the desired momentum resolution of charged particles in the tracker and good performance of the muon system. The bending power of the magnet enables the determination of the sign and transverse momentum of charged particles. The main parameters of the CMS magnet system are given in Tab. 3.2. Figure 3.10 is a plot of the energy-to-mass ratio versus stored magnetic energy for several different detectors, and we see that the CMS magnet stands apart from previous and current detector magnets on both axes. The CMS detector has a superconducting solenoid with a high and (relatively) uniform field. With a free bore diameter of 6.3 m and an axial length of 12.9 m, the magnet is large enough to house the tracker and both calorimeters inside of it.

Table 3.2: Defining parameters of the CMS magnet system.

Property	CMS Solenoid
Peak field (T)	3.8
Inner diameter (m)	5.9
Outer diameter (m)	6.7
Axial length (m)	12.9
Operating current (kA)	18.5
Number of turns	2168
Stored energy (MJ)	2700

Additional bending of muon tracks outside of the central solenoid is achieved by a return yoke of three iron layers in the barrel and three iron discs in the endcap. The iron layers have a length of 13 m and extend out to a diameter of 14 m. The thickness of these three layers are 30 cm, 63 cm, and 63 cm. The iron discs in the endcap have a thickness of 25 cm, 60 cm, and 60 cm. The magnetic field is large enough to saturate the 1.5 m of lead [7], such that increasing the applied external field from the CMS magnet cannot further increase the magnetization of the iron.

3.2.3 Tracking System

We will now follow a particle from the interaction region to the edge of the CMS detector. The physics reach of the LHC has put strong requirements on the tracking system of the CMS detector. It must have superior momentum and vertex resolution to precisely measure all relevant tracks (e.g., to reconstruct narrow,

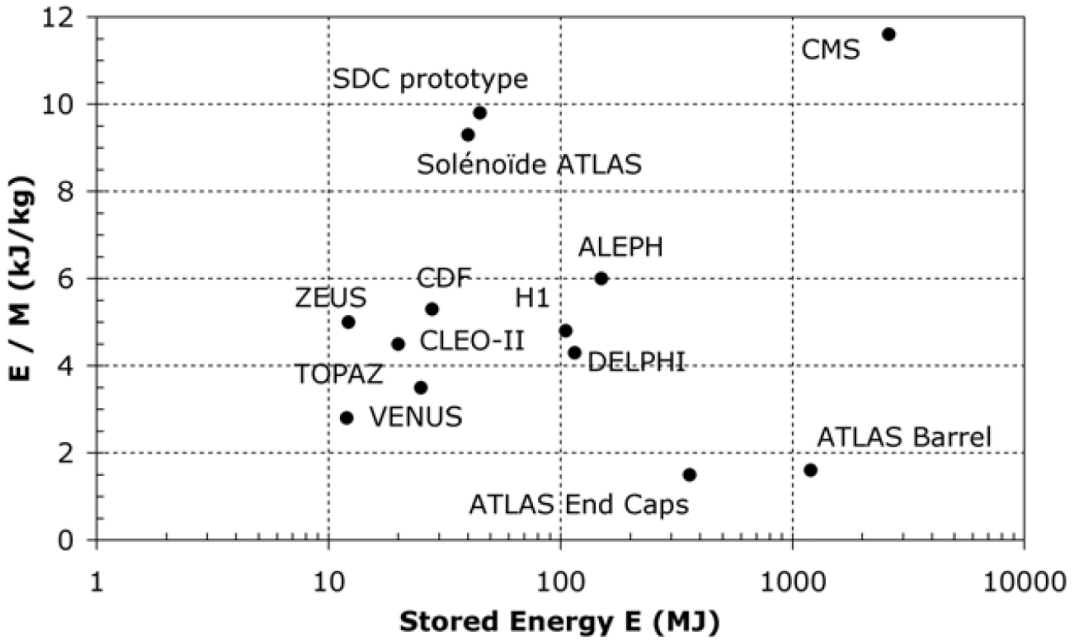

Figure 3.10: Magnetic energy to mass ratio plotted versus stored energy for different detectors [1]. CMS distinguishes itself on both axes over previous and current detector magnet systems.

heavy objects) and impact parameters (e.g., to tag τ's and b-jets). At nominal operating parameters, each bunch crossing of the LHC will produce 20 events on average, resulting in around 1,000 particles in the tracker [48]. This intense particle rate has direct implications on the design, material, and construction of the tracker.

In order for the tracker to perform well, it must maintain an occupancy at or below the level of a few percent, and it should not age or degrade too quickly in the high radiation environment. For these reasons, CMS employs a pixel detector at the closest location to the interaction point. Surrounding the pixel detector is a silicon strip tracker, as shown in Fig. 3.11. The pixel subdetector has three barrel layers, located at radii of 4.4 cm, 7.3 cm, and 10.2 cm. These are complemented by two end-cap disks on each side at a $|z|$ of 34.5 cm and

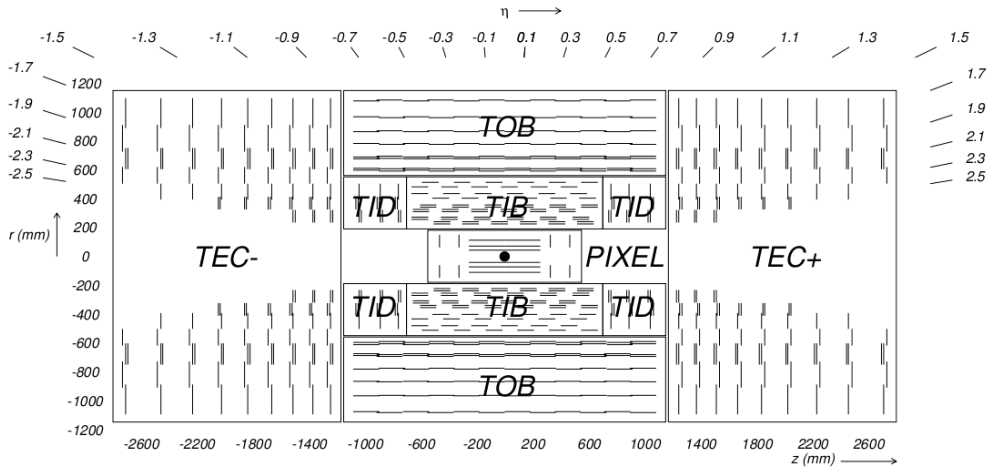

Figure 3.11: The CMS tracker. It is 5.4 m long, and it has an outer radius of 120 cm [7].

46.5 cm. With 66 million channels and about 1 m^2 of instrumented area, the pixel detector has a range of $|\eta| < 2.5$ [7].

The silicon strip tracker of CMS is a large and intricate device. It can be divided into three different subsystems. Closest to the interaction point, in the radial region between 20 cm and 55 cm, are the tracker inner barrel and tracker inner disks (the TIB and TID, respectively). The TIB has four cylindrical layers of silicon microstrip detectors with a cell size of 10 cm × 80 μm that was chosen to keep the occupancy at the level of 1% for design luminosity. The first two layers of the TIB are double-sided to give a stereo measurement with an angle of 100 mrad between the microstrip detectors. The TIB is able to provide a resolution of 23 - 34 μm in the $r - \phi$ direction and 23 μm in the z direction [49]. The TID serves as an end-cap to the TIB. It is composed of 3 disks, where each disk is made of three concentric rings of increasingly larger radius. The two smaller rings are stereo modules.

Table 3.3: The tracker system of CMS.

Property	CMS Pixel	CMS SST
Inner/outer barrel r (cm)	4.4/10.2	20/110
Inner/outer endcap $\|z\|$ (cm)	34.5/46.5	120/280
Active area (m^2)	1	210
Channels ($\times 10^6$)	66	9.6
$r-\phi$ resolution (μm)	10	23 - 52
z resolution (μm)	17	23 - 52

Further from the origin, extending from a radius of about 55 cm to 116 cm, is the tracker outer barrel (TOB). Since the particle flux is much smaller here than it is for the TIB, the microstrips can be larger (cell size 25 cm × 180 μm) without increasing the occupancy. The TOB has 6 layers in total; the first two are stereo modules with an angle of 100 mrad. Resolution in these layers is 35 - 52 μm in the $r-\phi$ direction and 52 μm in the z direction [7]. Lastly, the TOB is enclosed on each side by nine tracker end-cap (TEC) disks. Similar to the TID, each TEC disk is composed of rings. There are a total of seven rings, where the first, second, and fifth rings are stereo modules.

In total, the SST has almost 10 million channels and covers an active area of 210 m^2, making it the largest silicon detector in the world. Table 3.3 provides a summary of the CMS silicon detector.

3.2.4 Calorimeters

The momenta of particles are measured by the tracking and/or muon systems. However, this needs to be complemented by a measurement of energy, and this is provided by the calorimeters. The important properties of a calorimeter are its material, granularity, and coverage. The material determines the size of the calorimeter. The radial extent of the calorimeter should be large enough to encompass many radiation lengths (X_0) or interaction lengths (λ). The radiation (interaction) length is the distance an electromagnetic (hadronic) particle travels before its energy decreases to a fraction e^{-1} (~ 0.368) of its original value, due to showering. The granularity ($\Delta\eta \times \Delta\phi$) controls the channel occupancy as well as the precision to which the position of the energy deposition in the calorimeter can be known. Finally, the detectors should be hermetic (full 4π coverage in η and ϕ) to determine the amount of missing transverse energy in an event that may be ascribed to neutrinos or weakly interacting new particles.

There are two types of calorimeters employed by the CMS experiment: electromagnetic and hadronic. An electromagnetic calorimeter is designed to measure the energy of particles that interact primarily through the electromagnetic interaction, while a hadronic calorimeter is designed to measure the energy of particles that interact via the strong interaction. In addition, the calorimeters provide information on particle identification when used in conjunction with other systems. The electromagnetic calorimeter mainly serves to measure the energy of electrons and photons.

When a high-energy electron passes through the electromagnetic calorimeter, the calorimeter material will feel a high electric field. Equivalently, the electron will feel a force from the material, causing it to change direction. In this

process, the electron will emit a virtual photon to conserve energy and momentum. The photons in this medium have sufficient energy to produce electron-positron pairs. Each of the photons, electrons, and positrons produce more pairs as they continue to pass through the calorimeter material. The result is a cascade or "shower" of electromagnetic particles that share the energy of the original electron or photon. This continues until the cascade particles no longer have enough energy to produce pairs and they are absorbed into the material of the calorimeter.

Although muons have the same electric charge as electrons, their behavior through the electromagnetic calorimeter is quite different. Since the electromagnetic interactions are the same for the muon and the electron, the force from the electric field that the two feel are the same. However, the muon is 207 times more massive than the electron, meaning that the muon experiences a smaller acceleration and does not change direction significantly. In this way, a muon can pass through the electric fields without radiating photons and depositing much energy in the electromagnetic calorimeter.

One of the design goals of CMS was to construct a very high-performance electromagnetic calorimeter (ECAL). It should be able to accurately measure a wide range of energies, from 2 GeV up to a few TeV. The lower energy is important for the reconstruction of the Higgs boson decaying to b-jets; the upper energy is important to reconstruct the decay of new particle resonances. The photon energy range in between (20 - 80 GeV) is important for detecting the decay $H \rightarrow \gamma\gamma$ (if $m_{\text{higgs}} \sim 120$ GeV). In addition to having a large region of sensitivity, the electromagnetic calorimeter must also have exceptional energy resolution. This is important, for example, in the decay $H \rightarrow \gamma\gamma$, where we

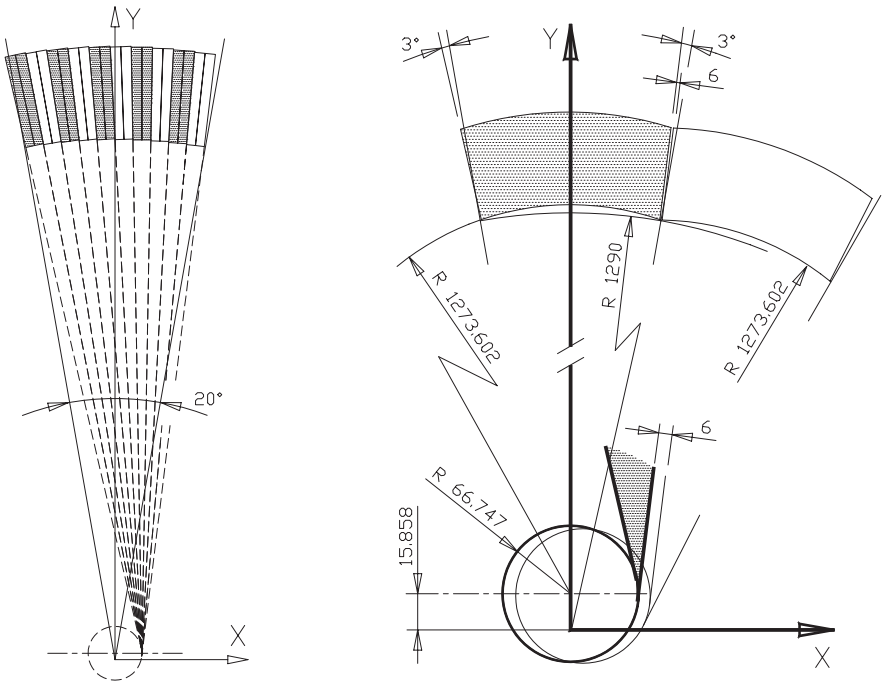

Figure 3.12: Tilt of ECAL crystals in transverse plane [8]. This tilt in ϕ prevents electromagnetic particles from escaping through gaps in the crystals.

search for a small resonance in the invariant mass of the two photons over a large continuum background.

The ECAL consists of nearly 76,000 lead tungstate ($PbWO_4$) scintillating crystals to measure energy depositions made from showering electromagnetic particles. The short radiation length (X_0 = 0.89 cm) of these crystals allows for a very compact calorimeter (about 25 X_0 for a 220 mm long crystal). In addition, lead tungstate crystals have a very small Molière radius (2.19 cm). This radius is a characteristic constant of a material that describes the transverse dimension of a fully-contained electromagnetic shower. Thus, small crystal cross-sections (about 22 mm × 22 mm) can be used to achieve a very fine granularity ($\Delta\eta \times \Delta\phi = 0.0175 \times 0.0175$) [8].

The ECAL barrel (EB) has a coverage of $|\eta| < 1.479$, and it can be broken down in the following way. First, it is divided in half along the z-axis into a (+) and (-) side. Each half contains 18 supermodules, arranged in ϕ, and each supermodule can be further subdivided into 4 modules, arranged in η. This hierarchy of components was designed to be versatile. Should the ECAL need servicing, it would be possible to remove the supermodule in question and correct the problem. Azimuthal cracks are minimized by the non-pointing geometry of the crystal array. The crystal axes are arranged such that they are tangential to a circle of radius 66.7 mm, as shown in Fig. 3.12. In addition, this circle is offset by 15.9 mm with respect to the beam axis. Together, these two designs correct for the 6 mm gap in ϕ between supermodules, insuring that the ECAL is fully covered in ϕ. The detector coverage in the η direction is similar. Here, the non-pointing geometry was created by inclining the crystals by -3° with respect to the line connecting the interaction point and the center of the front face of the crystal, as shown in Fig. 3.13.

The ECAL endcaps (EE) cover a range of $1.479 < |\eta| < 3.0$ and are located at $|z| = 314$ cm. Each EE is composed of two half-circle "Dees", which have a 5×5 crystal array structure as their basic unit, called a supercrystal. As for the EB, the crystal axes point away from the origin of the detector. However, here they are aligned in an $x - y$ grid and not in an $\eta - \phi$ grid [8]. Lastly, there is the preshower detector in front of the EE within a fiducial region $1.65 < |\eta| < 2.6$. The preshower detector causes the showering of electrons and photons before they reach the EE. This helps with the identification and differentiation between electrons and neutral pions, and it improves the position determination of the electrons and photons. The preshower detector is made up of a lead absorber in front of 2 silicon strip detector planes. A schematic of the ECAL subdetector is

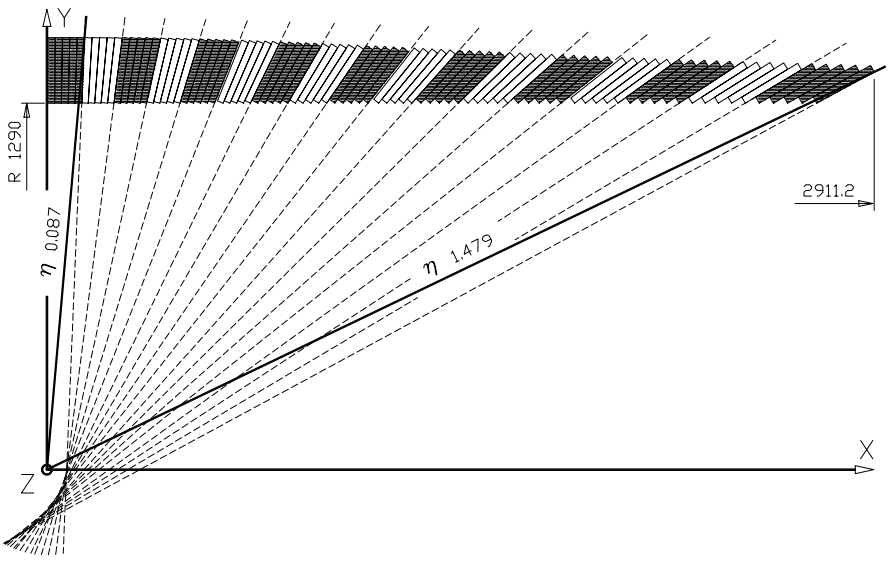

Figure 3.13: Longitudinal view of the barrel crystal geometry of the ECAL [8]. The non-pointing orientation of the crystals prevents electromagnetic particles from escaping through η gaps.

shown in Fig. 3.14.

The hadronic calorimeter (HCAL) measures the energy of particles that pass through the electromagnetic calorimeter and interact via the strong force. The HCAL is made of thicker layers of more dense material than the ECAL. When hadrons pass sufficiently close to the nuclei, there is a residual strong interaction between the hadrons and the protons and neutrons of the nearby nucleus. These interactions produce additional particles that share the energy of the original high-energy particle. Each of the produced particles will strongly interact with nearby nuclei, resulting in a cascade of particles similar to an electromagnetic shower. This will continue until the particles all begin to slow down and get absorbed into the calorimeter.

The CMS HCAL is a sampling calorimeter. Using alternating layers of absorber and scintillator material, the HCAL facilitates the strong interactions that

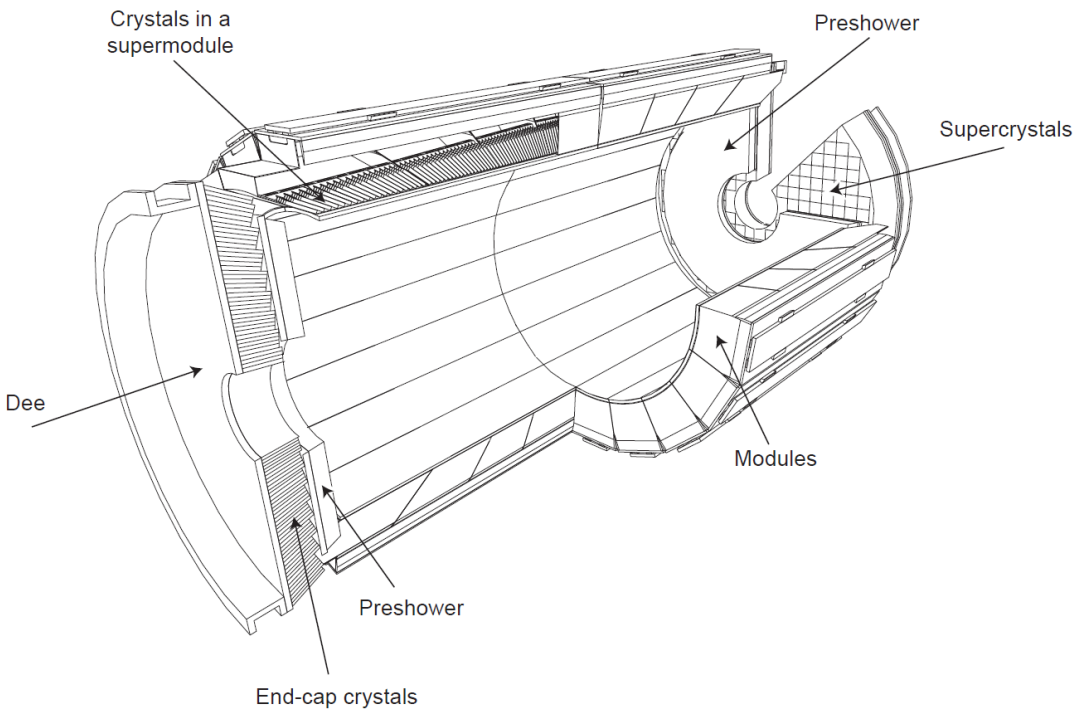

Figure 3.14: Layout of the CMS electromagnetic calorimeter showing the arrangement of crystal modules, supermodules, and endcaps, with the preshower in front [7].

cause the incoming hadrons to shower and measures the light pulse as particles pass through the calorimeter. The most crucial property for the HCAL is that it be hermetic to provide the best estimate of missing transverse energy. Careful consideration was made about which material would best satisfy all requirements of the HCAL. In the end, using brass interleaved with plastic scintillator for the entire HCAL was a good compromise of constraints, cost, and performance.

The hadronic calorimeter barrel (HB) covers the range of $|\eta| < 1.4$, and it consists of 2304 towers with a granularity of 0.087×0.087. The segmentation of the HCAL is shown in Fig. 3.15. The HB has a single longitudinal sampling. Even including the ECAL, the total interaction length of the calorimeters is only

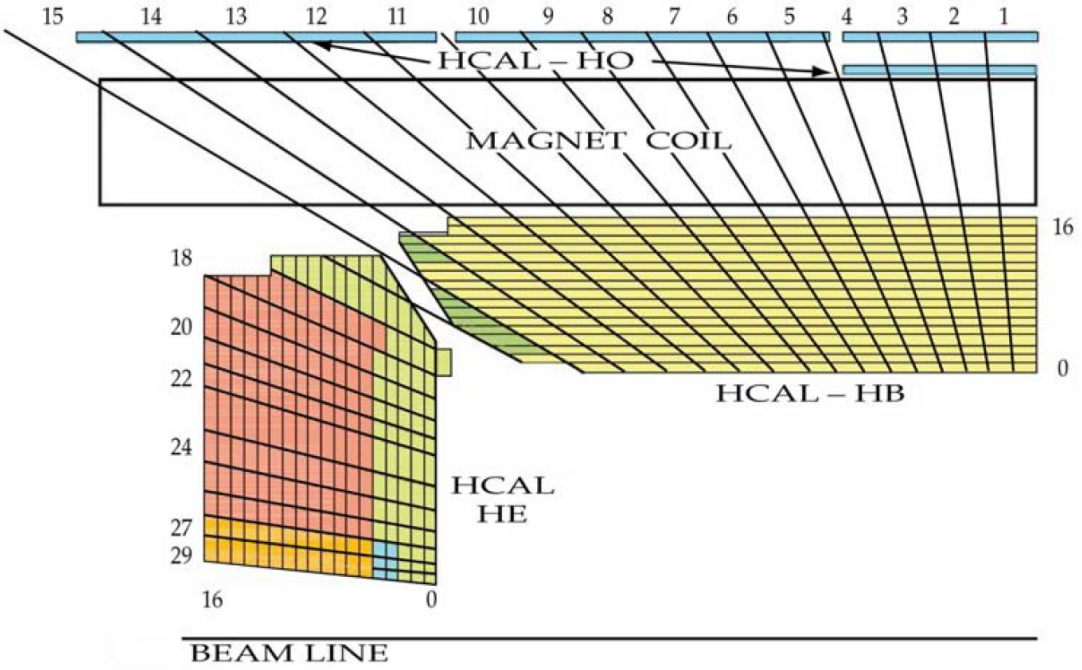

Figure 3.15: Lateral segmentation of the HCAL in the $r - z$ plane for one-fourth of the HB, HE, and HO detectors. The shading represents the optical grouping of scintillator layers into different longitudinal readouts [7].

7.2 λ. Therefore, an extra layer of scintillating detector was placed outside of the superconducting coil as a "tail-catcher". This hadron outer (HO) detector only covers the region $|\eta| < 1.26$, but it increases the calorimeter interaction length to over 10 λ. The HO reduces the non-Gaussian tails in the energy resolution, improves the missing transverse energy resolution of the detector, and provides better protection against "punch-through" of hadronic energy into the muon spectrometer [7].

The hadron calorimeter endcap (HE) provides coverage for $1.3 < |\eta| < 3.0$. The granularity is not constant across the entire HE. It varies from 0.087×0.087 at large radii (smaller η) to 0.35×0.17 closer to the beam axis (larger η). It is interesting to note that the brass used for the HE came from Russian artillery

shells [7]. To provide coverage out to even higher values of η ($3.0 < |\eta| < 5.0$), the CMS experiment uses its hadron forward (HF) calorimeter. Unlike the rest of the HCAL, the HF uses steel interleaved with quartz fibers, as opposed to brass and plastic scintillator. Since the radiation is larger at higher values of η (near the beam pipe), the HF is located 11 m away from the origin of the detector. It uses photomultipliers to detect Čerenkov light that is emitted in the quartz fibers.

The response, R, of a calorimeter to a hadronic shower is given by

$$R = e \cdot E_e + h \cdot E_h \tag{3.10}$$

where e and h are energy independent coefficients, and E_e (E_h) is the electromagnetic (hadronic) component of the shower. The ratio e/h describes how a calorimeter responds to leptons or photons versus hadrons. An ideal calorimeter would have $e/h \sim 1$. This is called a compensating calorimeter. The e/h is about 2.6 for the ECAL and 1.4 for the HCAL [50]. The deviation from a compensating calorimeter ($e/h \sim 1$) complicates the energy response of the calorimeters and makes their energy calibration more difficult.

3.2.5 Muon System

Many new physics signatures involve decays to muons. The momenta of these muons must be precisely measured over a wide range of values. Low momentum muons (1 - 10 GeV) are important for B-physics, mid-range momentum muons (10 - 30 GeV) may allow for the discovery of the Higgs boson and its decay, and high momentum muons (> 30 GeV) provide an avenue of discovery for new particle resonances with masses in the TeV range. For each of these

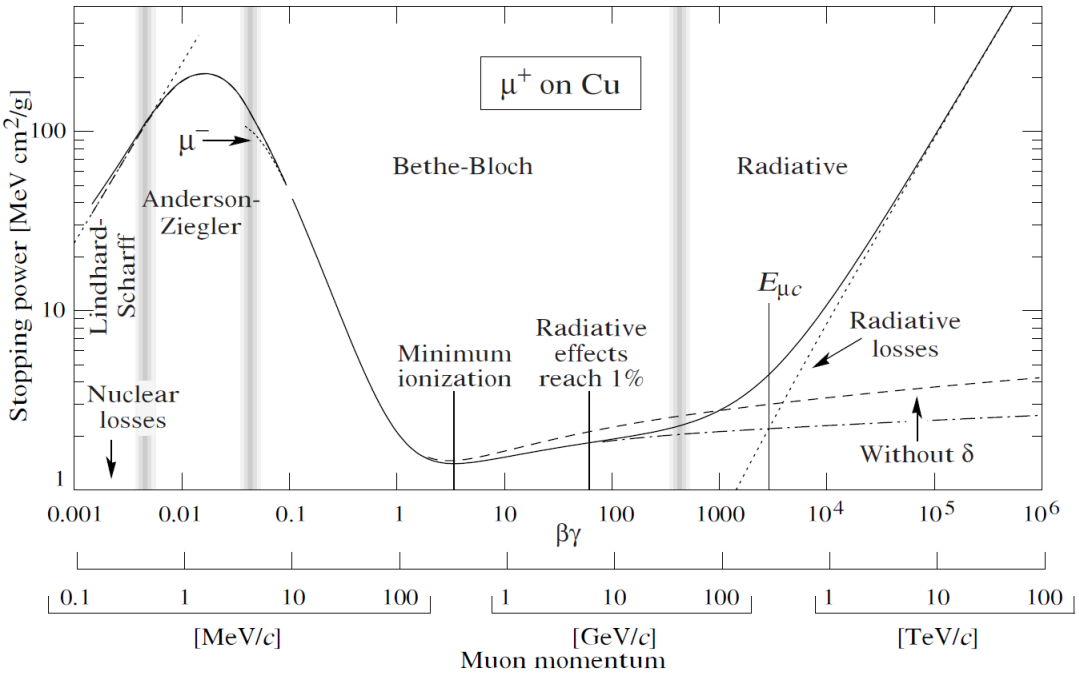

Figure 3.16: Stopping power (= $\langle -dE/dx \rangle$) for positive muons in copper as a function of $\beta\gamma = p/Mc$ over nine orders of magnitude in momentum (12 orders of magnitude in kinetic energy). Solid curves indicate the total stopping power. Vertical bands indicate boundaries between different approximations [1]. For a muon in the Bethe-Bloch minimum ionizing radiation, an electron of the same energy would be in the radiative region. This helps explain why muons do not shower like electrons in the ECAL.

ranges, it is necessary to distinguish muons that decayed promptly after the initial collision from muons that originate from a position some distance away from the collision event. A major background is the decay of pions or kaons to muons. These background muons usually have small momentum, and they can be reduced through matching track information to information from the muon systems.

As described in Sec. 3.2.4, most muons produced at the LHC will be minimum ionizing particles, or mips, meaning that their mean energy loss as they

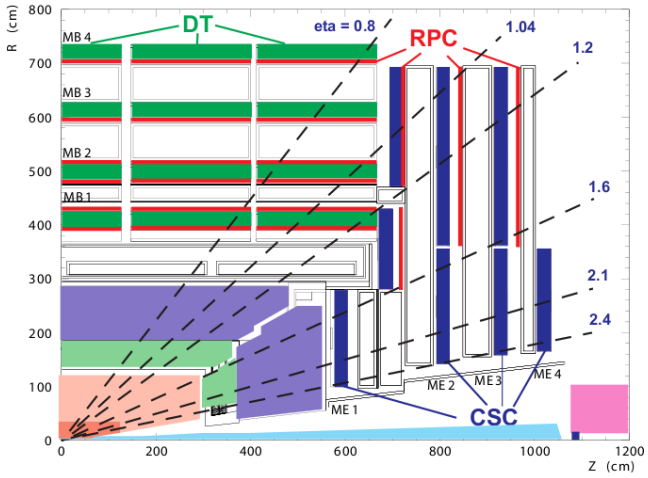

Figure 3.17: Cross-section of one quadrant of the CMS detector, with an emphasis on the muon system [7].

travel through the CMS detector will be close to the minimum possible (given by the Bethe-Bloch equation [1]). Figure 3.16 shows the stopping power for muons in copper as a function of $\beta\gamma$ and momentum. The majority of muons produced at the LHC will have momenta between 1 - 100 GeV, which is in the Bethe-Bloch energy loss regime. Note that electrons in the same momentum range will be in the radiative regime (due to their different masses). This is why muons are mips at the LHC and electrons are not.

Focusing on the muon system, the momentum resolution is strongly dependent on the bending power of the magnetic field and the amount of multiple scattering. The muons do lose some energy in the calorimeters, roughly 3 GeV on average, but this becomes negligible for muons with intermediate to high transverse momentum ($p_T > 10$ GeV) [51]. The p_T resolution is roughly given by

$$\frac{\sigma_{p_T}}{p_T} \sim \frac{\sqrt{\text{material in muon system}[X_0]}}{\int B d\ell} \tag{3.11}$$

where the material in the muon system is given in terms of the number of interaction lengths, X_0.

The barrel of the CMS muon spectrometer consists of five large wheels with four radial layers (or stations) for each wheel. These muon barrel (MB) stations are labeled MB1, MB2, MB3, and MB4, and they are located at radii of about 4.0 m, 4.9 m, 5.9 m, and 7.0 m. The muon end-cap (ME) also has four stations, labeled ME1 - ME4, as shown in Fig. 3.17.

For measurements and triggering of the muon spectrometer, CMS uses similar detector technology as current and previous experiments. Drift tube (DT) chambers are used for high-precision momentum measurements in the barrel ($|\eta| < 1.2$). In the two endcaps, where the particle flux and radiation are high ($|\eta| < 2.4$), cathode strip chambers (CSCs) are used. The CMS spectrometer has resistive plate chambers (RPCs) that provide a flexible trigger, precise timing (time resolution < 10 ns), and a position measurement that is orthogonal to the DTs and CSCs. RPCs are used in both the barrel and the endcap.

As described above, the magnetic field bending in the muon system is accomplished by means of an iron return yolk. Unfortunately, all of this iron leads to multiple scattering that significantly degrades the muon p_{T} resolution, as one can see from Eq. (3.11). The high magnetic field generated by the 3.8 T solenoid of CMS has the ability to accomplish significant track bending ability ($\int B d\ell$) in the barrel. That high magnetic field leads to better momentum resolution in the tracker. As shown in Fig. 3.18, combining the inner tracker and muon system measurements leads to a much better muon p_{T} resolution than either could obtain in isolation.

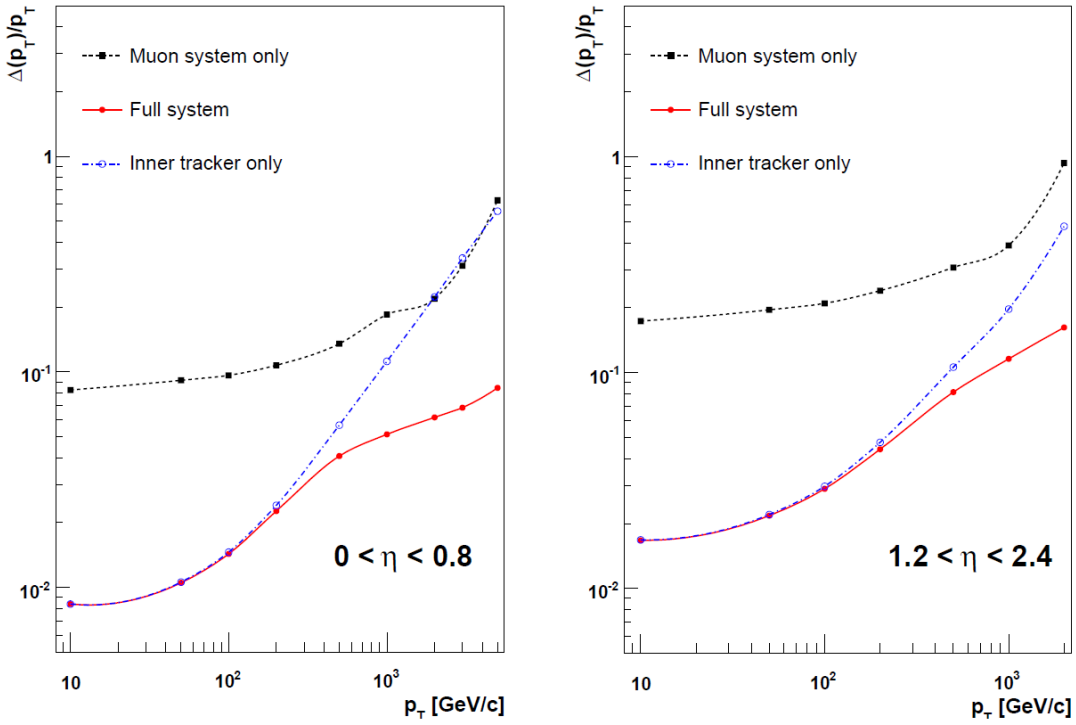

Figure 3.18: The muon transverse momentum resolution as a function of transverse momentum (p_T) using the muon system only, the inner tracking only, and both [7]. Left: $0 < \eta < 0.8$. Right: $1.2 < \eta < 2.4$.

CHAPTER 4

DATA QUALITY MONITORING

The CMS detector was built to make physics measurements using collision data collected from the LHC. It is of the utmost importance that the data taken by the CMS detector be of the highest possible quality. Any data that is lost or rendered unusable by detector malfunctions is lost forever. To maintain high operational efficiency and reliable data certification, data quality monitoring (DQM) has an important role within the CMS collaboration. From 2008 to 2010, I helped manage the level-1 trigger DQM. In addition, I participated heavily in both central and expert DQM shifts.

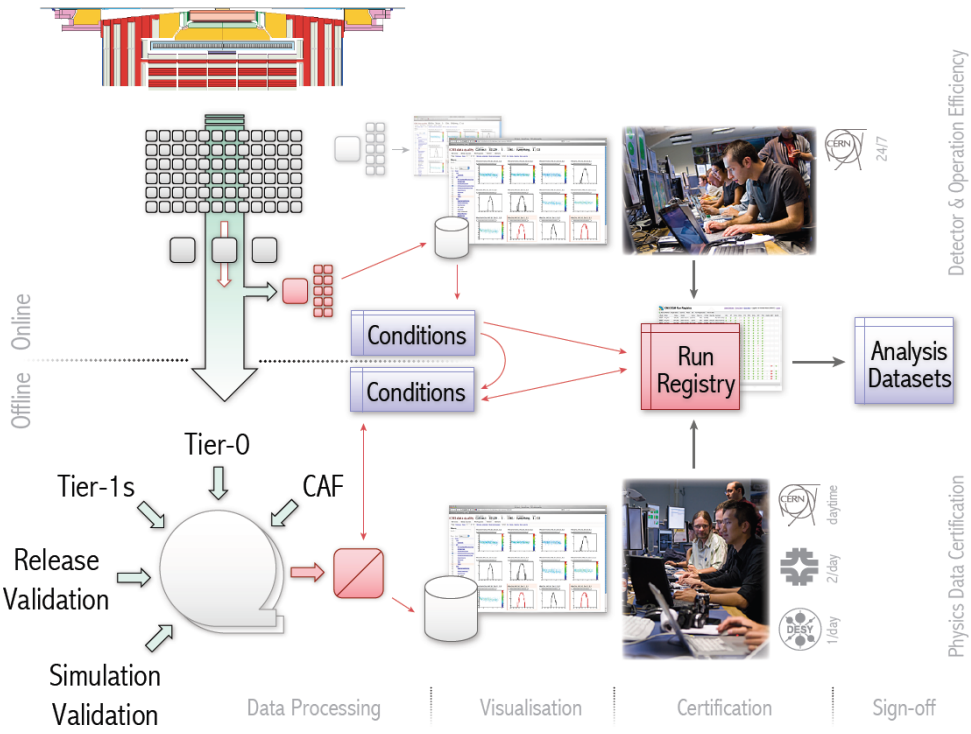

Figure 4.1: Overview of the data quality monitoring system [9].

Figure 4.1 gives an overview of the DQM system. Beginning at the CMS detector, some data are sent to the DQM tools and monitored by online shifters. All data are sent to the main computing facilities and processed there. Offline shifters monitor this data to detect any issues. The DQM system comprises [9]:

- tools for the creation, filling, transport, and archival of histogram and scalar monitor elements, with standardized algorithms for performing automated quality and validity tests on distributions;
- monitoring systems live online for the detector, trigger, data acquisition hardware status and data throughput, offline reconstruction, and validating calibration results, software releases, and simulated data;
- visualization of the monitoring results;
- certification of datasets and subsets thereof for physics analyses;
- retrieval of DQM quantities from the conditions database;
- standardization and integration of DQM components in CMS software;
- organization and operation of activities, including shifts and tutorials.

The value of the DQM system is its ability to quickly and accurately identify problems.

4.1 Online and Offline DQM

There are two levels of the DQM framework: online and offline. The goal of the online DQM is mostly centered on discovering problems with detector hardware. Similar to other detector subsystems (e.g., the electromagnetic calorimeter or the pixel detector), the online DQM system is started by the central data

acquisition system (DAQ) when the CMS is taking data and stopped when CMS is not. In this way, the DQM applications are an integral part of the data-taking process.

The online DQM system consists of distributions that come from two different sources: the DQM applications directly and HLT filter units. The DQM applications receive the event data from a special DQM monitoring data stream at a rate of 10-20 Hz. Typically, there is one application per detector subsystem (e.g., each muon, calorimeter, and trigger system). Apart from trigger filter requirements specific to each DQM application, events receive no special sorting or handling [9]. The HLT filter units produce some histograms as well. In the filter units, the DQM consumers have access to all events processed by the HLT, even events that will eventually be dropped. This is critical for trigger monitoring to compute rates and rejection factors for each trigger algorithm and filtering stage. Identical histograms across several filter units are summed and sent to a storage manager proxy server, which saves and ships the histograms to consumer applications.

Whereas the focus of the online system is more on detector performance, the offline DQM system is focused more on reconstruction. After events are fully processed and reconstructed through the CMS software, the increased statistics available offline may reveal subtle problems not found online, the reconstruction process may introduce errors, or both. The offline DQM system is separated into two steps. The first step consists of storing the DQM histograms with the processed events of the CMS data. In this way, all of the same histograms are summed to form a partial result when the CMS data processing system merges output files together. The second step is focused on "harvest-

ing" the histograms. In this step, the histograms are extracted from the event data files and summed over a continuous data taking period to provide the full statistics for that running period.

In both the online and offline, the DQM applications package the histograms and additional information (e.g., when the data was taken) in the form of "monitor elements". The DQM applications perform algorithms, called quality tests, that run checks on the data for known problems. The monitor element data are uploaded to a central DQM GUI web server for visualization in real time [52]. Based on the results of the quality tests, there are alarms to warn people about problems. The tracking and bookkeeping of CMS data taking periods is managed via the Run Registry. The Run Registry is a database with a front-end web application; it serves as both a user interface and a persistent store of the information [9]. Along with the DQM GUI, it is one of the major tools used by shifters to monitor and categorize the state of the detector at different times.

4.2 Level-1 Trigger DQM

For most of 2009 and 2010, my DQM duties focused on the management of the L1T data quality monitoring package. Monitoring the trigger is especially important, as the trigger is the first system to integrate the detector, and it is the most sensitive gauge of detector problems. Part of that work included the design and implementation of the L1T workspace so that the trigger shifter and the central DQM shifter had necessary and sufficient information to immediately spot problems with the trigger. It was important to balance exactly how much information was presented to the shifter; too little is not useful, and too

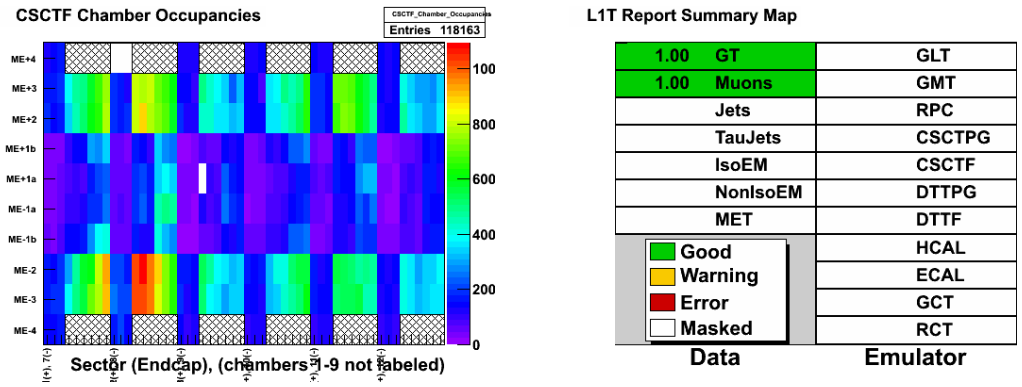

Figure 4.2: Two of the L1T plots seen by the shifter in the DQM GUI. Left: Chamber occupancy plot of the track-finding algorithm of the CSC muon system. Note that the plot is rendered to indicate where one should not expect data (hashed region). Right: Global report summary of the L1T. We can see the status of each L1 object that is not masked in the current run.

much can be distracting.

To aid the shifters, the DQM monitor elements can be rendered with different options to draw attention towards or away from certain parts of the histograms. This is achieved using different plugins with the DQM system to make understanding plots more intuitive. For example, regions that are uninstrumented (i.e., they will never show data) can be rendered in a way that makes it obvious that the shifter should not expect data. Also, the global summary of the L1T seen by the shifter can help him or her quickly survey the L1T subsystem. Here, one can see the quality of the L1 objects (e.g., muons, jets, MET) to determine if there are any issues and use this to certify a certain data-taking period as good or bad. An example of the use of these plugins and the L1T global summary are shown in Fig. 4.2. In the global summary, some of the objects, such as jets and MET, are masked. The masking of different objects is easily configurable, and the objects can be quickly reinstated.

In addition to the plugins described above, the DQM system allows the use of quality tests to be performed on monitor elements. Automated quality tests are designed to find a host of problems: hot, cold, or otherwise bad channels, data integrity, noise and pedestal levels, occupancy, timing problems, reconstructed quantities, trigger issues, and detector-specific known problems. The quality tests are defined using a generic quality testing module, and they are configured using an XML file [9]. If a monitor element fails a quality test, the DQM GUI will raise an alarm. This includes, but is not limited to, highlighting the monitor element in red to draw the attention of the shifter. To further ensure stable performance of the trigger system, I also helped develop scripts to access L1T and HLT rates from the CMS Web Based Monitoring (WBM) system database [53] to monitor rates over long periods of time (several runs). This allows one to spot more subtle issues that may arise with the trigger.

4.3 DQM Shifts

In order to ensure that CMS is operating as efficiently as possible, there is always someone on shift for the DQM system when the CMS detector is collecting data. To monitor the online DQM at the site of the CMS detector, there are online shifts 24/7 during detector operation. From November 2008 until February 2010, I took more than 30 DQM shifts, giving me a better understanding of the DQM system and the DQM group as a whole.

The goal of the online DQM shifter is to quickly identify problems with detector performance or detector integrity during a run and notify the relevant expert to fix the problem immediately. In some cases, this may require stopping

the data taking to ensure that the data are of high quality and optimal operation efficiency is achieved. The offline DQM shifter produces data certification for all relevant datasets, which include prompt reconstruction after the data was taken or subsequent iterations of re-reconstruction that may take place to improve alignment, calibration issues, and/or bug fixes.

The DQM shifters of CMS are given four major tasks: (1) make sure all the DQM applications are working, as any application not visible in the GUI could indicate that the application may have crashed and needs to be restarted; (2) inspect all of the relevant histograms in the GUI, follow shift instructions, and contact expert in case of problems; (3) provide bookkeeping of all relevant runs using the Run Registry; (4) produce a summary of shifts and report any issues. In case of persistent problems or issues outside the depth of the shifter's experience, they are to contact the DQM expert on call.

The on-call DQM expert is there to make sure that DQM operations proceed smoothly. From December 2009 until September 2010, I took more than 50 days of shifts as the expert. As an on-call expert, I was responsible for the following:

- providing 24-hour phone support to online shifters at P5;
- helping to improve the shift instructions and procedures that are followed by the DQM shifters to reduce problems from future shifters;
- reporting at the daily run meetings every morning and the weekly run meetings every Friday evening about the status of DQM, any problems encountered, how they were solved, etc.;
- producing weekly shift summaries with a list of problems experienced over the weeks, any open issues encountered, and a range of recent runs to serve as input to the Physics Validation Team for certification;

- debugging specific issues with the DQM tools (e.g., DQM GUI, Run Registry, event display, etc.) or knowing which expert to contact;
- giving the weekly DQM tutorial to train future shifters.

For the first year of data-taking, there was a pool of 11 on-call experts, and only two of them were graduate students (I was one of them). Among this small group, I was part of a smaller sub-group that was given additional privileges to control DQM processes in case the GUI expert was not available and any processes needed to be restarted. This position requires the on-call expert to be on-site at the CMS detector often, and it is important to get to know many of the experts who spend much of their time there to make sure the detectors are running properly.

CHAPTER 5

DATA AND SIMULATION

For this analysis, we use collision data recorded by the CMS detector. In order to search for an excess of events in the data beyond the standard model, we need to have an estimate of just how large those standard model backgrounds will be. In this chapter, we discuss what data are used and how it was certified, and we describe the simulation of both standard model and W' events using Monte Carlo method generators.

5.1 Data and Certification

For each data-taking period, both the online and offline DQM shifters will mark a run as "good" or "bad" to be used for physics analyses. After this, experts of the various detector and software systems will review the certification and make changes, if necessary. As described in the previous section, the amount of data collected is reported in terms of integrated luminosity. There are three important numbers that are relevant for data-taking. First, there is the delivered luminosity; this is the data (related to the number of collisions) provided by the LHC. Second, there is the recorded luminosity; this is the data that is recorded by a particular experiment (CMS, in this case). The difference between recorded and delivered luminosity is mostly due to detector downtime, such as a subdetector needing to be restarted. Finally, there is the certified luminosity; this is the amount of data that was certified "good" by CMS to be used for physics analyses. Figure 5.1 shows how these three integrated luminosities increased over time in 2010. The data used in the analysis of this dissertation was recorded by the CMS detector between March 30 and October 31 of 2010. The majority of the

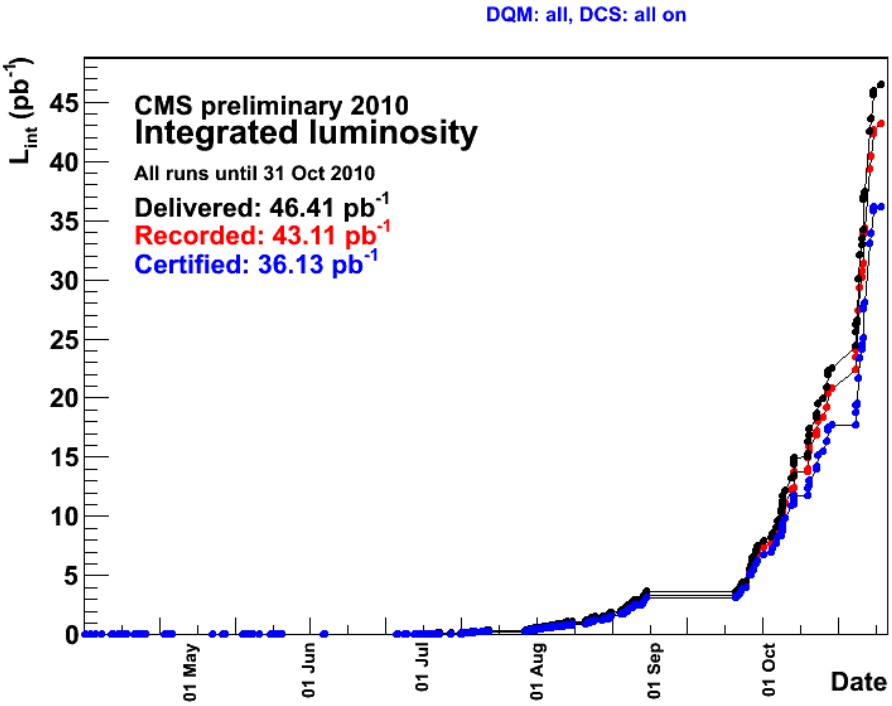

Figure 5.1: Integrated luminosity at CMS as a function of time (date). During 2010, the LHC delivered 46.41 pb^{-1}, CMS recorded 43.11 pb^{-1} (93% efficiency), and the DQM group certified 36.13 pb^{-1} as suitable for physics analyses (84% efficiency).

data, roughly 90%, was collected in the last month of running, after bunch trains were commissioned by the LHC. The analysis is based on data corresponding to an integrated luminosity of 36.1 pb^{-1}.

5.2 Simulation of Signal and Background Processes

The main sources of backgrounds to $W' \to e\nu$ are the standard model W boson, multi-jet events, $t\bar{t}$, and $W \to \tau\nu$. Table 5.1 gives a summary of the simulated processes, the generator used in the simulation, the kinematic requirements or assumptions, and the cross section. All samples use either the PYTHIA6 gen-

erator [54] or the MADGRAPH generator [55]. The geometric and kinematic acceptances are calculated using a GEANT-based full simulation of the CMS detector [56].

Decays of W bosons to an electron and a neutrino are the most important simulated background for this analysis. We use a PYTHIA6 sample of 10 million events, corresponding to an integrated luminosity of 498 pb^{-1}. For this sample, the statistics in the high p_{T} bins (e.g., the electron p_{T}) is quite low, consistent with data. Since a W' signal would likely show up in the high p_{T} tail, it is important to have a good understanding of this kinematic region. To have the best estimate of the high p_{T} tail of the $W \to e\nu$ distribution, we use a special sample of $W \to e\nu$ events with $p_{\text{T}}^{ele} > 100$ GeV.

For signal samples, we simulate the W' decaying into an electron and a neutrino for a range of W' masses using the PYTHIA6 generator, based on a leading order cross section. For each W' mass, we generate 11,000 events, ranging from $m_{W'} = 0.6$ TeV to $m_{W'} = 1.5$ TeV in steps of 0.1 TeV, along with a sample with $m_{W'} = 2$ TeV. The PYTHIA6 cross sections for $pp \to W' \to e\nu$ range from 6.3 pb for a relatively light (and already excluded) $m_{W'} = 0.6$ TeV to 11.5 fb for the heaviest investigated mass of 2 TeV. All LO cross sections are scaled to NNLO using a k-factor of roughly 1.3, with a slight dependence on the mass [57, 58]. The cross sections, k-factors, and cross section uncertainties for the different W' samples are given in Tab. 5.2.

Table 5.1: Simulation of background samples.

Process	Generator	Selection	σ(pb)
$W \to e\nu$	PYTHIA6	$\lvert\eta_e\rvert < 3.0$	10438 (NNLO)
$W \to \mu\nu$	PYTHIA6	$\lvert\eta_\mu\rvert < 3.0$	10438 (NNLO)
$W \to \tau\nu$	PYTHIA6	$\lvert\eta_\tau\rvert < 3.0$	10438 (NNLO)
$W \to e\nu$	PYTHIA6	$p_{\mathrm{T}}^{ele} > 100$ GeV	1.187 (LO)
$Z/\gamma^* \to e^+e^-$	PYTHIA6	$m_{ee} > 20$ GeV	1666 (NNLO)
$Z/\gamma^* \to \mu^+\mu^-$	PYTHIA6	$m_{\mu\mu} > 20$ GeV	1666 (NNLO)
$Z/\gamma^* \to \tau^+\tau^-$	PYTHIA6	$m_{\tau\tau} > 20$ GeV	1666 (NNLO)
$Z + \gamma \to \nu\nu + \gamma$	PYTHIA6	$m_{\nu\nu} > 45$ GeV, $p_{\mathrm{T}}^{\gamma} > 25$ GeV	2.68 (LO)
$t\bar{t}$	MADGRAPH	$m_t = 173$ GeV	157.5 (NLO)
single t	MADGRAPH	s-channel production	0.99 (LO)
single t	MADGRAPH	t-channel production	21 (LO)
single t	MADGRAPH	tW-channel production	10.56 (LO)
WW	PYTHIA6	-	43 (NLO)
WZ	PYTHIA6	$m_{\ell\ell} > 40$ GeV	18.2 (NLO)
ZZ	PYTHIA6	$m_{\ell\ell} > 40$ GeV	5.9 (NLO)
multi-jet	PYTHIA6	$\hat{p}_{\mathrm{T}} > 15$ GeV	8.8×10^8 (LO)
γ+jets	PYTHIA6	$\hat{p}_{\mathrm{T}} > 15$ GeV	1.9×10^5 (LO)

Table 5.2: Simulation of $W' \to e\nu$ signal samples.

$m_{W'}$ (TeV)	LO σ(pb)	k-factor (NNLO)	σ uncertainty (%)
0.6	6.28	1.32	6.6
0.7	3.23	1.32	7.6
0.8	1.838	1.32	8.4
0.9	1.06	1.31	9.4
1.0	0.64	1.31	10.4
1.1	0.397	1.30	11.2
1.2	0.257	1.30	12.1
1.3	0.167	1.29	13.0
1.4	0.106	1.28	13.6
1.5	0.077	1.28	14.4
2.0	0.0115	1.26	17.1

CHAPTER 6

PHYSICS OBJECT RECONSTRUCTION

To make physics measurements, CMS must be able to accurately identify different particles and measure their properties. It achieves this goal by exploiting the different layers of detector material, as shown in Fig. 6.1. Those particles created in the initial collision of the protons will either decay into lighter particles or they will travel outward through the detector. Particles with electromagnetic charge will leave tracks of their passage through the silicon pixels and silicon strip tracker; this information is used to determine their momentum. Next, the particles will encounter the electromagnetic calorimeter. The ECAL initiates electromagnetic showers from the incoming electrons and photons, causing them to deposit their energy.

Due to the confining nature of Quantum Chromodynamics, colored objects, such as quarks and gluons, cannot be observed. The process of confining the colored objects (quarks and gluons) to colorless objects (hadrons) produces a spray of particles in the detector. This spray of particles is called a jet. Jets will deposit some of their energy in the ECAL, but they will deposit the majority of their energy in the HCAL.

Although muons carry the same electric charge as electrons, their large mass (compared to electrons) and momentum between a few GeV and a hundred GeV cause them to deposit very little energy in the calorimeters at LHC energies (they do leave a track in the tracker). Thus, the only particles to routinely make it past the HCAL and reach the muon chambers are muons. This fact helps identify muons as they pass through the detector. The only other particles that can reach the muon chambers are hadrons that occasionally "punch-through"

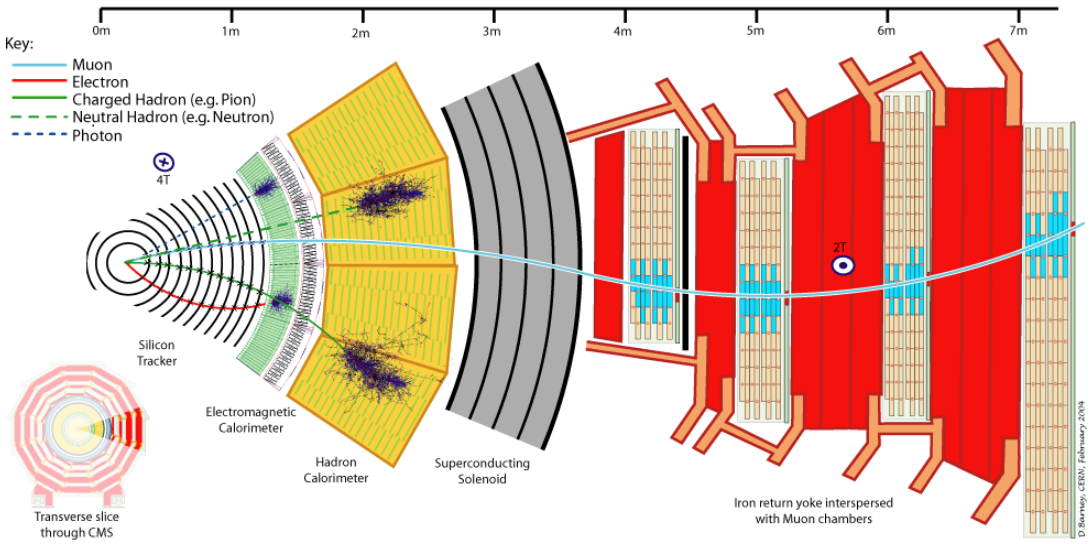

Figure 6.1: Transverse slice of CMS showing the different detector layers and the trajectories of muons, electrons, charged / neutral hadrons, and photons as these particles travel outward from the collision point.

the calorimeters.

Since we do not know the longitudinal momentum of the colliding partons (some fraction of the proton momentum), the initial momentum along the beam axis is unknown. However, the initial momentum transverse to the beam axis is zero. If there is any net transverse momentum in a collision event, this missing transverse energy can be used to infer non-detectable particles, such as the neutrino.

For this analysis, we are interested in the decay $W' \rightarrow e\nu$. As such, we will focus on the reconstruction and identification of electrons as well as the calculation of the missing transverse energy, which is used to infer the neutrino.

6.1 Electrons

6.1.1 Reconstruction

The reconstruction of electrons begins with the clustering of energy deposits in the electromagnetic calorimeter. CMS employs a hybrid (island) clustering algorithm for energy deposits in the barrel (endcap). The hybrid algorithm takes a fixed bar of 3 or 5 crystals in η and dynamically searches for energy deposits in the ϕ direction. The island algorithm begins by finding a seed (crystals with energy above some threshold). It scans crystals adjacent to the seed position, starting in the ϕ direction and then searching in the η direction. The scanning process continues until there is a rise in energy above some threshold [7].

The energy reconstruction begins by grouping basic crystal energy deposits together to form a hybrid super-cluster (if using the hybrid clustering algorithm in the barrel). The energy of the super-cluster is corrected to account for the spread of energy over multiple crystals. The correction depends on the number of crystals in the seed cluster that comprise a given super-cluster. This energy estimate is also corrected to remove any residual η dependence.

So far, this reconstruction would apply equally well to both electrons and photons, as both deposit their energy in the electromagnetic calorimeter. The difference between them (from the point of view of detector reconstruction) is whether or not the super-cluster has a track associated (matched) with it. The matching of the track and super-cluster is accomplished by looking at the angular separation (ΔR) between two objects located at positions (η_1, ϕ_1) and (η_2, ϕ_2)

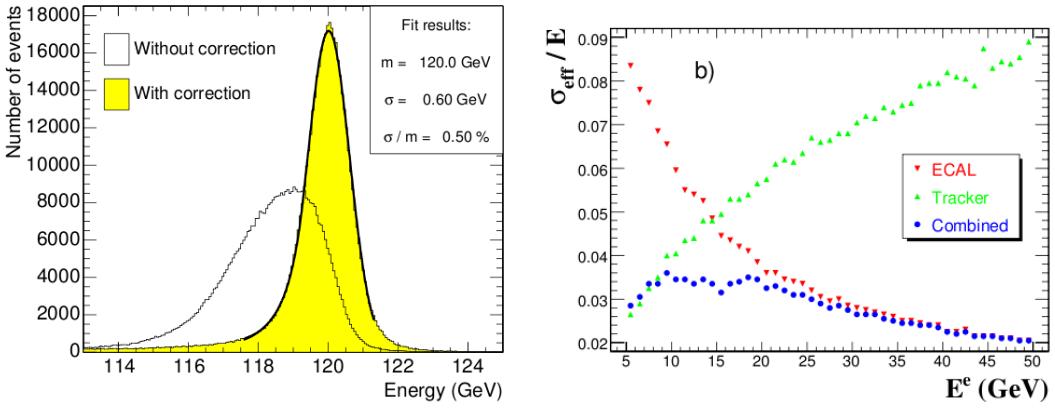

Figure 6.2: Left: Distribution of energy before (un-shaded) and after (shaded) energy corrections for electrons with an energy of 120 GeV. Right: Energy resolution uncertainty due to the ECAL and tracker individually, and the combined ECAL and track error versus electron energy.

where

$$\Delta R = \sqrt{(\eta_1 - \eta_2)^2 + (\phi_1 - \phi_2)^2}. \tag{6.1}$$

If a super-cluster has an associated track, then the energy of the electron is given as the error-weighted average of the corrected super-cluster energy and the magnitude of the track momentum (since the mass of the electron is negligible when compared to GeV energies). Using simulations, the energy resolution (before and after corrections) of 120 GeV electrons and the dependency of both the tracker and the ECAL resolution on electron energy is given in Fig. 6.2. Note that the error-weighted average of both the ECAL energy and track momentum produces the smallest error.

One of the difficulties of electron reconstruction is that the electrons can radiate in the tracker material in front of the ECAL due to bremsstrahlung radiation. Figure 6.3 shows an illustration of an electron as it radiates photons when traveling through the tracker layers. We see that an electron can leave multiple

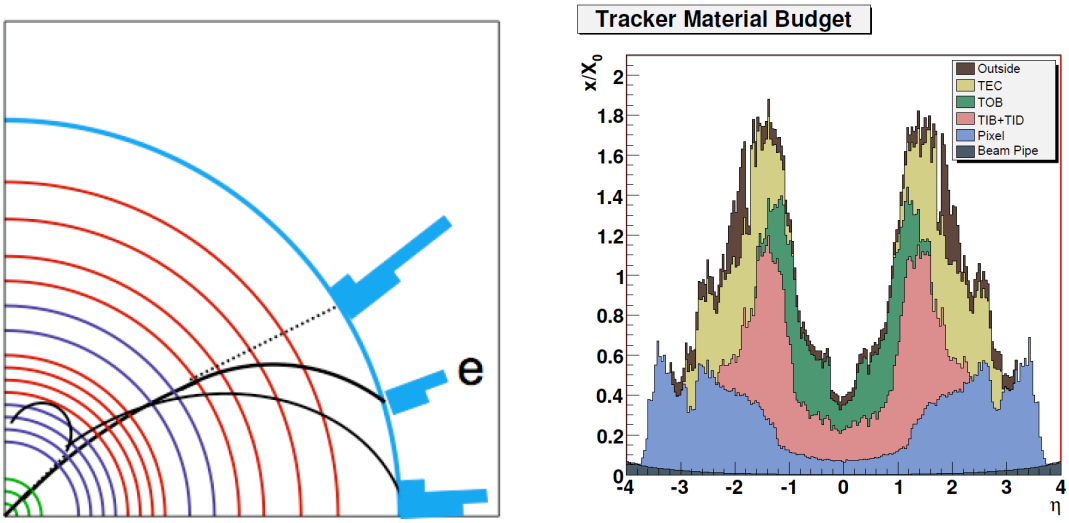

Figure 6.3: Left: Illustration of one quarter of the transverse view of CMS as an electron radiates. Right: Material budget in units of radiation length as a function of pseudorapidity for the different subdetectors [7].

disjoint energy deposits. The figure also shows the material budget of the CMS tracker in units of radiation length. The radiation affects both the energy and momentum measurement, and this effect depends on the material thickness. In an effort to take into account bremsstrahlung radiation losses, CMS employs a Gaussian Sum Filter (GSF) track fit. This fit uses a realistic model of energy loss of electrons due to bremsstrahlung, the Bethe-Heitler model [59], and approximates the energy loss distribution as a mixture of Gaussian distributions. Different components of the mixture model different degrees of hardness of the bremsstrahlung in the layer under consideration [60]. Electrons reconstructed in this way are called GSF electrons, in CMS nomenclature. The GSF fit allows for a good momentum resolution at the vertex while also providing a meaningful estimate of the momentum at the outermost part of the tracker [60]. The difference between these two momenta can then be used as a measure of the energy that the electron has radiated.

6.1.2 Identification

There are three main sources of electron candidates that are reconstructed with the CMS detector: prompt electrons, non-prompt electrons, and fake electrons. Prompt, high-energy electrons come from the decay of W bosons, Z bosons, τ leptons[1], or new physics particles (e.g., W' bosons). These are the signal electrons that are of the most interest to us. Non-prompt electrons arise from sources such as a heavy quark decaying to an electron. Although these electrons are usually not isolated (there is a significant amount of nearby electromagnetic and/or hadronic energy deposits), the kick from the quark decay might knock the electron out of the jet enough for it to appear isolated. Fake electrons are not electrons; they are due to a coincidence of a jet depositing a large amount of energy in the ECAL and a nearby (matched) single, high-p_{T} track that is then reconstructed as an electron. Non-prompt and fake electrons are a background source of electrons that we want to reduce as much as possible.

One way to reduce the background from these unwanted electron candidates is to place quality criteria on the electron objects. The electrons of most interest to us in this analysis, those coming from the decay of W' bosons, typically have very high momenta (several hundred GeV in energy). To identify these electrons, we use a dedicated selection that is designed to ensure high efficiency for these electrons and a high rejection of unwanted electron candidates from multi-jet processes. This selection includes the following electron object variables, also given in Tab. 6.1, to discriminate between signal and background sources of electrons:

- E_{T}: The corrected super-cluster energy of the electron multiplied by $\sin\theta_{trk}$,

[1]Electrons from the decay of τ leptons from semi-leptonic b/c-decays are considered non-prompt.

Table 6.1: The high-energy electron selection applied for electron identification.

Variable	Barrel	Endcap
E_{T}	> 30 GeV	> 30 GeV
η_{SC}	$\lvert\eta_{SC}\rvert < 1.442$	$1.560 < \lvert\eta_{SC}\rvert < 2.5$
isEcalDriven	true	true
$\Delta\eta_{in}$	$\lvert\Delta\eta_{in}\rvert < 0.005$	$\lvert\Delta\eta_{in}\rvert < 0.007$
$\Delta\phi_{in}$	$\lvert\Delta\phi_{in}\rvert < 0.09$	$\lvert\Delta\phi_{in}\rvert < 0.09$
H/E	< 0.05	< 0.05
$\sigma_{i\eta i\eta}$	n/a	< 0.03
$E^{2\times5}/E^{5\times5}$	> 0.94 OR $E^{1\times5}/E^{5\times5} > 0.83$	n/a
EM + Had Depth 1 Isolation	$< 2 + 0.03\times E_{\mathrm{T}}$	< 2.5 for $E_{\mathrm{T}} < 50$ else
		$< 2.5 + 0.03 \times (E_{\mathrm{T}} - 50)$
Had Depth 2 Isolation	n/a	< 0.5
Track Isol: Track p_{T}	< 7.5	< 15

where θ_{trk} is the polar angle of the electron track measured at the inner tracker layer and then extrapolated to the interaction vertex.

- η_{SC}: The pseudorapidity of the electron's super-cluster. Note this is with respect to the center of the CMS detector. So, its use is for fiducial cuts due to detector effects, and it should not be used to calculate four-momenta used in physics results, such as mass calculations.

- η: The pseudorapidity of the electron's track, as measured at the inner layer of the tracker and then extrapolated to the interaction vertex. This should be used for calculating the four-momentum of the electron and for

all physics results, but it is not used for detector fiducial cuts.

- IsEcalDriven: When reconstructing electrons, the electron can be seeded (reconstruction process begun) for the ECAL super-cluster or from tracks in the tracker. Currently, while useful for low energy or non-isolated electrons, tracker-driven electrons are not useful or validated for high energy electrons. Hence, we require that the electron be ECAL driven (it can and often will be tracker driven as well, as it can be found by both algorithms).
- $\Delta\eta_{in}$ and $\Delta\phi_{in}$: The difference in η and ϕ between the track position as measured in the inner layer of the tracker, extrapolated to the interaction vertex and then extrapolated to the calorimeter, and the η and ϕ of the super-cluster.
- H/E: The ratio of the hadronic energy of all deposits in a cone of radius $\Delta R = \sqrt{\Delta\eta^2 + \Delta\phi^2} < 0.1$ centered on the electron position in the calorimeter to the electromagnetic energy of the electron super-cluster. This variable provides useful discrimination between electrons and jets, as electrons will deposit little energy (if any) in the hadronic calorimeter, unlike most jets.
- $\sigma_{i\eta i\eta}$: A measure of the spread in η in units of crystals of the electron's energy in the 5×5 block centered on the seed crystal. A large spread in the energy deposition by the electron candidate indicates that the candidate is most likely a jet.
- $E^{1\times5}/E^{5\times5}$ and $E^{2\times5}/E^{5\times5}$: Respectively, the ratio between the energy of the super-cluster seed and the total energy collected in the 5×5 matrix surrounding the seed, and the ratio between the sum of the seed energy and the energy of the most energetic crystal adjacent to the seed and the total energy collected in the 5×5 matrix surrounding the seed. The pattern of

energy deposition made by an electron is fairly well understood from simulation and test beam studies. Electron candidates deviating from those energy patterns are likely to be jets.

- ECAL Isolation: The transverse electromagnetic energy of all deposits with $E > 0.08$ GeV in the ECAL barrel ($E > 0.1$ GeV in the ECAL endcap) in a ΔR cone of radius 0.3 centered on the position of the electron in the calorimeter, excluding those in an inner cone of radius 3 crystals and η strip of total width of 3 crystals. Due to deficiencies in the design of the reconstruction software, it is not possible to simply count crystals. Instead, we must work out what the crystal width approximately corresponds to in η to convert the crystal cut into an η cut. This is 0.0174 in the barrel and $0.00864 \times |\sinh(\eta)|$ in the endcap. This variable is used only in a sum with the hadronic depth 1 isolation, defined below. Significant nearby ECAL energy deposits not associated with the electron candidate often indicate the presence of a jet.

- Hadronic Depth Isolation: The transverse depth of hadronic energy of all the HCAL energy deposits in a ΔR cone of radius 0.3 centered on the position of the electron in the calorimeter, excluding energy deposits in a ΔR cone of radius 0.15. Different depths are defined for the barrel towers 1-17 (no depth segmentation), the forward towers 18-29, and the very forward towers 27-29. Exploiting the segmented depth in the forward towers gives better performance at high E_{T}^{ele}. Significant nearby HCAL energy deposits not associated with the electron candidate often indicate the presence of a jet.

- Track p_{T} Isolation: The sum p_{T} of the tracks in a ΔR cone of 0.04–0.3 with $p_{\mathrm{T}} > 0.7$ GeV and z-position within $\pm$ 0.2 of the z-position of the track of the

electrons. The z-position is the minimum distance along the z-axis from the nominal beam spot. A large number of high-p_{T} tracks not associated with the electron candidate often indicate the presence of a jet.

Electron candidates that pass all of the quality selections are hereafter called electrons.

6.1.3 Single-Electron Trigger

To be as inclusive as possible, the goal is to use a single-electron trigger to select events. However, during the 2010 data-taking period, the instantaneous luminosity increased by over 5 orders of magnitude from 10^{27} cm^{-2}s^{-1} to 2×10^{32} cm^{-2}s^{-1}. Due to the rapidly evolving beam conditions, it was not possible to use one unchanging trigger. Instead, it was necessary to use a collection of several electron triggers with different energy thresholds and quality requirements. A summary of the HLT trigger path used for the different run periods is given in Tab. 6.2.

The requirements for the HLT, in terms of variables defined above, are:

- Inclusive Electron/Photon paths: H/E < 0.15;
- CaloEleId: H/E < 0.15, $\sigma_{i\eta i\eta}$ < 0.014 (EB) or 0.035 (EE);
- EleId: CaloEleId plus $\Delta\eta$ < 0.01, $\Delta\phi$ < 0.08 (requires an online track);
- TightCaloEleId: H/E < 0.1, $\sigma_{i\eta i\eta}$ < 0.012 (EB) or 0.032 (EE);
- TightCaloEleIdTrack: H/E < 0.1, $\sigma_{i\eta i\eta}$ < 0.012 (EB) or 0.032 (EE) (requires online track).

Table 6.2: List of the trigger paths used in this analysis. The right column indicates how much data was collected with each trigger.

HLT path	$\mathcal{L}(\text{pb}^{-1})$
HLT_Ele10_LW_L1R	0.1
HLT_Ele15_SW_L1R	0.2
HLT_Ele15_SW_CaloEleId_L1R	2.8
HLT_Ele17_SW_CaloEleId_L1R	5.1
HLT_Ele27_SW_TightCaloEleIdTrack_L1R_v1	9.5
HLT_Ele22_SW_TighterEleId_L1R_v2	10.3
HLT_Ele22_SW_TighterEleId_L1R_v3	8.1

6.1.4 Energy Scale

For both the electron energy scale corrections and the electron efficiency measurements (described in the next section), we use $Z \to e^+e^-$ events. These events are useful for our studies, because they provide a relatively pure sample of leptons when requiring that the invariant mass of the leptons be close to the mass of the Z boson. The decay of Z bosons to electrons is well understood both theoretically and from other experiments.

In general, the energy resolution in the Monte Carlo simulations does not accurately reproduce the energy resolution in data. In addition, the corrections to the electron energy and their effects differ slightly between Monte Carlo and data. In this analysis, we correct for these differences between simulation and data due to the electron energy resolution and the electron energy scale. First, we look at data and simulation events with two electrons that both travel

through the ECAL barrel ($|\eta| < 1.45$). Then, we select events with Z bosons by requiring that the event have electrons of opposite charge, that both electrons pass the identification requirements listed above (one with $E_T > 30$ GeV and the second with $E_T > 10$ GeV), and that the reconstructed invariant mass of the two electrons be between 60 and 120 GeV (recall that the mass of the Z boson is about 91 GeV).

Next, we concentrate on the Monte Carlo simulation. For the two electrons in the ECAL barrel, we scale the energy of each electron, and we also smear their energy. The energy scale factor (multiplicative factor for the energy) varied between 0.950 and 1.050 in steps of 0.001. The smearing of the energy is accomplished by adding to the electron energy between 0.00 and 1.50 GeV in steps of 0.01 GeV, multiplied by a random number from a Gaussian distribution with mean 0 and sigma 1. For each scale factor and smearing, we construct an invariant mass of the two electrons. We compare this distribution to the invariant mass distribution from data and calculate the χ^2. The scale factor and smearing of the simulation that produced the smallest final χ^2 value is taken as the optimal values for electrons in the barrel.

Once we have the corrections for the barrel, we repeat the procedure for events with one electron in the barrel (which we knew how to correct) and one electron in the endcap. This gives us the correction for electrons in the endcap. Finally, we look at events with both electrons in the endcap after applying our corrections. Figure 6.4 shows the data compared with the simulation both before and after correcting the Monte Carlo. We see that the agreement improves significantly after applying the corrections. We find that we need to scale up the energy of the electrons in the data by 0.8% in the ECAL barrel and by 4.2% in the

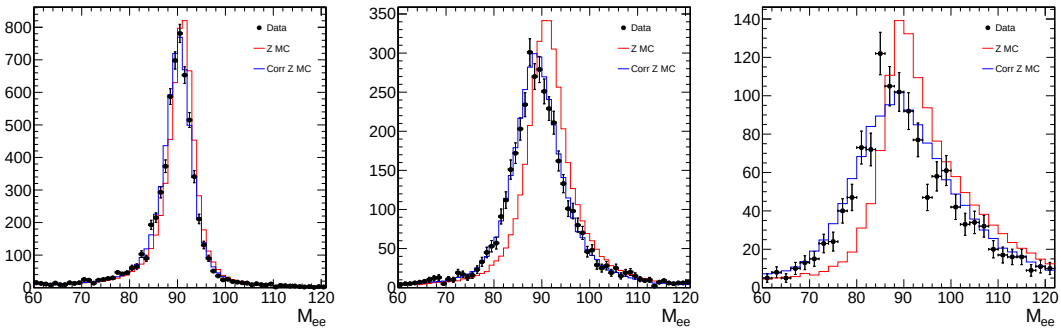

Figure 6.4: Distributions of the invariant mass of two electrons in data (black points), MC (red line), and MC that has a smear and scale factor that best matches the data (blue line). One electron must pass the full identification requirements, and the second electron must also pass the identification with $E_T > 10$ GeV. Electrons must have opposite charge. Left: Both electrons in the ECAL barrel. Center: One electron in the ECAL barrel and one in the endcap. Right: Both electrons in the ECAL endcap.

ECAL endcap. Also, we apply a smearing of 0.41 GeV for Monte Carlo electrons in the ECAL barrel and 1.00 GeV for Monte Carlo electrons in the ECAL endcap to get the simulation to more accurately reproduce the data.

6.1.5 Efficiency

When comparing the data and simulation, it is important to take into account any differences in electron reconstruction and identification efficiency. Differences in efficiency are important for two reasons. First, efficiency measurements are an important tool to check that both the detector and the reconstruction software are performing well. Second, to get an accurate estimate of background sources from the Monte Carlo simulation, the simulation should have the same electron efficiency as the data. We need to correct for any differences between

the two.

The efficiency of electrons to begin as super-clusters and end up passing our electron identification can be factored into three separate efficiencies: the reconstruction efficiency for an electron to be reconstructed at all (ϵ_{reco}), an identification efficiency for electrons to pass the quality criteria described above (ϵ_{id}), and an HLT efficiency for electrons to pass the single-electron trigger requirement given above (ϵ_{trig}). We can write this factorization as

$$\epsilon_{\text{total}} = \epsilon_{\text{reco}} \cdot \epsilon_{\text{id}} \cdot \epsilon_{\text{trig}}. \tag{6.2}$$

Once the total electron efficiency for both data (ϵ_{data}) and Monte Carlo simulation (ϵ_{sim}) are computed, the ratio of efficiencies

$$\rho_{\text{eff}} = \frac{\epsilon_{\text{data}}}{\epsilon_{\text{sim}}} \tag{6.3}$$

can be used as a correction factor on the predicted background yields obtained using Monte Carlo samples.

The electron efficiency at each step is measured using the tag-and-probe method. This method has been studied at the Tevatron by the CDF and D0 collaborations [61] and by CMS [62]. As with the energy scale corrections, we begin by selecting a clean sample of $Z \to e^+e^-$ events comprised of both a "tag" and a "probe" electron candidate. The tag must pass a tight electron selection, while the probe is only required to pass a much looser selection criteria.

For each efficiency measurement, the invariant mass of the tag and the probe is required to be between 70 and 110 GeV, and the tag is always an electron that passes the full identification given above. The probe is required to pass the specific criteria that is used to define the particular efficiency that is under study.

For the reconstruction efficiency measurement, the probe is a super-cluster in the ECAL acceptance (passing the E_{T}, H/E, and $\sigma_{i\eta i\eta}$ requirements of the electron identification), and the probe passes the selection if it is matched ($\Delta R < 0.3$) to a GSF electron. For the identification efficiency measurement, the probe is a GSF electron (again passing E_{T}, H/E, and $\sigma_{i\eta i\eta}$ requirements), and the probe passes if it satisfies the full electron identification. Finally, for the trigger efficiency, the probe is an electron passing the full electron identification, and the probe passes if it fires the trigger (i.e., if it is within $\Delta R < 0.3$ of the HLT object corresponding to the trigger of interest).

From the tag and probe definitions, we can construct the invariant mass of the tag and probe pairs separately for when the probe passes and when the probe fails a given selection. Although $Z \to e^+e^-$ events present a fairly clean signature, some background events will fall within the invariant mass window that we are using. Therefore, we fit the invariant mass distribution to the sum of a signal and a background distribution. For the $Z \to e^+e^-$ signal distribution, we use a Breit-Wigner distribution [63] (to describe the natural shape and width of the Z boson decay) convoluted with a Crystal Ball distribution [64] (to account for the finite detector resolution and radiation effects). For the background distribution, we use a polynomial. From the fit to the sum of signal and background components, we can determine the number of probes that pass or fail a given selection, which is used to determine the efficiency of that selection using

$$\epsilon = \frac{N_{\mathrm{probe}}^{\mathrm{pass}}}{N_{\mathrm{probe}}^{\mathrm{pass}} + N_{\mathrm{probe}}^{\mathrm{fail}}} \tag{6.4}$$

where the uncertainty on the number of probes passing or failing the selection (mostly due to statistics) is propagated to an uncertainty on the efficiency mea-

Table 6.3: Electron efficiency measurements for data, simulation, and the ratio of the two (data/simulation).

Efficiency	ϵ_{data}	ϵ_{sim}	ρ_{eff}
EB			
ϵ_{reco}	0.979 ± 0.002	0.976 ± 0.002	1.003 ± 0.003
ϵ_{id}	0.843 ± 0.005	0.868 ± 0.005	0.970 ± 0.008
ϵ_{trig}	0.977 ± 0.002	1.000 ± 0.000	0.977 ± 0.002
ϵ_{total}	0.806 ± 0.005	0.848 ± 0.005	0.951 ± 0.008
EE			
ϵ_{reco}	0.934 ± 0.006	0.948 ± 0.006	0.986 ± 0.009
ϵ_{id}	0.842 ± 0.009	0.837 ± 0.010	1.006 ± 0.016
ϵ_{trig}	0.963 ± 0.005	1.000 ± 0.000	0.963 ± 0.005
ϵ_{total}	0.758 ± 0.010	0.793 ± 0.010	0.955 ± 0.018

surement.

Figure 6.5 shows the invariant mass distributions of tag and probe pairs and the fit results for the different selections and ECAL regions (barrel and endcap). Table 6.3 gives the results of the efficiency measurements for each selection and the total efficiency in both the EB and EE. In addition, the table gives the efficiency for both the data and the Monte Carlo simulation, and it gives the ratio of the efficiencies, ρ_{eff}, used to correct the Monte Carlo simulation. Note that not all triggers of interest are simulated in the Monte Carlo samples, due to the constantly changing trigger requirements. Therefore, we did not implement a trigger requirement on simulated events. Instead, we weight each simulated event (in terms of counting events) by the trigger efficiency we find in the data.

The inefficiency in the single electron trigger is mostly due to the HLT online track-matching requirement, which was not fully efficient during the 2010 data-taking period.

6.2 Missing Transverse Energy

As described above, we are interested in events with large missing transverse energy ($\not\!\!E_{\mathrm{T}}$ or MET). Currently, there are three algorithms that are used by the CMS experiment to measure this important quantity: calorimeter based $\not\!\!E_{\mathrm{T}}$ (caloMET), track-corrected calorimeter $\not\!\!E_{\mathrm{T}}$ (tcMET), and particle-flow $\not\!\!E_{\mathrm{T}}$ (pfMET). Since $\not\!\!E_{\mathrm{T}}$ is such a critical variable for our analysis, and because there is so much information that is included to calculate the $\not\!\!E_{\mathrm{T}}$ for each event, it is important to understand any issues with the different $\not\!\!E_{\mathrm{T}}$ algorithms. The algorithms have different levels of sophistication and complication, allowing them to be good cross-checks of one another.

CaloMET is the negative vector sum of the transverse energy deposited in calorimeter towers that are above a certain noise threshold [10]. It is corrected to account for clustered energy and muon deposits in the calorimeter. Muons will deposit a small fraction of their energy (a few GeV) in the calorimeters. The muon correction removes the muon p_{T} and adds back the energy deposition. In order to incorporate the nonlinear and non-compensating behavior of the calorimeter, the jet energy corrections are propagated to caloMET. Finally, there are corrections to correct all unclustered towers for this nonlinearity.

The goal of tcMET is to augment caloMET in places where the tracker measurement is more accurate than the calorimeter measurement. The track-

corrected $\not\!\!E_T$ algorithm starts from caloMET. From there, tracking information is incorporated by adding the p_T of the reconstructed tracks and subtracting the expected calorimetric energy deposited by that track [65]. For this, tracks are all treated as pions, and the expected energy deposit is determined from simulation. Tracks with $p_T < 2$ GeV (that do not deposit energy in the calorimeters) or $p_T > 100$ GeV (that are well measured by the electromagnetic calorimeter) are not included in this correction.

The particle-flow technique aims to reconstruct a complete, unique list of particles in each event using the entire CMS detector [66]: muons, electrons, photons, and charged and neutral hadrons. The pfMET is the negative vector sum of the transverse momentum of all reconstructed particles in the event. Corrections to propagate particle-flow jet energy corrections to pfMET are under development, but they were not used for this analysis.

In order to compare the algorithms for our selection, we investigated the $\not\!\!E_T$ distributions and the differences between algorithms in events with undetectable particles and genuine $\not\!\!E_T$ (e.g., $W \to e\nu$). Figure 6.6 shows the $\not\!\!E_T$ distributions for the three different algorithms. Notice that the three $\not\!\!E_T$ algorithms have a qualitatively similar behavior for large values of missing transverse energy, but they display different behavior for small values of missing transverse energy. One can see that the Monte Carlo simulation predicts that calorimeter $\not\!\!E_T$ has a much larger contribution from the multi-jet and γ+jets background than the other $\not\!\!E_T$ algorithms. Figure 6.7 shows the differences between the three $\not\!\!E_T$ algorithms for two different selections: requiring events have one electron (passing events are dominated by multi-jet background), and requiring events that have one electron and pass the requirement $0.4 < E_T^{ele} / \not\!\!E_T < 1.5$ (a selection

that is dominated by $W \to e\nu$ events).

On average, calorimeter $\not\!\!E_{\mathrm{T}}$ is larger than either track-corrected or particle-flow $\not\!\!E_{\mathrm{T}}$ in a selection dominated by multi-jet events. One may also observe that the three $\not\!\!E_{\mathrm{T}}$ algorithms are not as different as one might expect in a selection dominated by W boson events. For example, the distribution of pfMET-tcMET is well described by a Gaussian distribution with a mean of 1.1 GeV and a sigma of 3.7 GeV. In addition, there are only a handful events where the difference between the two algorithms is greater than 20 GeV. Figure 6.8 shows a comparison of pfMET, tcMET, and the difference between the two as a function of E_{T}^{ele} or $\not\!\!E_{\mathrm{T}}$. The largest differences between the two algorithms occur for low values of $\not\!\!E_{\mathrm{T}}$. For $\not\!\!E_{\mathrm{T}} > 100$ GeV, both algorithms give similar estimates for the missing transverse energy in the event. This gives us some confidence that our estimate for $\not\!\!E_{\mathrm{T}}$ is fairly accurate.

The CMS collaboration has studied the performance of these different types of $\not\!\!E_{\mathrm{T}}$ in events containing electroweak bosons [67]. Good agreement has been observed between data and Monte Carlo simulation for each of the three $\not\!\!E_{\mathrm{T}}$ algorithms. However, it was noted that the inclusion of charged-particle tracking (e.g., for pfMET and tcMET) significantly improved the $\not\!\!E_{\mathrm{T}}$ resolution, including in events with genuine $\not\!\!E_{\mathrm{T}}$ (as is the case for $W \to e\nu$ events). In order to use the $\not\!\!E_{\mathrm{T}}$ with the best resolution, we choose to use particle-flow $\not\!\!E_{\mathrm{T}}$ for this analysis. Figure 6.9 shows the resolution of the different MET algorithms.

6.3 Transverse Mass

The transverse mass is an attempt to reconstruct the parent particle in the decay $W' \rightarrow e\nu$ using only transverse quantities. Although not a physics object, the reconstruction of the transverse mass is critical for this analysis. Constructed from the missing transverse energy and the electron, it provides a better discriminator between $W' \rightarrow e\nu$ events and background events than the electron or $\not{E}_{\mathrm{T}}$ alone. It is necessary that the mass must be the transverse mass, as the longitudinal component of the neutrino momentum is unknown.

Reconstruction of the transverse mass for the W' boson is exactly the same as the reconstruction of the standard model W boson, as both bosons will produce a Jacobian peak when looking at the transverse mass distribution. The transverse mass is calculated as

$$m_{\mathrm{T}} = \sqrt{2 \cdot E_{\mathrm{T}}^{ele} \cdot \not{E}_{\mathrm{T}} \cdot \left(1 - \cos \Delta\phi_{e\not{E}_{\mathrm{T}}}\right)} \tag{6.5}$$

where E_{T}^{ele} is the transverse energy of the electron, $\not{E}_{\mathrm{T}}$ is the estimation of the transverse momentum of the neutrino, and $\Delta\phi_{e\not{E}_{\mathrm{T}}}$ is the opening azimuthal angle between the electron and the neutrino. The transverse mass distribution will have an edge at the mass of the W' boson.

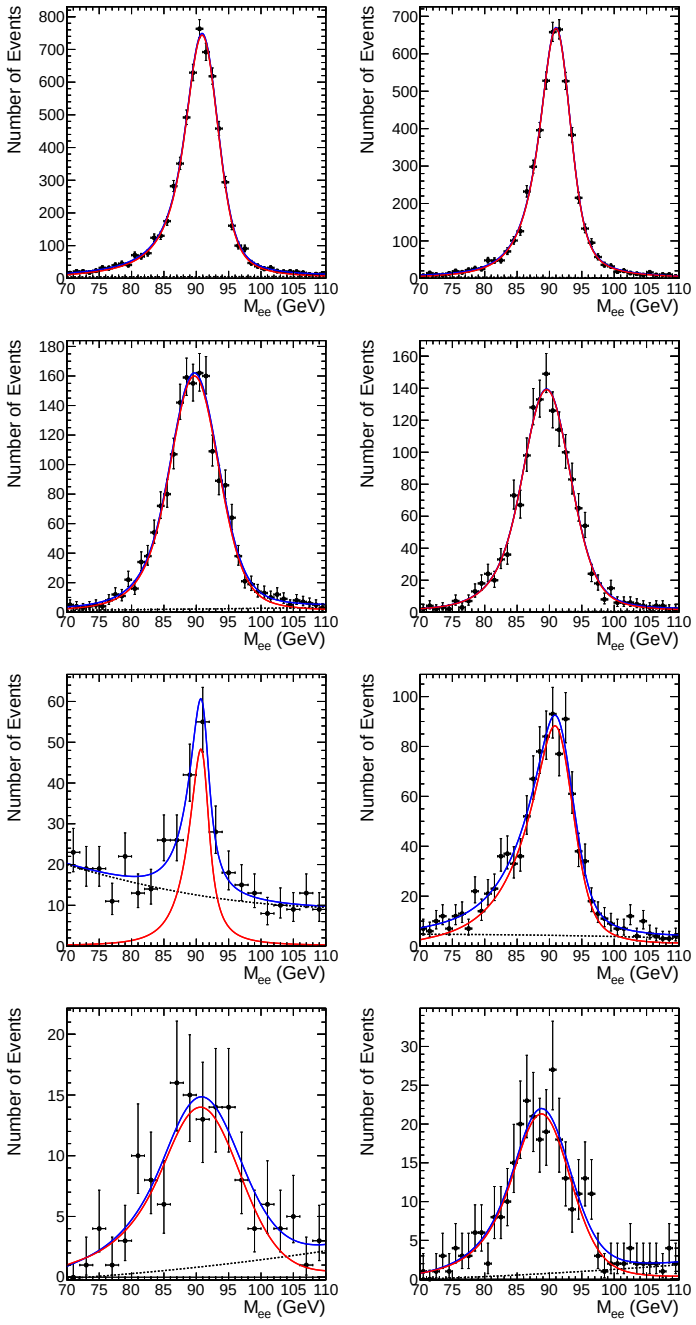

Figure 6.5: Invariant mass distributions of tag and probe pairs where the probe passes (top two rows) and fails (bottom two rows) a given selection. The first (second) column is for the measurement of the reconstruction (identification) efficiency. The first and third rows are for probe candidates in the ECAL barrel, while the second and fourth rows are probe candidates in the ECAL endcap. The fits for the background (dotted blue), Z signal (solid red), and sum (solid blue) are shown.

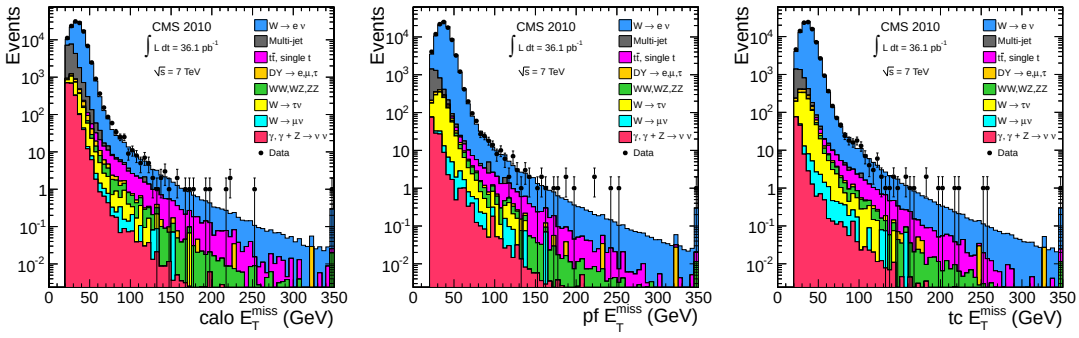

Figure 6.6: Distributions of the three $\not\!\!E_{\mathrm{T}}$ algorithms for data and Monte Carlo after requiring that each event have one identified electron, $\not\!\!E_{\mathrm{T}} > 20$ GeV, and $0.4 < E_{\mathrm{T}}^{ele}/\not\!\!E_{\mathrm{T}} < 1.5$. Left: Calorimeter $\not\!\!E_{\mathrm{T}}$. Center: Particle-flow $\not\!\!E_{\mathrm{T}}$. Right: Track-corrected $\not\!\!E_{\mathrm{T}}$.

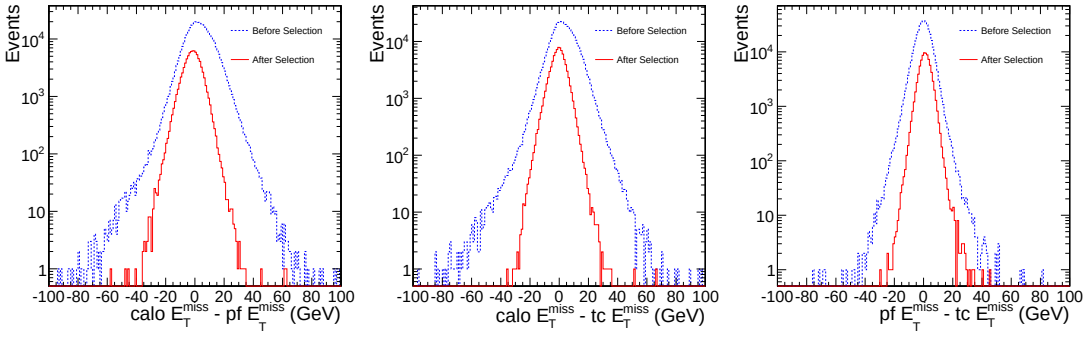

Figure 6.7: Distributions of differences between $\not\!\!E_{\mathrm{T}}$ algorithms in data for events with one electron. Distributions are shown before (dashed line) and after (solid line) requiring $0.4 < E_{\mathrm{T}}^{ele}/\not\!\!E_{\mathrm{T}} < 1.5$. Left: Calorimeter $\not\!\!E_{\mathrm{T}}$- Particle-flow $\not\!\!E_{\mathrm{T}}$. Center: Calorimeter $\not\!\!E_{\mathrm{T}}$- Track-corrected $\not\!\!E_{\mathrm{T}}$. Right: Particle-flow $\not\!\!E_{\mathrm{T}}$- Track-corrected $\not\!\!E_{\mathrm{T}}$.

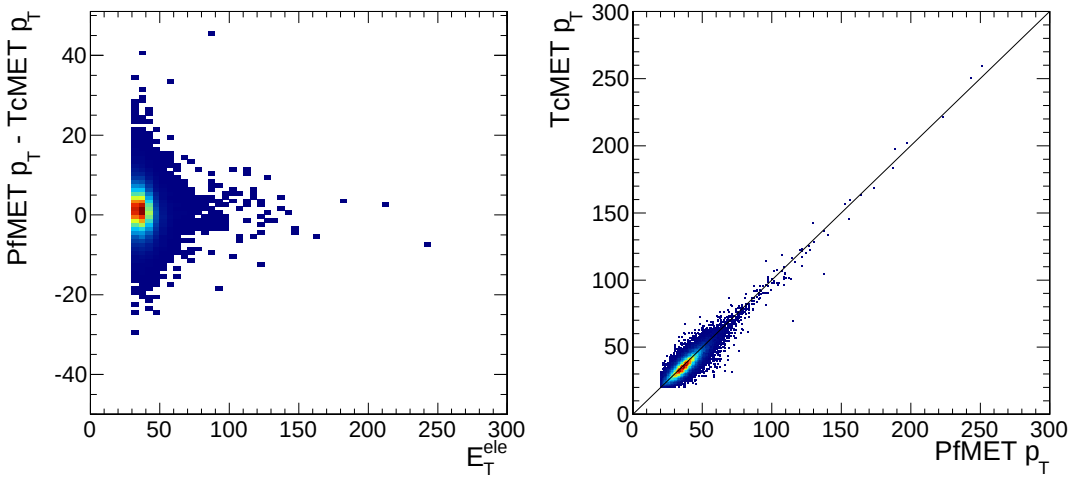

Figure 6.8: Comparison of the tc and pf $\not\!\!E_T$ algorithms for our analysis. The bulk of the differences are at small electron E_T and $\not\!\!E_T$. The differences between algorithms decrease rapidly at higher energy scales. Left: Difference between pf and tc $\not\!\!E_T$ as a function of the electron E_T. Right: tc $\not\!\!E_T$ vs pf $\not\!\!E_T$.

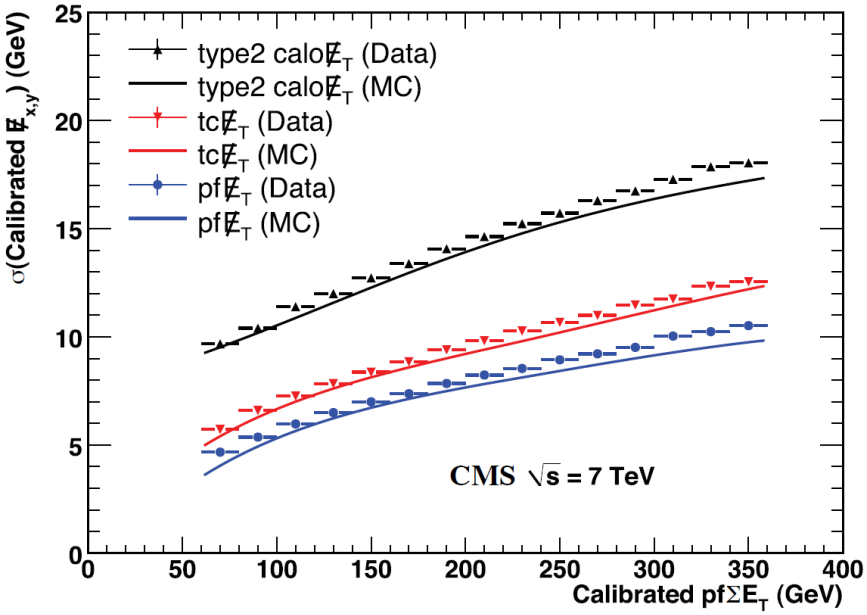

Figure 6.9: Calibrated x- and y-components of $\not\!\!E_T$ versus the total transverse energy in the event for the three $\not\!\!E_T$ algorithms in data and in simulation [10].

CHAPTER 7

ANALYSIS PROCEDURE AND METHODS

The signal selection has been optimized with Monte Carlo simulated samples. This section summarizes the selection steps and shows the performance results from comparisons of data and Monte Carlo.

7.1 Event Selection

The goal of the event selection is to separate signal from background events. The signature of $W' \to e\nu$ events is characterized by the presence of one high p_{T} electron and missing transverse energy ($\not\!\!E_{\mathrm{T}}$) caused by the neutrino that is not detectable with the CMS detector. The charged lepton momentum and the $\not\!\!E_{\mathrm{T}}$ are expected to be balanced in the transverse plane, leading to a signature that is very similar to $W \to e\nu$ events, our largest background.

Given the large mass of the W' compared to the W boson, the electron from its decay has a large momentum, and the electron identification cuts for high energy electrons (as described in the previous chapter) are optimized to be efficient at selecting signal events and rejecting background events. After requiring at least one electron, most of the W' events survive the selection, while the multijet and $t\bar{t}$ backgrounds are significantly reduced. Due to the similarity of W and W' boson signatures, most $W \to e\nu$ events also survive this selection. One reason that some $W \to e\nu$ events do not pass it is the high value of the electron energy cut ($E_{\mathrm{T}}^{ele} > 30$ GeV); this cuts into the kinematic acceptance of those W boson events, where the peak of the E_{T}^{ele} distribution is around 40 GeV.

To improve the signal to background ratio, events are selected according to

the following set of requirements:

- There is a pre-selection applied to all samples, where we require that each event have a GSF electron with $E_{\mathrm{T}}^{ele} > 20$ GeV and H/E < 0.1. This is done to reduce the initial number of events that need to be processed.
- The event has to satisfy the single-electron unprescaled trigger with the lowest E_{T} threshold, as given in the previous chapter.
- Exactly one electron passing all identification requirements with transverse energy greater than 30 GeV.
- The ratio between the electron transverse energy and the missing transverse energy, $E_{\mathrm{T}}^{ele}/\not{E}_{\mathrm{T}}$, should be around 1.0, given the two-body decay. The selected range is $0.4 < E_{\mathrm{T}}^{ele}/\not{E}_{\mathrm{T}} < 1.5$.
- The angle between the direction of the electron and the $\not{E}_{\mathrm{T}}$, $\Delta\phi_{e\not{E}_{\mathrm{T}}}$, should be close to π, since the electron and the neutrino are expected to be almost back-to-back in the transverse plane for signal events. The requirement is $\Delta\phi_{e\not{E}_{\mathrm{T}}} > 2.5$.

The two dedicated selections on the ratio and the angular difference between the electron transverse energy and the $\not{E}_{\mathrm{T}}$, $E_{\mathrm{T}}^{ele}/\not{E}_{\mathrm{T}}$ and $\Delta\phi_{e\not{E}_{\mathrm{T}}}$, are designed to select events with the W' signal topology, with the lepton and the neutrino expected to nearly balance one another in the transverse plane. As illustrated in Fig. 7.1, the distribution of $E_{\mathrm{T}}^{ele}/\not{E}_{\mathrm{T}}$ shows a pronounced peak around 1.0. Also shown is the $\Delta\phi_{e\not{E}_{\mathrm{T}}}$ distribution, which peaks around π for the signal and for the $W \to e\nu$ background, while it is flatter for the other main backgrounds (namely $t\bar{t}$, multi-jet, and Z boson events). No strong dependence of the signal selection efficiency on the exact value of the selection requirement is observed from studies performed on simulated events.

The efficiencies for each major selection step mentioned above relative to the previous cut and the total efficiency after each cut are detailed in Tab. 7.1 for the signal and Tab. 7.2 for the Monte Carlo backgrounds.

7.2 Data - Monte Carlo Comparisons

This section shows the comparison of data to the simulated Monte Carlo samples for key quantities of this analysis. Here, we use the Monte Carlo samples out-of-the-box. The distributions using more sophisticated data-driven methods for the background estimation are shown below. The distribution of the transverse energy of electrons in the EB and EE are shown in Fig. 7.2. The pseudorapidity, η, and the azimuthal angle, ϕ, are shown in Fig. 7.3. The η-distribution exhibits the gaps in the ECAL barrel-endcap transition (crack) region, which are excluded in this analysis.

The Monte Carlo samples seem to model the data well, as we see good between the two. One place where the agreement is not as good between data and Monte Carlo is in the η distribution for the ECAL endcap. The disagreement in this region is most likely due to an incorrect estimate of the multi-jet background. To get a better estimate, it is necessary to use data-driven methods.

7.3 Background Estimation

This section describes how we obtain a transverse mass distribution for each of the standard model backgrounds. The backgrounds can be separated into three

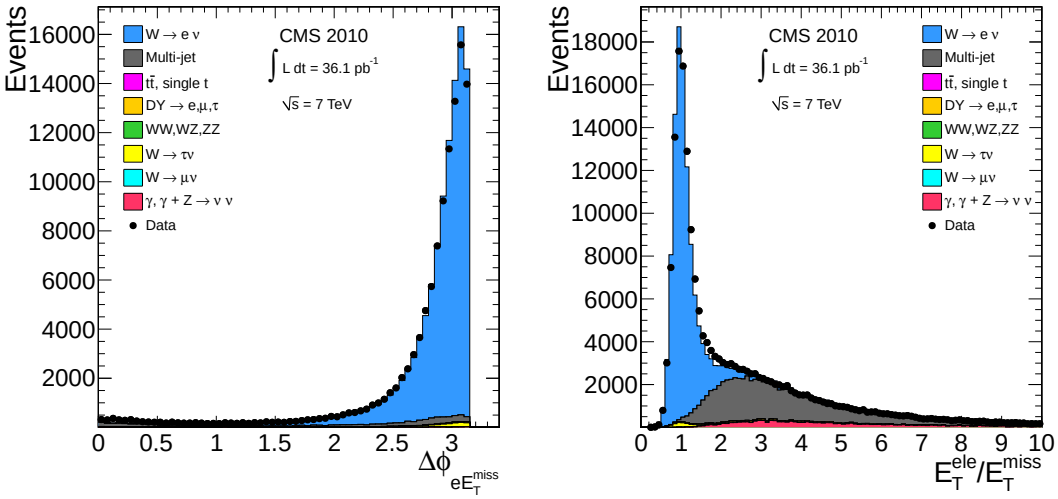

Figure 7.1: Kinematic quantities involving the electron and $\not{E}_{\mathrm{T}}$. Left: The angular difference $\Delta\phi_{e\not{E}_{\mathrm{T}}}$ for signal and backgrounds. Right: The ratio between the electron transverse energy and the missing transverse energy for signal and backgrounds.

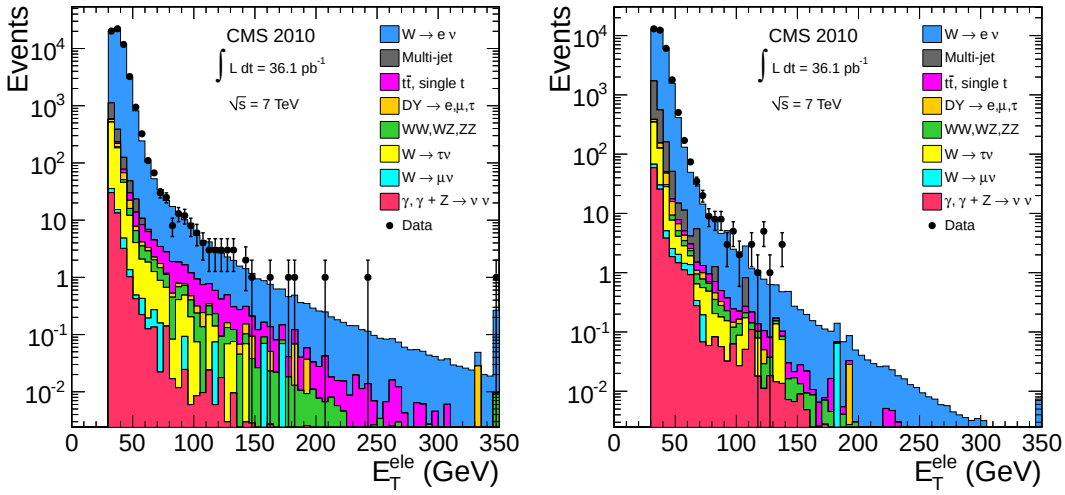

Figure 7.2: Distribution of electron E_{T} for electrons in the ECAL barrel (left) and ECAL endcap (right).

different major components: $W \to e\nu$, multi-jet, and "Other". The "Other" standard model backgrounds are a combination of the following backgrounds: γ +

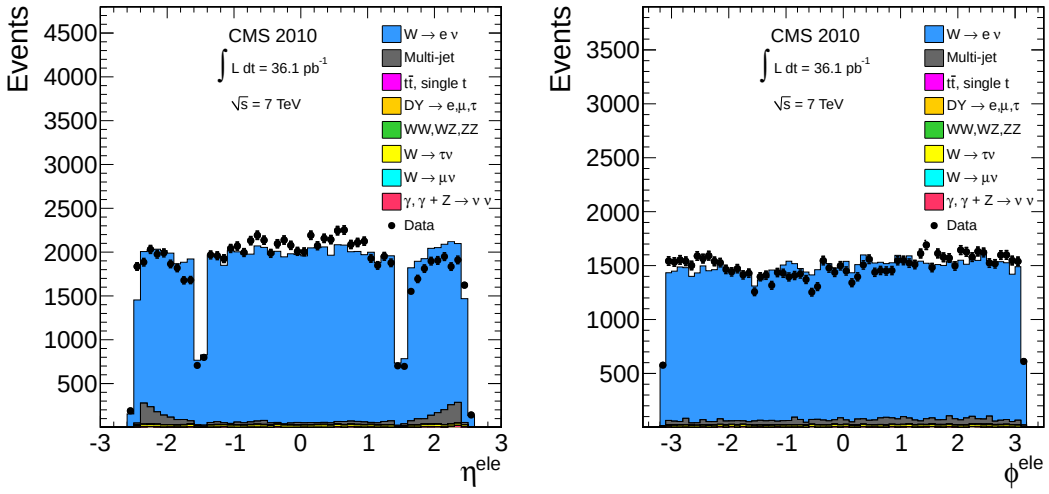

Figure 7.3: Distribution of electron η (left) and ϕ (right).

jets, $W \to \tau\nu$, $W \to \mu\nu$, $Z/\gamma^* \to \ell\ell$, WW, WZ, ZZ, $t\bar{t}$, single t, and $Z + \gamma \to \nu\nu + \gamma$. These background contributions are expected to be very small from Monte Carlo simulations. As such, the transverse mass distributions for these backgrounds are obtained entirely from simulation (shape and normalization), with appropriate corrections (e.g., electron energy resolution and efficiency corrections).

7.3.1 The Hadronic Recoil Method

The largest standard model background for our signal region is $W \to e\nu$. The contribution from this background is obtained from Monte Carlo simulation, but it is corrected to account for differences in the $\not{E}_{\mathrm{T}}$ resolution and response between data and simulation that can arise due to un-modeled detector effects, pile-up, etc. This is called the Hadronic Recoil method, and it has been used by the CMS collaboration to extract the best possible measurement of the W cross

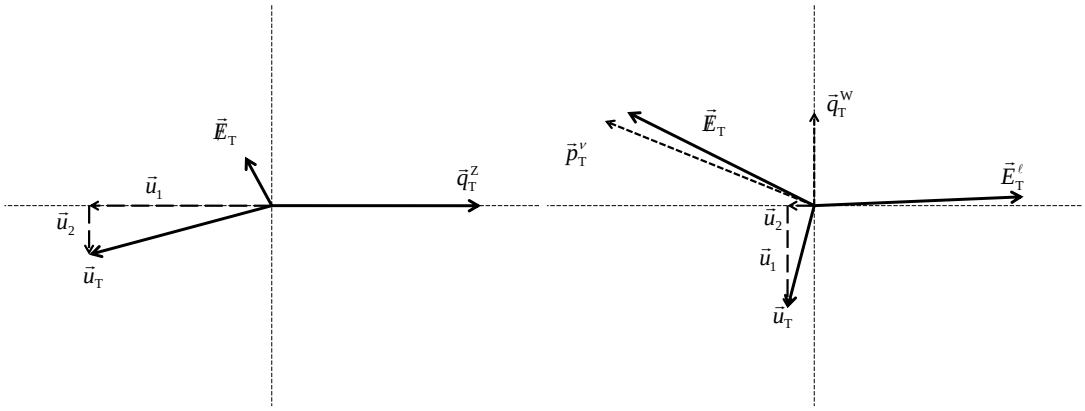

Figure 7.4: Diagrams of hadronic recoil. Left: Z boson events. Right: W boson events.

section [62].

Here, we attempt to exploit similarities between the hadronic recoil of the W and Z bosons. The hadronic recoil is the energy that (roughly) balances the momentum of the gauge bosons. It is due to hard radiation (jets), soft radiation (energy not clustered into jets), and the underlying event (the activity of the spectator particles not involved in the parton collision). For Z boson events, the hadronic recoil vector is defined by the equation

$$\vec{u}_T = -\left(\vec{\not{E}}_T + \vec{q}_T\right) \tag{7.1}$$

where $\vec{u}_T$ is the hadronic recoil vector and $\vec{q}_T$ is the transverse momentum of the Z boson (the sum of the two daughter electrons). It is useful to split up the hadronic recoil vector into components parallel ($\vec{u}_1$) and perpendicular ($\vec{u}_2$) to $\vec{q}_T$. Figure 7.4 provides an illustration of the different vectors of interest for both Z and W boson events.

To select Z boson events in data and simulation, we require that each event have at least two electrons of opposite charge; one electron must pass the full

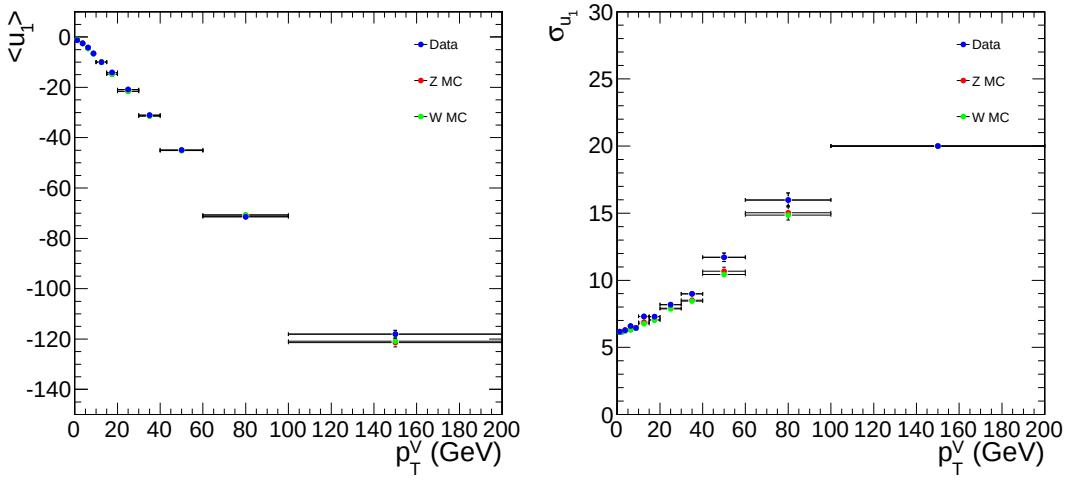

Figure 7.5: As a function of the boson p_{T}, the average (left) and sigma (right) of u_1 for data (blue), Z boson events (red), and W boson events (green).

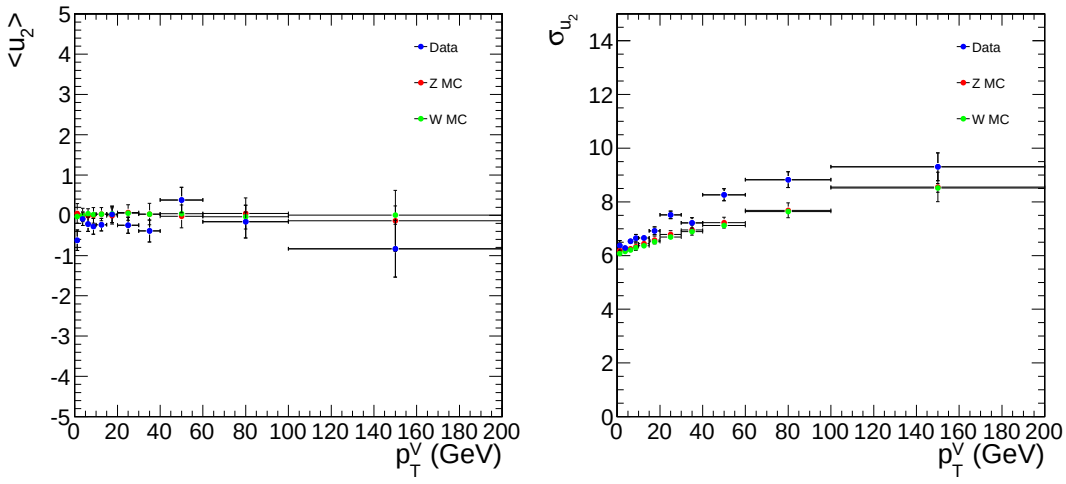

Figure 7.6: As a function of the boson p_{T}, the average (left) and sigma (right) of u_2 for data (blue), Z boson events (red), and W boson events (green).

identification, while the second electron must pass the identification requirements with a lower electron energy threshold ($E_{\mathrm{T}}^{ele} > 10$ GeV). In addition, we require that the invariant mass of the two electrons be between 70 and 110 GeV.

Following the work of the W cross section analysis [62], we use Z boson events to fit both u_1 and u_2 to Gaussian distributions

$$\frac{1}{\sqrt{2\pi\sigma_{u_i}(q_{\mathrm{T}})^2}}\exp\left[-\frac{(u_i - f_{u_i}(q_{\mathrm{T}}))^2}{2\sigma_{u_i}(q_{\mathrm{T}})^2}\right] \tag{7.2}$$

in bins of $q_{\mathrm{T}} \equiv |\vec{q}_{\mathrm{T}}|$, where $f_{u_i}(q_{\mathrm{T}})$ and $\sigma_{u_i}(q_{\mathrm{T}})$ are the mean and sigma of the Gaussian, respectively. Figure 7.5 (7.6) shows the behavior of the mean and sigma of u_1 (u_2) as a function of q_{T} for data, simulated Z boson events, and simulated W boson events. Using $Z \to e^+e^-$ selected events in the data and simulation, we can determine scale factors to correct the $W \to e\nu$ simulation event by event. For example, the sigma of the Gaussian for corrected W bosons is

$$\sigma_{u_i}^{W,\mathrm{corr}}\left(p_T^W\right) = \frac{\sigma_{u_i}^{Z,\mathrm{data}}\left(p_T^W\right)}{\sigma_{u_i}^{Z,\mathrm{MC}}\left(p_T^W\right)} \cdot \sigma_{u_i}^{W,\mathrm{MC}}\left(p_T^W\right). \tag{7.3}$$

Once these Gaussian distributions are found as a function of q_{T}, we can use this to construct a hadronic recoil vector for W boson simulation events (where the boson $\vec{q}_{\mathrm{T}}$ is known) and obtain a corrected value of $\not{E}_{\mathrm{T}}$ on an event-by-event basis using

$$\vec{\not{E}}_{\mathrm{T}} = -\left(\vec{u}_{\mathrm{T}} + \vec{E}_{\mathrm{T}}^{ele}\right). \tag{7.4}$$

Once we have the corrected $\not{E}_{\mathrm{T}}$ for each event, we can use this to construct a corrected transverse mass distribution. This is our prediction for the shape of the W boson m_{T} distribution. Figure 7.7 shows the difference between using the W simulation out-of-the-box and using the hadronic recoil correction. Although the differences are small, they are mostly in the region between 100 and 150 GeV. The tail of the m_{T} distribution is mostly unchanged by the hadronic recoil correction.

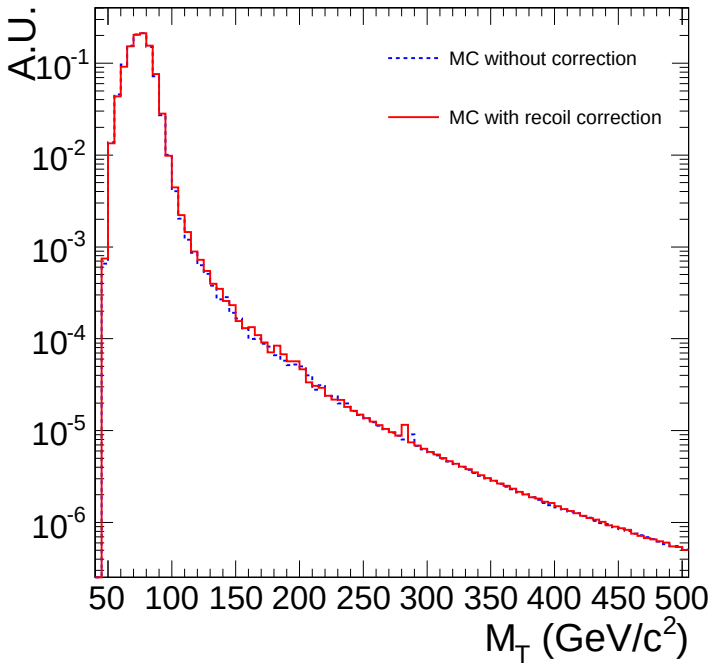

Figure 7.7: Transverse mass distribution for W boson Monte Carlo out-of-the-box (dashed line) and with the hadronic recoil corrections (solid line).

7.3.2 Shape of Multi-Jet Background

The contribution of the multi-jet background to our signal region is due to fake (e.g., a jet that is reconstructed as an electron) or non-prompt (e.g., a bottom quark decay) electrons. These processes are notoriously difficult to simulate correctly, as it requires a good model of the hard scattering process, beam-beam remnants (the spectators in the collision), multiple parton interactions, and the interactions of the quarks and gluons with the detector material as they travel through the different layers of CMS. Therefore, we use a data-driven approach to obtain both the shape and normalization of the multi-jet transverse mass distribution. The shape of the m_T distribution for this background is constructed using non-isolated electrons; such a sample is enriched in multi-jet events. We

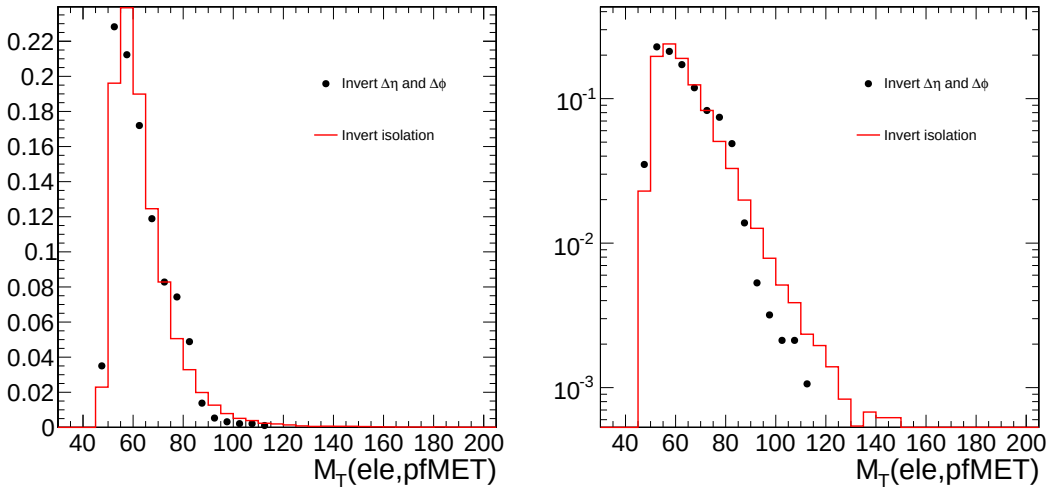

Figure 7.8: Comparison of transverse mass shapes for the multi-jet background obtained by inverting isolation (red line) and by inverting $\Delta\eta$ and $\Delta\phi$ matching between electron track and supercluster (black points). Shapes show fair agreement. Left: Linear y-scale. Right: Logarithmic y-scale.

construct a transverse mass distribution using electron candidates in data that pass the kinematic and identification requirements of the electron selection but fail the isolation requirement. The resultant distribution is our prediction for the shape of the multi-jet m_{T} distribution.

As a check of this shape, we compare the multi-jet transverse mass shape for two orthogonal samples from data: one has the electron isolation requirement but has the $\Delta\eta$ and $\Delta\phi$ requirements inverted, and the other has the electron $\Delta\eta$ and $\Delta\phi$ requirements but has the isolation requirement inverted. Figure 7.8 shows these two templates, and we see that the two agree fairly well. Table 7.3 shows the agreement between the total multi-jet background predictions for the two different shapes for several transverse mass ranges.

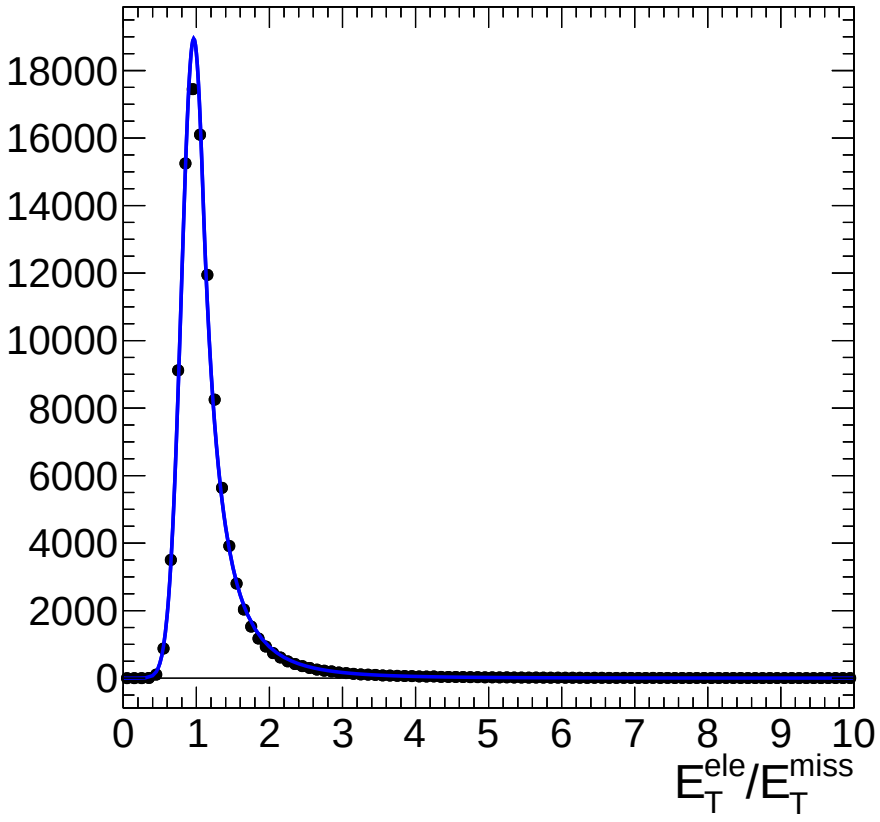

Figure 7.9: W boson Monte Carlo with hadronic recoil correction (black dots) is well modeled by the Crystal Ball function (solid blue line).

7.3.3 Normalization of W boson and Multi-Jet Backgrounds

Once we have the shapes of the W and multi-jet background distributions, we need to determine their normalizations. This is done by exploiting the power of our $E_{\mathrm{T}}^{ele}/\not{E}_{\mathrm{T}}$ cut, the last step in our selection. Again, as one can see from Fig. 7.1, the W background dominates for $E_{\mathrm{T}}^{ele}/\not{E}_{\mathrm{T}}$ around 1.0, and the multi-jet background dominates for $E_{\mathrm{T}}^{ele}/\not{E}_{\mathrm{T}} > 2.0$. To extract the W boson and multi-jet yields, we first subtract the backgrounds that are determined entirely from simulation (labeled "Other" above).

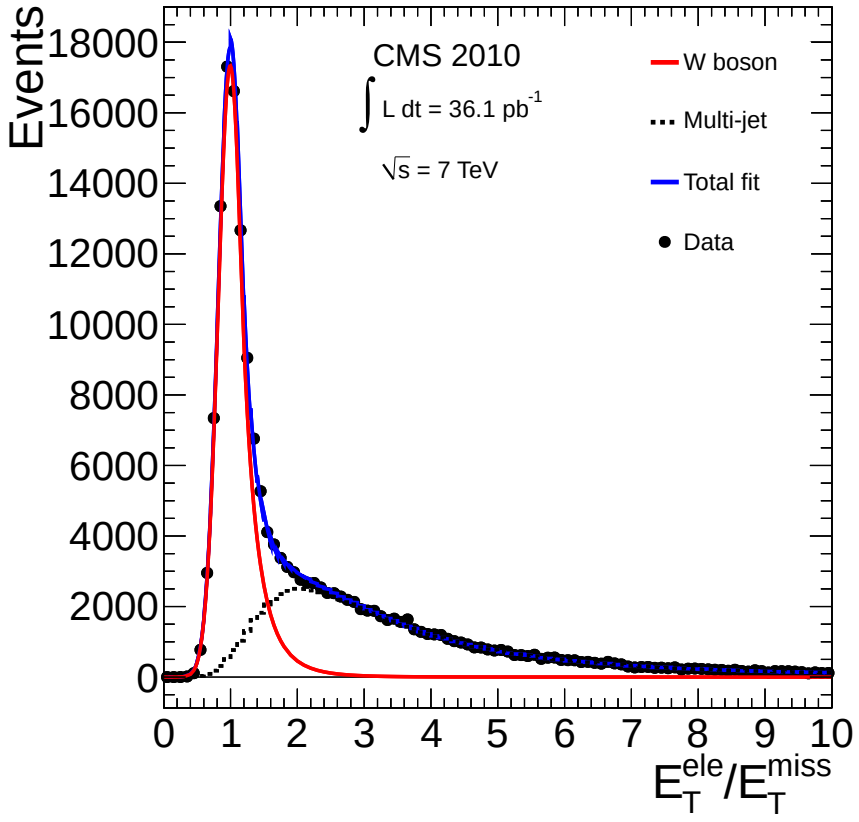

Figure 7.10: Simultaneous fit of W boson and multi-jet templates to data. The fit describes the data well.

The $E_{\mathrm{T}}^{ele}/\not{E}_{\mathrm{T}}$ distribution for W boson events is obtained from simulation that has had the hadronic recoil correction applied, as described above. This distribution is then fit to a Crystal Ball function, as shown in Fig. 7.9 (right). The $E_{\mathrm{T}}^{ele}/\not{E}_{\mathrm{T}}$ distribution for multi-jet events is obtained from electron candidates that have an inverted isolation requirement (only keeping non-isolated electrons). As before, this sample should be enriched in multi-jet events due to the large cross section of these processes.

Figure 7.10 shows the simultaneous fit of the W boson and multi-jet templates to data. We see that the resultant fit describes the data very well. Once we have the distributions for the W boson and multi-jet distributions, we can

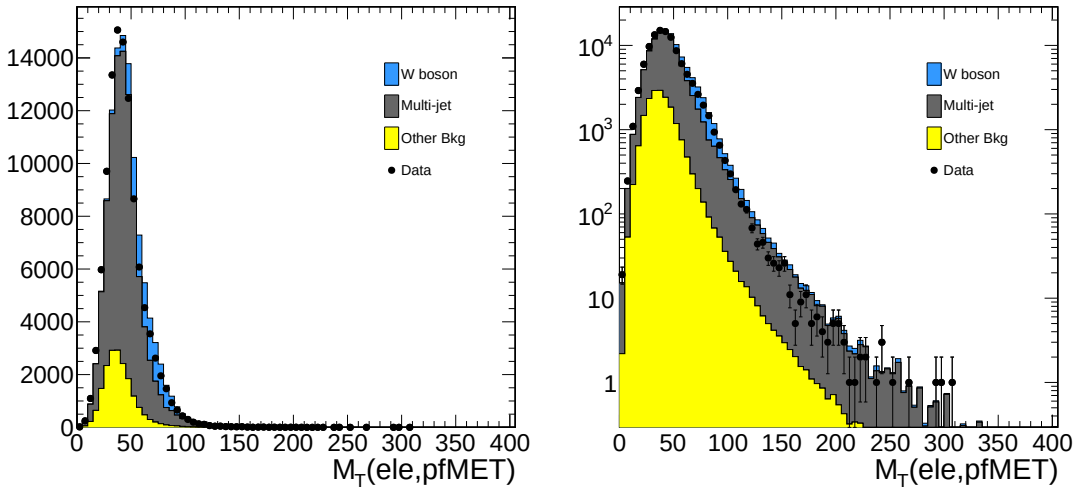

Figure 7.11: Transverse mass distribution for events that fail our $E_{\mathrm{T}}^{ele}/\not{E}_{\mathrm{T}}$ requirement using data-driven methods. As expected, we are dominated by multi-jet events. Although the agreement is not perfect, the shape and normalization are reasonable and well within our 50% uncertainty on the multi-jet background. Left: Linear y-scale. Right: Logarithmic y-scale.

integrate these distributions over the signal region ($0.4 < E_{\mathrm{T}}^{ele}/\not{E}_{\mathrm{T}} < 1.5$) to determine the normalizations for these backgrounds.

As an additional check of the method, we test to see if our data-driven techniques could adequately predict events failing the $E_{\mathrm{T}}^{ele}/\not{E}_{\mathrm{T}}$ requirement, a selection dominated by multi-jet events. Indeed, the method predicts this distribution fairly well (in shape and normalization) within systematic uncertainty, as shown in Fig. 7.11.

Table 7.1: Cutflow for each of our signal samples. The first number is the efficiency of that cut with respect to the previous cut, and the second number is the total efficiency after that cut has been applied with respect to the total number of signal events expected in 36.1 pb^{-1} (shown below last column).

$m_{W'}$ (TeV)	Pre-selection	1 Good Ele	$\Delta\phi_{e\not{E}_T} > 2.5$	$0.4 < E_T^{ele}/\not{E}_T < 1.5$
0.6	- , 89%	94%,83%	92%,76%	97%,74%
				220.05
0.7	- , 88%	93%,83%	92%,76%	97%,74%
				113.57
0.8	- , 90%	93%,83%	92%,76%	97%,74%
				65.13
0.9	- , 90%	93%,84%	93%,78%	98%,76%
				38.25
1.0	- , 90%	93%,84%	93%,78%	98%,76%
				23.09
1.1	- , 90%	94%,84%	93%,78%	98%,77%
				14.28
1.2	- , 91%	93%,85%	93%,79%	98%,78%
				9.40
1.3	- , 90%	93%,84%	93%,79%	98%,77%
				6.01
1.4	- , 90%	93%,84%	93%,78%	98%,77%
				3.77
1.5	- , 90%	94%,84%	93%,79%	98%,78%
				2.76
2.0	- , 89%	93%,82%	93%,77%	98%,75%
				0.39

Table 7.2: Cutflow for each of our Monte Carlo background samples. The first number is the efficiency of that cut with respect to the previous cut, and the second number is the total efficiency after that cut has been applied with respect to the total number of background events expected in 36.1 pb^{-1} (shown below last column).

Sample	Pre-selection	1 Good Ele	$\Delta\phi_{e\not{E}_{\mathrm{T}}} > 2.5$	$0.4 < E_{\mathrm{T}}^{ele}/\not{E}_{\mathrm{T}} < 1.5$
$W \to e\nu$	- , 48%	73%,35%	81%,28%	87%,24%
				91679.29
Multi-jet	- , $7 \cdot 10^{-4}$%	2.5%,$2 \cdot 10^{-5}$%	34%,$6 \cdot 10^{-6}$%	3.5%,$2 \cdot 10^{-7}$%
				2830.24
$t\bar{t}$, single t	- , 32%	46%,15%	19%,2.8%	54%,1.5%
				88.19
$DY \to e, \mu, \tau$	- , 15%	46%,7.0%	30%,2.1%	5.2%,0.1%
				196.56
WW, WZ, ZZ	- , 15%	56%,8.6%	39%,3.4%	60%,2.0%
				48.90
$W \to \tau\nu$	- , 2.3%	30%,0.7%	57%,0.4%	77%,0.3%
				1160.45
$W \to \mu\nu$	- , $3 \cdot 10^{-1}$%	5.4%,$2 \cdot 10^{-2}$%	53%,$1 \cdot 10^{-2}$%	80%,$8 \cdot 10^{-3}$%
				28.58
$\gamma, \gamma + Z \to \nu\nu$	- , $6 \cdot 10^{-3}$%	21%,$1 \cdot 10^{-3}$%	40%,$5 \cdot 10^{-4}$%	1.1%,$5 \cdot 10^{-6}$%
				151.03
Total Bkg	- , $7 \cdot 10^{-4}$%	4.3%,$3 \cdot 10^{-5}$%	49%,$2 \cdot 10^{-5}$%	47%,$7 \cdot 10^{-6}$%
				96183.24

Table 7.3: Comparison of multi-jet background prediction, in bins of transverse mass, for templates obtained by inverting isolation and by inverting the track and super-cluster matching requirement. There is an uncertainty of 50% on each prediction.

m_{T} range	inverted isolation	inverted track/SC matching
(25, 50)	79 ± 40	76 ± 38
(50, 75)	2900 ± 1500	1800 ± 890
(75, 100)	440 ± 220	300 ± 150
(100, 125)	55 ± 28	15.8 ± 7.9
(125, 150)	13.4 ± 6.8	0.0 ± 0.0

CHAPTER 8

RESULTS

Table 8.1 gives the number of events surviving after all the selection steps for different transverse mass thresholds. The Table shows the number of events for data corresponding to an integrated luminosity of 36.1 pb^{-1} (bottom row) and for all of the expected backgrounds (individually and the total number). The dominant background for all transverse mass ranges is $W \rightarrow e\nu$, as expected, given its almost identical signature to the W' signal.

The agreement between data and our background estimation in the high m_T region is good, as shown in Fig. 8.1, and the number of events in data and our background estimation are compatible within uncertainty. This is more apparent in the cumulative distribution of Fig. 8.2, which shows the number of selected events above a given transverse mass threshold. Figures 8.3, 8.4, and 8.5 show the comparison of data and the expected background contributions for different kinematic variables. These distributions demonstrate good agreement between the two.

Figure 8.6 shows the event displays for the highest transverse mass candidate recorded in 2010, with a transverse mass of 707 GeV. Table 8.2 summarizes the characteristics and most relevant kinematic variables of this event.

8.1 Systematic Uncertainties

We consider several different sources of systematic uncertainties in this analysis. Systematic uncertainties concern on one hand effects due to our imperfect understanding of the detector in the early stage of running, such as calibration or

Table 8.1: Expected number of standard model background event counts and observed data event counts, as a function of minimum m_T requirement. The uncertainties include statistical and systematic uncertainties, except the luminosity uncertainty.

Sample	> 45	> 100	> 200	> 400	> 650	> 750
$W \to e\nu$	84209± 363	1090± 238	38.0± 3.5	2.57± 0.44	0.31± 0.15	0.16± 0.10
multi-jet	7700± 3855	162± 81	6.5± 3.4	0.45± 0.32	0.11± 0.13	0.11± 0.13
$t\bar{t}$	88± 35	35± 14	4.9± 2.0	0.17± 0.08	0.00± 0.00	0.00± 0.00
$W \to \tau\nu$	1160± 85	17± 3	1.0± 0.3	0.00± 0.00	0.00± 0.00	0.00± 0.00
Other bkg	425± 88	25± 5	2.2± 0.4	0.15± 0.04	0.04± 0.04	0.01± 0.01
Total bkg	93584± 3876	1329± 254	52.7± 5.4	3.34± 0.55	0.46± 0.20	0.28± 0.16
Data	93878	1347	47	3	1	0

uncertainty on the luminosity. Other effects are uncertainties on parton distribution functions (PDFs), the properties of the W boson, and the W' production cross section. We assume that all systematic errors are uncorrelated. Some effects, such as the width of the W boson, are shape sensitive and considered only up to the extent that the number of events may change. Table 8.3 reports the systematic uncertainties and their impact on the signal and background yield for events with $m_T > 500$ GeV. What follows is an enumeration of the systematic uncertainties that we consider.

8.1.1 Luminosity

The uncertainty on the integrated luminosity is 11% [68]. This uncertainty is dominated by the measurement of the beam currents. The RMS measurement

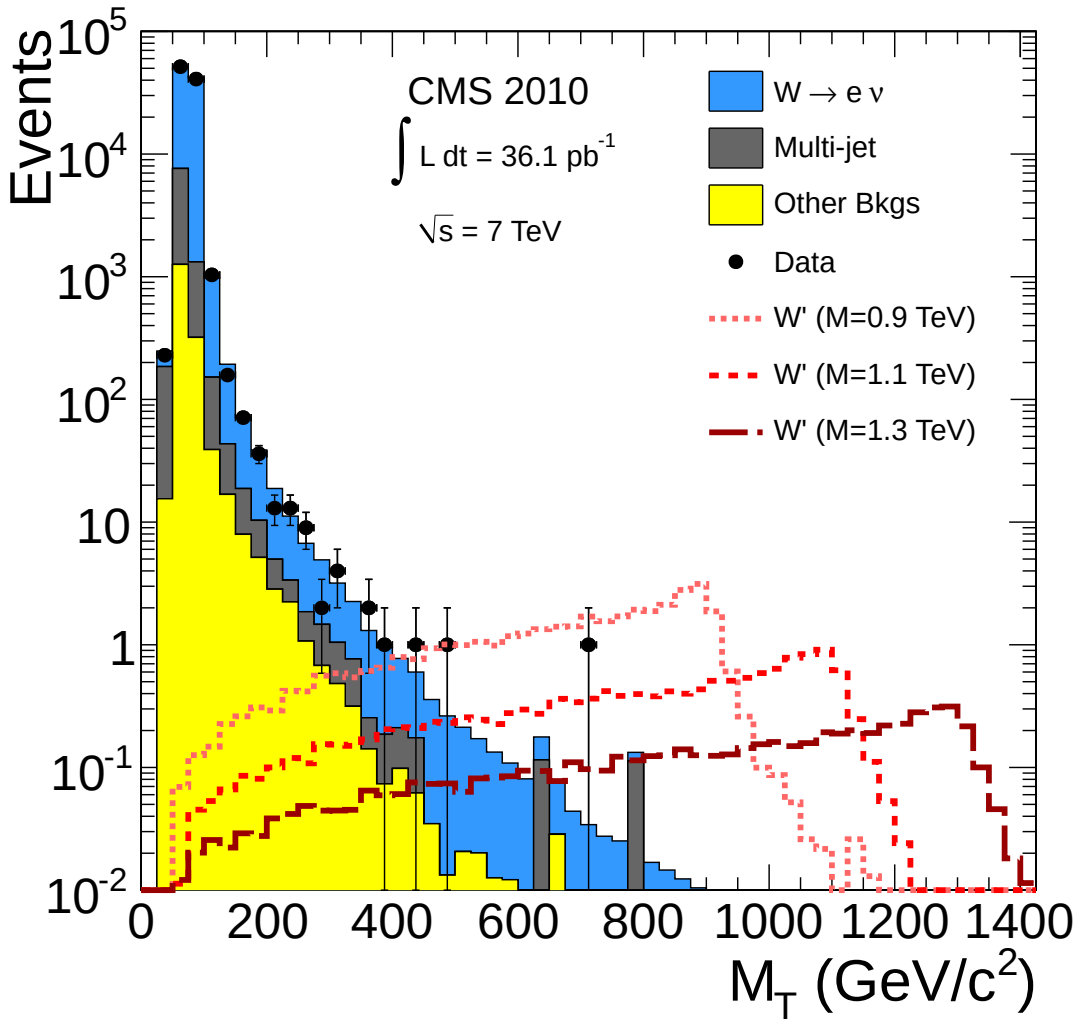

Figure 8.1: Transverse mass distribution for all standard model backgrounds and data. We see good agreement between the two.

is currently at 5% per beam. As the multi-jet and $W \rightarrow e\nu$ background are normalized to the data, the luminosity uncertainty does not affect the two largest backgrounds. Due to the small size of the contribution from the backgrounds taken from simulation, the luminosity uncertainty does not have a large effect on the total background uncertainty.

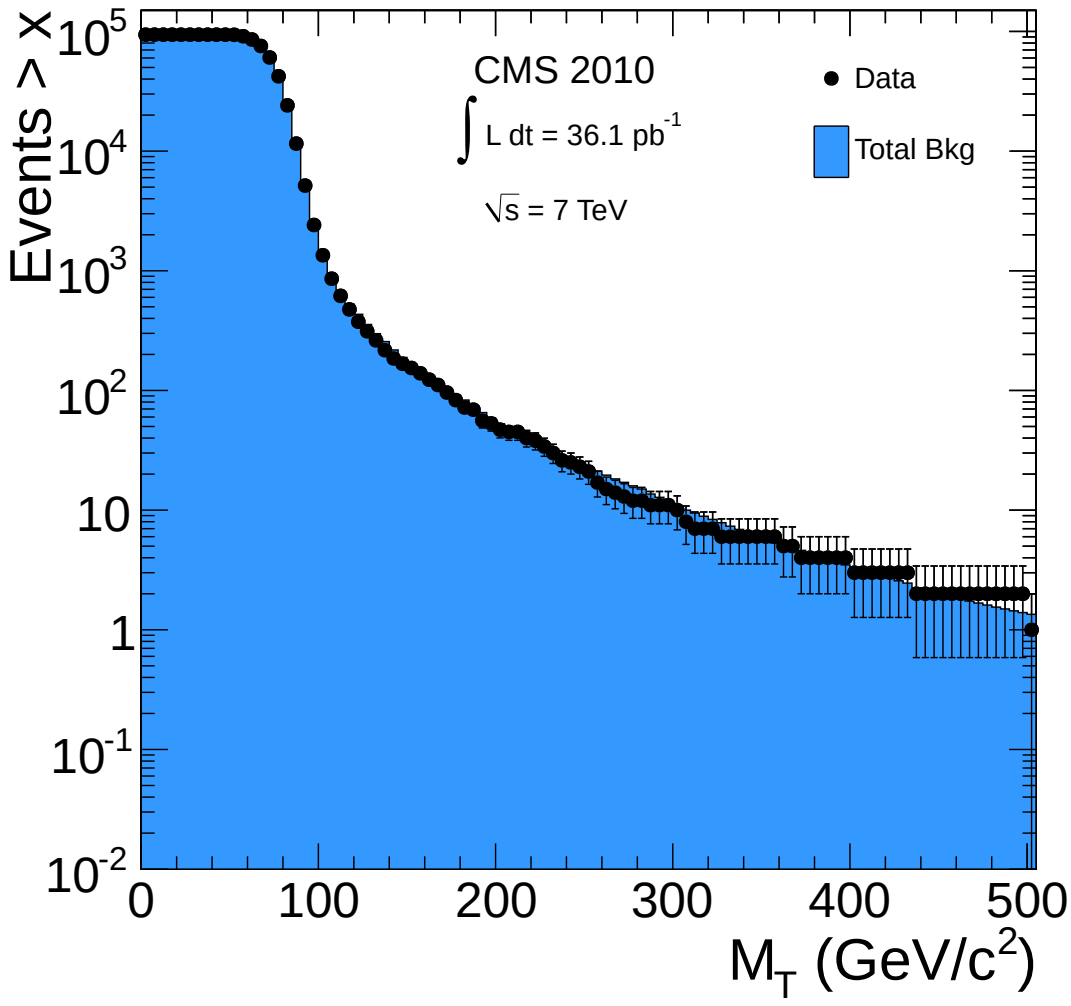

Figure 8.2: Cumulative distribution as a function of the transverse mass threshold. We see good agreement between data and the expected background.

8.1.2 Electron efficiency

As described in Sec. 6.1.5, the electron efficiencies and their statistical uncertainties are determined from $Z \to e^+e^-$ events using the tag-and-probe method. The reconstruction efficiency (i.e., the efficiency in forming a GSF electron from a super-cluster) has an uncertainty of 1.9% [62], mostly due to low statistics. The

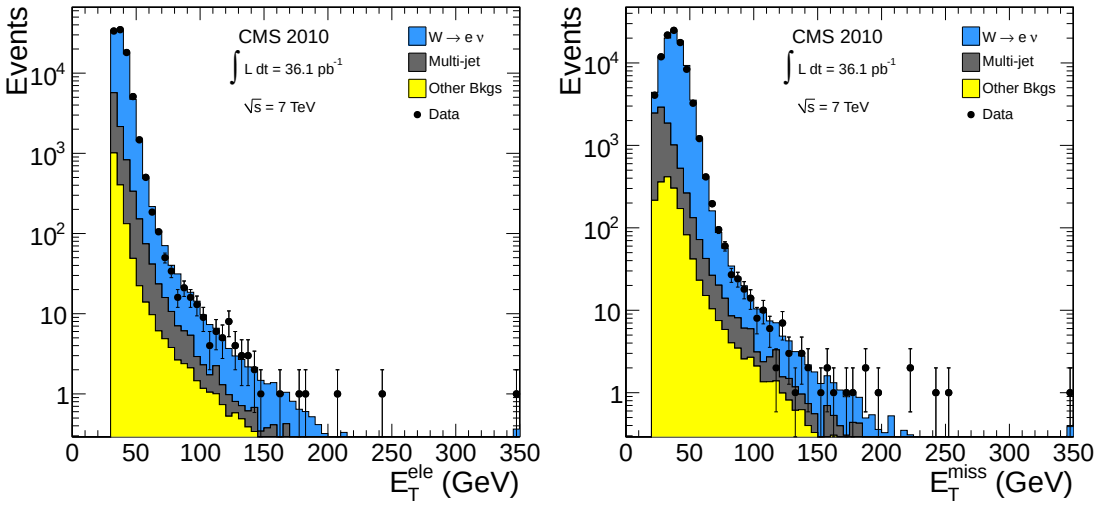

Figure 8.3: Left: Distribution of electron E_T. Right: Distribution of particle-flow $\not{E}_T$. Both distributions show good agreement.

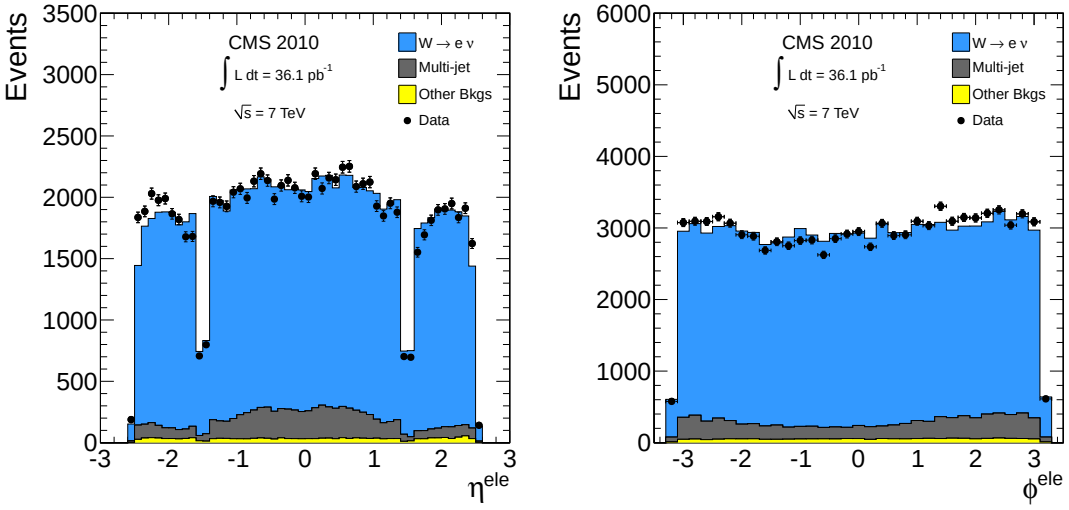

Figure 8.4: Left: Distribution of electron η. Right: Distribution of electron ϕ. Both distributions show good agreement.

efficiency of the electron identification with respect to reconstruction was measured by the High p_T Electron Group for high p_T electrons ($p_T > 25$ GeV) to be better than 1.5% [69]. For the HLT efficiency, we assume a systematic uncer-

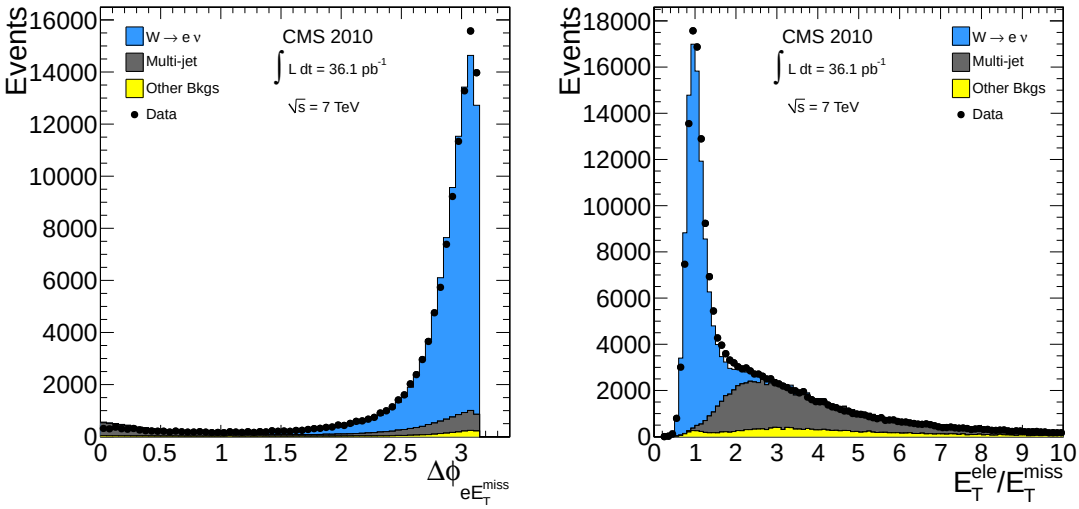

Figure 8.5: Left: The angular difference $\Delta\phi_{e\not{E}_T}$ for signal and backgrounds. Right: The ratio between the electron transverse energy and the missing transverse energy for signal and backgrounds.

tainty of 2% for high E_T W' electrons, and we include this uncertainty on the W' acceptance in the limit calculation. The effect of this on our final limit is marginal. As the normalization of the $W \to e\nu$ and multi-jet backgrounds are data-driven, the uncertainty on the efficiencies are absorbed into the normalization procedure.

8.1.3 Electron energy scale

Imperfect calibration of the electromagnetic calorimeter has a direct influence on the electron energy scale and resolution. From Sec. 6.1.4, the electron energy scale factor is 1% (4%) in the ECAL barrel (endcap). Due to the changing nature of the ECAL calibration, energy dependence, etc., we assume that the uncertainty on the energy scale correction is less than the size of the correction itself. The impact of the scale uncertainty on the number of events in our search win-

Table 8.2: Characteristics of the event with the highest transverse mass recorded in 2010.

Variable	Value
Transverse mass	707 GeV
$\Delta\phi_{e\not{E}_{\mathrm{T}}}$	3.10
$E_{\mathrm{T}}^{ele}/\not{E}_{\mathrm{T}}$	1.03
pf $\not{E}_{\mathrm{T}}$	348 GeV
Electron	
E_{T}	359 GeV
η	-1.071
ϕ	2.167
$E_{\mathrm{SC}}/p_{\mathrm{trk}}$	1.09924
H/E	0.00
$\Delta\eta$(trk, SC)	0.0030
$\Delta\phi$(trk, SC)	-0.0012
$\sigma_{i\eta i\eta}$	0.0087
seed Energy	235 GeV
seed Time	4.817 ns

dow depends on the background source in question, as each background has a different electron energy distribution. We find the following uncertainties on the number of events with high m_{T} ($m_{\mathrm{T}} > 200$ GeV) for the background estimates taken from simulation: 5% for $W \to \tau\nu$ events, 2.5% for $Z \to e^+e^-$ events, 1% for $t\bar{t}$ events, and negligible impact for other simulated backgrounds and for the W' signals at high E_{T}.

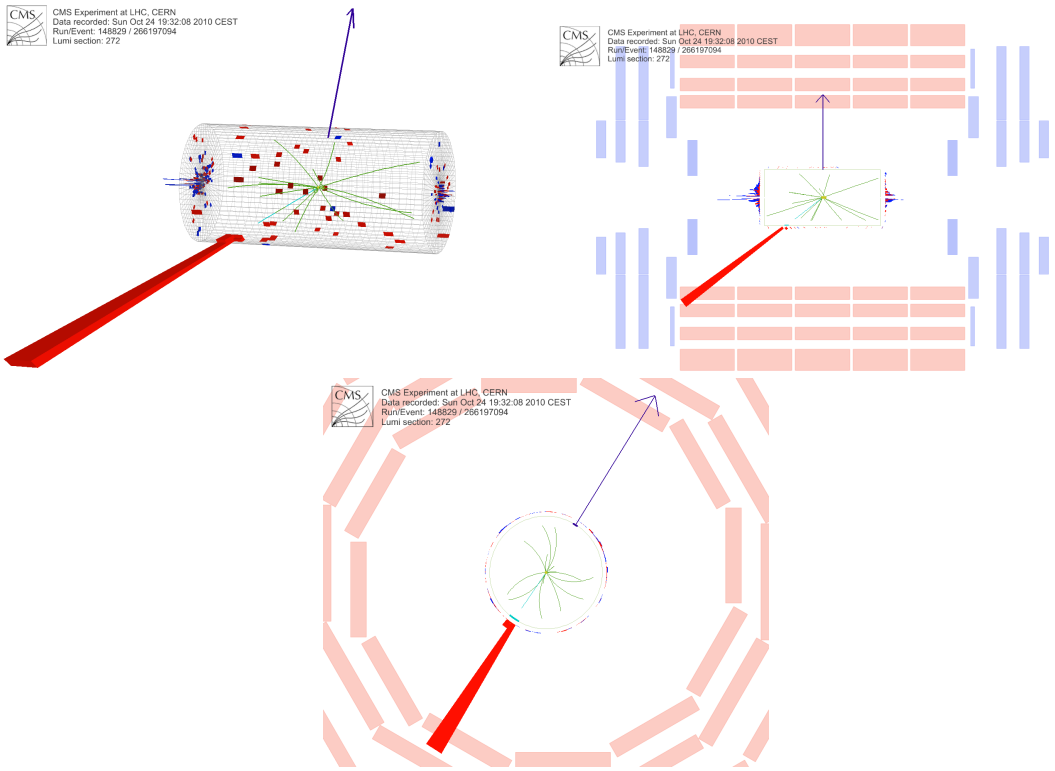

Figure 8.6: Event displays of the highest transverse mass event that passes our selection. Top Left: 3D view. Top Right: ρ–z view. Bottom: $\rho - \phi$ view.

For the multi-jet background, the electron energy scale uncertainty is included in our estimate of 50% for the number of these events. To see the effect of this uncertainty for the $W \rightarrow e\nu$ background, we create three different transverse mass distributions using the hadronic recoil correction method: a nominal shape (as described in Sec. 7.3.1), a shape constructed by scaling the electron energy up by the energy scale uncertainty, and a shape constructed by scaling it down by the uncertainty. Each of the three shapes are normalized to the predicted number of W boson events. The difference between the scaled up / down estimates and the nominal estimate gives us the systematic uncertainty due to the electron energy scale for this background.

Table 8.3: Systematic uncertainties and their impact on the signal and background event yield after requiring $m_{\mathrm{T}} > 500$ GeV.

Source of systematic error	Uncertainty	Signal	Total Bkg
Integrated luminosity	11%	11%	0.84%
Electron reco efficiency	1.9%	1.9%	0.14%
Electron ID efficiency	1.5%	1.5%	0.11%
Electron energy scale	1%(EB), 4%(EE)	0.4%	9.9%
$\not{E}_{\mathrm{T}}$ scale	5%	1.6%	1.4%
$\not{E}_{\mathrm{T}}$ resolution	10%	0.9%	0.5%
Cross section		10%	1.1%
Total (lumi not included)		10.5%	10.1%

8.1.4 ECAL saturation

Biases in the electron energy reconstruction at very high energies can be induced by saturation in the electromagnetic calorimeter electronics. Saturation occurs for energy deposits in a single crystal above (roughly) 1.7 TeV in the barrel and 3 TeV in the endcap. This does not affect our analysis in the case of low W' mass values. Previous simulation studies revealed that at most 16% of the events at the highest mass point studied (5 TeV) were affected, causing a slight shift in the transverse mass distribution. Hence, even without corrections, saturation will not compromise this study.

8.1.5 $\not\!\!E_{\mathrm{T}}$ resolution and scale

We assume an uncertainty of 10% on the $\not\!\!E_{\mathrm{T}}$ resolution. To evaluate the impact of this uncertainty on our background estimate, we add a 10% smearing to the x- and y-components of the reconstructed $\not\!\!E_{\mathrm{T}}$ in the simulation, and we evaluate the difference in the number of events in our m_{T} search window with respect to the unsmeared distribution. For all backgrounds, the impact on the number of events is below 1%. We also test a more conservative value of 20% for the $\not\!\!E_{\mathrm{T}}$ resolution uncertainty, resulting in a difference in the number of events within 5% of the event yields for all the backgrounds considered.

We use a similar approach to evaluate the impact of the uncertainty on the $\not\!\!E_{\mathrm{T}}$ scale. We apply a shift of 5% event-by-event to the $\not\!\!E_{\mathrm{T}}$ value, and the impact on the event yield with $m_{\mathrm{T}} > 200$ GeV is smaller than 10% for all backgrounds. For the $W \to e\nu$ background, we use the hadronic recoil correction method to obtain the $\not\!\!E_{\mathrm{T}}$ shape, and we get the uncertainty on $\not\!\!E_{\mathrm{T}}$ in the same way. There is an uncertainty on each value of the mean and sigma for both u_1 and u_2. Assuming maximal correlation / anti-correlation between values, we can determine a maximum spread on the $\not\!\!E_{\mathrm{T}}$, and therefore the m_{T}, distribution using the hadronic recoil. From this, we obtain the uncertainty on the $W \to e\nu$ background.

8.1.6 Cross section and PDF

For the W' signal, the uncertainty on the cross section, mostly due to uncertainties in the parton distribution functions (PDFs), varies between 6% (for $m_{W'}$ = 600 GeV) and 17% (for $m_{W'}$ = 2.0 TeV). The effect of the PDF uncertainty on the W' acceptance (the number of events passing our selection) is marginal (~0.5%).

According to the official cross sections used by the CMS experiment [70], the uncertainty on the di-boson (WW, WZ, ZZ) production cross section is less than 5%, and the uncertainty on the $Z \rightarrow e^+e^-$ cross section is about 5%. The latter uncertainty includes effects due to PDFs, the value of the strong coupling constant (α_S), and the factorization / renormalization scales. For $t\bar{t}$, we assume an uncertainty of 39%, as resulting from the CMS $t\bar{t}$ cross section measurement performed in pp collisions at $\sqrt{s} = 7$ TeV [71]. The measured $t\bar{t}$ cross section value is in agreement with the theoretical prediction for which the uncertainty is around 15% [70].

8.2 Statistical Analysis

Since we observe no excess in the data beyond our standard model background prediction, we set a lower bound on the mass of the W' boson, under the model assumptions described in Sec. 2.3. A potential W' signal would peak at large values of transverse mass. To reduce the amount of background in the search window without significantly affecting the signal yield, we put a high cut on the transverse mass, the last cut in the selection chain. For each mass point, we choose a minimum m_{T} requirement that proves the best *a priori* limit, and we take this to be our search window. The resultant minimum m_{T} requirement ranges from 425 - 800 GeV across our W' mass range.

We use a Bayesian technique to determine an upper limit on the cross section of each of our W' boson mass points with a confidence of 95%. This technique and the code to calculate the limit have been used at the D0 experiment [72]. A flat prior is assumed for the signal cross section. To incorporate the systematic

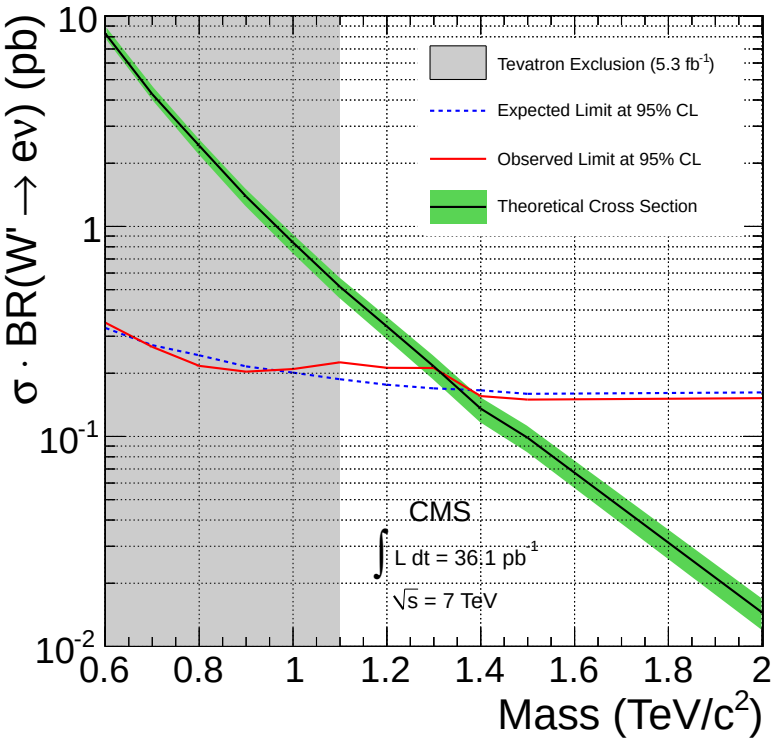

Figure 8.7: Limit using a Bayesian technique with a counting experiment in the search window, for the reference model. The intersection of the cross section limit curve and the central value of the theoretical cross section yields a lower limit of $m_{W'} > 1.32$ TeV/c^2 at 95% C.L. for the assumed $\sigma \cdot B(W' \to e\nu)$.

uncertainties described in the previous section, we treat the systematic uncertainty as a nuisance parameter and use a Log-Normal distribution to integrate over this parameter. In addition, we also tried a Gaussian and Gamma distribution, and they yielded results for the limit that were numerically the same.

Table 8.4 gives the inputs for this method, as well as the expected and observed limits. Figure 8.7 shows both the expected and the observed limit using this Bayesian cut-and-count technique. Using this method, we exclude the existence of the W' boson with standard model-like couplings with masses below 1.32 TeV at a 95% confidence level (compared to an expected limit of 1.36 TeV).

Table 8.4: Lower m_{T} requirement as a function of W' mass and expected and observed data counts. The entries n_s, n_b, and n_d correspond to the expected signal and background counts and the observed data counts, respectively. The cross sections σ_t, σ_e, and σ_o correspond to the theoretical W' production cross section and the expected and observed limits, respectively. The errors include all systematic uncertainties.

$m_{W'}$ (TeV/c^2)	min m_{T} (TeV/c^2)	n_{s}	n_{b}	n_{d}	σ_t (pb)	σ_e (pb)	σ_o (pb)
0.6	0.425	139.14 ± 21.89	2.57 ± 0.48	3	8.290	0.329	0.348
0.7	0.450	79.91 ± 12.37	1.97 ± 0.40	2	4.264	0.272	0.267
0.8	0.500	46.00 ± 7.09	1.35 ± 0.33	1	2.426	0.244	0.217
0.9	0.525	28.53 ± 4.37	1.13 ± 0.31	1	1.389	0.216	0.203
1.0	0.575	17.25 ± 2.64	0.83 ± 0.28	1	0.838	0.201	0.209
1.1	0.650	10.31 ± 1.59	0.46 ± 0.20	1	0.516	0.187	0.225
1.2	0.650	7.09 ± 1.09	0.46 ± 0.20	1	0.334	0.176	0.212
1.3	0.675	4.63 ± 0.71	0.38 ± 0.18	1	0.215	0.169	0.212
1.4	0.800	2.67 ± 0.41	0.12 ± 0.09	0	0.136	0.166	0.156
1.5	0.800	2.02 ± 0.31	0.12 ± 0.09	0	0.099	0.160	0.150
2.0	0.800	0.29 ± 0.04	0.12 ± 0.09	0	0.014	0.162	0.152

CHAPTER 9

CONCLUSION

The new energy regime of the LHC provides a wonderful opportunity to explore physics at the TeV scale. Both the LHC and the CMS detector were built to help answer some of the most fundamental questions of particle physics and search for new physics beyond the standard model.

We searched for a potential new, heavy, charged vector boson W' in the decay channel of an electron and neutrino using 36.1 pb^{-1} of the 2010 LHC data of pp collisions at a center-of-mass energy of 7 TeV. We based the event selection on high p_{T} electrons and $\not{E}_{\text{T}}$, and we optimized the selection for a signal that would peak at large values of transverse mass. We applied data driven methods to derive the contributions from multi-jet and W boson events. In addition, we took into account systematic uncertainties due to electron efficiencies, electron energy scale, luminosity, and signal and background cross sections.

In the transverse mass region of $m_{\text{T}} > 650$ GeV, we expected 0.46 background events in 36.1 pb^{-1} of data, and we see one. As we did not see a significant excess in the data, we set a lower-bound on the mass of the W' boson. Using a Bayesian technique, we excluded the existence of a W' boson with mass below 1.32 TeV with a confidence of 95%.

As of summer 2011, the LHC has already delivered over 2 fb^{-1}, and it is well on track to deliver several more fb^{-1} of data before the end of the year. This is an exciting time to be involved in high energy particle experiments, and I look forward to seeing what we find around the corner.

APPENDIX A

THE STANDARD MODEL LAGRANGIAN

The Lagrangian of the standard model can be separated into different pieces and written as

$$\mathcal{L}_{\text{SM}} = \mathcal{L}_{\text{Dirac}} + \mathcal{L}_{\text{mass}} + \mathcal{L}_{\text{gauge}} + \mathcal{L}_{WZA} + \mathcal{L}_{\text{gauge},\psi}. \tag{A.1}$$

The first term is the kinetic term for Dirac fermions

$$\begin{aligned}\mathcal{L}_{\text{Dirac}} = {} & i\bar{e}^i_L\gamma^\mu\partial_\mu e^i_L + i\bar{\nu}^i_L\gamma^\mu\partial_\mu \nu^i_L + i\bar{e}^i_R\gamma^\mu\partial_\mu e^i_R \\ & + i\bar{u}^i_L\gamma^\mu\partial_\mu u^i_L + i\bar{d}^i_L\gamma^\mu\partial_\mu d^i_L + i\bar{u}^i_R\gamma^\mu\partial_\mu u^i_R + i\bar{d}^i_R\gamma^\mu\partial_\mu d^i_R\end{aligned} \tag{A.2}$$

where the indices i = 1,2,3 runs over the three generations. The second term in Eq. (A.1) gives the masses of the fermions and bosons with

$$\mathcal{L}_{\text{mass}} = \frac{\upsilon}{\sqrt{2}}\left(\lambda^i_e\bar{e}^i_L e^i_R + \lambda^i_u\bar{u}^i_L u^i_R + \lambda^i_d\bar{d}^i_L d^i_R + h.c.\right) + m^2_W W^+_\mu W^{-\mu} + \frac{m^2_Z}{2}Z_\mu Z^\mu. \tag{A.3}$$

The third term in Eq. (A.1) is the kinetic term for the gauge bosons (in the mass basis)

$$\mathcal{L}_{\text{gauge}} = -\frac{1}{4}\left(G^a_{\mu\nu}\right)^2 - \frac{1}{2}W^+_{\mu\nu}W^{-\mu\nu} - \frac{1}{4}Z_{\mu\nu}Z^{\mu\nu} - \frac{1}{4}F_{\mu\nu}F^{\mu\nu} \tag{A.4}$$

where the index a = 1 to 8 runs over the 8 gluon field color combinations and

$$\begin{aligned}G^a_{\mu\nu} &= \partial_\mu A^a_\nu - \partial_\nu A^a_\mu - g_3 f^{abc}A^b_\mu A^c_\mu \\ W^\pm_{\mu\nu} &= \partial_\mu W^\pm_\nu - \partial_\nu W^\pm_\mu \\ Z_{\mu\nu} &= \partial_\mu Z_\nu - \partial_\nu Z_\mu \\ F_{\mu\nu} &= \partial_\mu A_\nu - \partial_\nu A_\mu.\end{aligned} \tag{A.5}$$

Originally, the kinetic term in the Lagrangian involved the $SU(2)_L$ and the $U(1)_Y$ fields W^i_μ and B_μ. After switching to the mass basis ($W^i_\mu, B_\mu \rightarrow W^\pm_\mu, Z_\mu, A_\mu$),

the kinetic term describes the interactions between these fields with the Lagrangian given by

$$\begin{aligned}\mathcal{L}_{WZA} = & ig_L \cos\theta_W \left[\left(W_\mu^- W_\nu^+ - W_\nu^- W_\mu^+\right)\partial^\mu Z^\nu + W_{\mu\nu}^+ W^{-\mu} Z^\nu - W_{\mu\nu}^- W^{+\mu} Z^\nu\right] \\ & + ie\left[\left(W_\mu^- W_\nu^+ - W_\nu^- W_\mu^+\right)\partial^\mu A^\nu + W_{\mu\nu}^+ W^{-\mu} A^\nu - W_{\mu\nu}^- W^{+\mu} A^\nu\right] \\ & + g_L^2 \cos^2\theta_W \left(W_\mu^+ W_\nu^- Z^\mu Z^\nu - W_\mu^+ W^{\mu-} Z_\nu Z^\nu\right) \\ & + g_L^2 \left(W_\mu^+ W_\nu^- A^\mu A^\nu - W_\mu^+ W^{\mu-} A_\nu A^\nu\right) \\ & + g_L e \cos\theta_W \left[W_\mu^+ W_\nu^- \left(Z^\mu A^\nu + Z^\nu A^\mu\right) - 2W_\mu^+ W^{\mu-} Z_\nu A^\nu\right] \\ & + \frac{g_L^2}{2}\left(W_\mu^+ W_\nu^-\right)\left(W^{\mu+} W^{\nu-} - W^{\nu+} W^{\mu-}\right).\end{aligned} \tag{A.6}$$

The final term in Eq. (A.1) comes from the interaction between the gauge bosons and the fermions with

$$\mathcal{L}_{\text{gauge},\psi} = -g_3 A_\mu^a J_3^{\mu a} - g_L\left(W_\mu^+ J_{W^+}^\mu + W_\mu^- J_{W^-}^\mu + Z_\mu J_Z^\mu\right) - eA_\mu J_A^\mu \tag{A.7}$$

where the standard model currents are given by

$$\begin{aligned}J_{W^+}^\mu &= \frac{1}{\sqrt{2}}\left(\bar{\nu}_L^i \gamma^\mu e_L^i + V^{ij}\bar{u}_L^i \gamma^\mu d_L^j\right) \\ J_{W^-}^\mu &= \frac{1}{\sqrt{2}}\left(\bar{e}_L^i \gamma^\mu \nu_L^i + V^{ij*}\bar{d}_L^j \gamma^\mu u_L^i\right) \\ J_Z^\mu &= \frac{1}{\cos\theta_w}\left[\left(\frac{1}{2}\right)\bar{\nu}_L^i \gamma^\mu \nu_L^i + \left(-\frac{1}{2} + \sin^2\theta_W\right)\bar{e}_L^i \gamma^\mu e_L^i + \left(\sin^2\theta_W\right)\bar{e}_R^i \gamma^\mu e_R^i\right. \\ &\quad + \left(\frac{1}{2} - \frac{2}{3}\sin^2\theta_W\right)\bar{u}_L^i \gamma^\mu u_L^i + \left(-\frac{2}{3}\sin^2\theta_W\right)\bar{u}_R^i \gamma^\mu u_R^i \\ &\quad \left. + \left(-\frac{1}{2} + \frac{1}{3}\sin^2\theta_W\right)\bar{d}_L^i \gamma^\mu d_L^i + \left(\frac{1}{3}\sin^2\theta_W\right)\bar{d}_R^i \gamma^\mu d_R^i\right] \\ J_A^\mu &= (-1)\,\bar{e}^i \gamma^\mu e^i + \left(\frac{2}{3}\right)\bar{u}^i \gamma^\mu u^i + \left(-\frac{1}{3}\right)\bar{d}^i \gamma^\mu d^i.\end{aligned} \tag{A.8}$$

APPENDIX B

HEAVY GAUGE BOSON PRODUCTION

As mentioned above, there are many theories that predict new gauge bosons that are analogues of the standard model W and Z bosons. In this section, we work through one such theory in detail. The theory which we consider was recently discussed in [25], and we follow the effective Lagrangian notation of [29].

Whatever the gauge group of the ultimate theory of new physics is, we consider the case where it includes

$$SU(2)_1 \otimes SU(2)_2 \otimes U(1)_Y \tag{B.1}$$

which is similar to the group of electroweak interactions, but it contains an extra *SU(2)* group. All of the standard model fermion doublets and the Higgs doublet transform under $SU(2)_1$, and they are singlets under $SU(2)_2$. In addition to the standard model scalar field ϕ, there is a bifundamental scalar field Φ that transforms under $SU(2)_1 \otimes SU(2)_2$ as $\Phi \to U_1 \Phi U_2^\dagger$. The fermion and scalar fields and their charge assignments under the different gauge groups are given in Tab. B.1.

We require that the neutral components of Φ acquire a VEV

$$\langle \Phi \rangle = \frac{1}{\sqrt{2}} \begin{pmatrix} f & 0 \\ 0 & f \end{pmatrix} \tag{B.2}$$

such that $U(1)_{\mathrm{EM}}$ remains unbroken. The spontaneous symmetry breaking pattern here is $SU(2)_1 \otimes SU(2)_2 \to SU(2)_L$. We can write the covariant derivative as

$$D_\mu = \partial_\mu - i g_1 V_{1\,\mu}^a T_a + i g_2 V_{2\,\mu}^b T_b + i g_X X_\mu Y \tag{B.3}$$

Table B.1: The matter fields and their representations in this $SU(2)_1 \otimes SU(2)_2 \otimes U(1)_Y$ model.

Field	$SU(3)$	$SU(2)_1$	$SU(2)_2$	$U(1)_Y$
$Q_L = \begin{pmatrix} u_L \\ d_L \end{pmatrix}$	**3**	**2**	**1**	$\frac{1}{6}$
u_R	**3**	**1**	**1**	$\frac{2}{3}$
d_R	**3**	**1**	**1**	$-\frac{1}{3}$
$L_L = \begin{pmatrix} \nu_L \\ e_L \end{pmatrix}$	**1**	**2**	**1**	$-\frac{1}{2}$
e_R	**1**	**1**	**1**	-1
$\phi = \begin{pmatrix} \phi^+ \\ \phi^0 \end{pmatrix}$	**1**	**2**	**1**	$\frac{1}{2}$
$\Phi = \begin{pmatrix} \eta_1^0 & \eta_1^+ \\ \eta_2^- & \eta_2^0 \end{pmatrix}$	**1**	**2**	$\bar{\mathbf{2}}$	0

where $V^a_{1\,\mu}$, $V^b_{2\,\mu}$, and X_μ are associated with the groups $SU(2)_1$, $SU(2)_2$, and $U(1)_Y$, respectively. The covariant derivative acting on the bifundamental scalar field can be written as

$$D_\mu \Phi = \partial_\mu \Phi - i g_1 V^a_{1\,\mu} \frac{\sigma^a}{2} \Phi + i g_2 V^b_{2\,\mu} \Phi \frac{\sigma^b}{2} \tag{B.4}$$

where we have used $Y = 0$ for this field, and we have written the generators of *SU(2)* in terms of the Pauli matrices. We are most interested in how this field gives masses to the gauge bosons, and these come from the VEV in the kinetic term of the bifundamental field. It is easiest to work out this term using indices

where $\langle\Phi\rangle_{ij} = \frac{f}{\sqrt{2}}\delta_{ij}$. The VEV of the kinetic term is

$$\begin{aligned}\mathrm{tr}\left[\left|D_\mu \langle\Phi\rangle\right|^2\right] &= \left[ig_1 V_{1\,\mu}^a \left(\frac{\sigma^a}{2}\right)_{ij} \frac{f}{\sqrt{2}}\delta_{jk} - ig_2 V_{2\,\mu}^b \frac{f}{\sqrt{2}}\delta_{ij}\left(\frac{\sigma^b}{2}\right)_{jk}\right] \times \\ &\quad \left[-ig_1 V_1^{\bar{a}\,\mu}\left(\frac{\sigma^{\bar{a}}}{2}\right)_{km} \frac{f}{\sqrt{2}}\delta_{mi} + ig_2 V_2^{\bar{b}\,\mu}\frac{f}{\sqrt{2}}\delta_{km}\left(\frac{\sigma^{\bar{b}}}{2}\right)_{mi}\right] \\ &= \frac{f^2}{2}\Bigg[g_1^2 V_{1\,\mu}^a V_1^{\bar{a}\,\mu}\left(\frac{\sigma^a}{2}\right)_{ik}\left(\frac{\sigma^{\bar{a}}}{2}\right)_{ki} - g_1 g_2 V_{2\,\mu}^b V_1^{\bar{a}\,\mu}\left(\frac{\sigma^b}{2}\right)_{ik}\left(\frac{\sigma^{\bar{a}}}{2}\right)_{ki} \\ &\quad - g_1 g_2 V_{1\,\mu}^a V_2^{\bar{b}\,\mu}\left(\frac{\sigma^a}{2}\right)_{ik}\left(\frac{\sigma^{\bar{b}}}{2}\right)_{ki} + g_2^2 V_{2\,\mu}^b V_2^{\bar{b}\,\mu}\left(\frac{\sigma^b}{2}\right)_{ik}\left(\frac{\sigma^{\bar{b}}}{2}\right)_{ki}\Bigg].\end{aligned} \tag{B.5}$$

This can be simplified by using the property of the Pauli matrices that

$$\left(\frac{\sigma^a}{2}\right)_{ik}\left(\frac{\sigma^b}{2}\right)_{ki} = \mathrm{tr}\left[\frac{\sigma^a}{2}\,\frac{\sigma^b}{2}\right] = \frac{1}{2}\delta_{ab}. \tag{B.6}$$

which causes Eq. (B.5) to simplify to

$$\mathrm{tr}\left[\left|D_\mu \langle\Phi\rangle\right|^2\right] = \frac{f^2}{4}\left(g_1 V_1^a - g_2 V_2^a\right)^2. \tag{B.7}$$

Next, we make the following mass eigenstate definitions

$$\begin{pmatrix} \widehat{W}'^{\,a} \\ \widehat{W}^a \end{pmatrix} = \begin{pmatrix} \cos\tilde{\phi} & -\sin\tilde{\phi} \\ \sin\tilde{\phi} & \cos\tilde{\phi} \end{pmatrix}\begin{pmatrix} V_1^a \\ V_2^a \end{pmatrix} \quad \text{and} \quad \begin{aligned} \widehat{W}'^{\,\pm} &= \tfrac{1}{\sqrt{2}}\left(\widehat{W}'^{\,1} \mp i\widehat{W}'^{\,2}\right) \\ \widehat{W}^{\pm} &= \tfrac{1}{\sqrt{2}}\left(\widehat{W}^1 \mp i\widehat{W}^2\right) \\ \widehat{Z}' &= \widehat{W}'_3 \end{aligned} \tag{B.8}$$

where the angle $\tilde{\phi}$ is defined by

$$\cos\tilde{\phi} = \frac{g_1}{\sqrt{g_1^2 + g_2^2}}, \quad \sin\tilde{\phi} = \frac{g_2}{\sqrt{g_1^2 + g_2^2}}, \quad \text{and} \quad \tan\tilde{\phi} = \frac{g_2}{g_1}. \tag{B.9}$$

After these substitutions, Eq. (B.7) becomes

$$\mathrm{tr}\left[\left|D_\mu \langle\Phi\rangle\right|^2\right] = \frac{\widetilde{m}_{Z'}^2}{2}\widehat{Z}'_\mu \widehat{Z}'^{\,\mu} + \widetilde{m}_{W'}^2 \widehat{W}'^{\,+}_\mu \widehat{W}'^{\,-\,\mu} \tag{B.10}$$

where the masses of the heavy gauge bosons are

$$\tilde{m}_{Z'}^2 = \tilde{m}_{W'}^2 = \frac{1}{2}\left(g_1^2 + g_2^2\right) f^2. \tag{B.11}$$

At this stage, the heavy gauge boson eigenstates ($\widehat{W}'^{\pm}$, $\widehat{Z}'$) are degenerate in mass, and the electroweak gauge bosons ($\widehat{W}^{\pm}$,X_μ) are massless. Here, we are using the tilde symbol (~) for numbers (e.g., masses and coupling constants) and hats (∧) for fields (e.g., $\widehat{W}$ and $\widehat{Z}$) to indicate that these numbers and field are not equivalent to the standard model values and fields. For example, as we will see below, the symmetry breaking of the electroweak sector will induce mixing between $\widehat{W}$ and $\widehat{W}'$ such that the standard model W boson will be a combination of both fields.

As in the standard model, we require that the neutral components of ϕ acquire a VEV

$$\langle\phi\rangle = \frac{1}{\sqrt{2}}\begin{pmatrix} 0 \\ \tilde{v} \end{pmatrix} \tag{B.12}$$

that leads to a second stage of symmetry breaking $SU(2)_L \otimes U(1)_Y \rightarrow U(1)_{\text{EM}}$, electroweak symmetry breaking. This will lead to a shift in the masses of the heavy gauge bosons and give mass to the standard model weak gauge bosons. These masses come from the VEV in the kinetic term of the scalar field. This covariant derivative can be written as

$$\begin{aligned} D_\mu \langle\phi\rangle =& -ig_1\left(\cos\tilde{\phi}\widehat{W}'^{\,a}_\mu + \sin\tilde{\phi}\widehat{W}^a_\mu\right)\frac{\sigma^a}{2}\langle\phi\rangle - ig_X\frac{1}{2}X_\mu\langle\phi\rangle \\ =& -i\frac{\tilde{g}_{W'}}{\sqrt{2}}\left(\widehat{W}'^{\,+}_\mu\sigma^+ + \widehat{W}'^{\,-}_\mu\sigma^-\right)\langle\phi\rangle - i\frac{\tilde{g}_L}{\sqrt{2}}\left(\widehat{W}^+_\mu\sigma^+ + \widehat{W}^-_\mu\sigma^-\right)\langle\phi\rangle \\ & -i\frac{\tilde{g}_{W'}}{2}\widehat{Z}'_\mu\sigma^3\langle\phi\rangle - i\frac{\tilde{g}_L}{2}\widehat{W}^3_\mu\sigma^3\langle\phi\rangle - i\frac{\tilde{g}_Y}{2}X_\mu\langle\phi\rangle \end{aligned} \tag{B.13}$$

where we have used the field definitions in Eq. (B.9) and identified the couplings

$$\tilde{g}_{W'} = g_1 \cos\tilde{\phi} = \frac{g_1^2}{\sqrt{g_1^2 + g_2^2}}, \quad \tilde{g}_L = g_1 \sin\tilde{\phi} = \frac{g_1 g_2}{\sqrt{g_1^2 + g_2^2}}, \quad \text{and} \quad \tilde{g}_Y = g_X. \tag{B.14}$$

Using the couplings defined in this way, the VEV component of the kinetic term of the scalar field becomes

$$\begin{aligned} \left|D_\mu \langle\phi\rangle\right|^2 =& \frac{\tilde{\upsilon}^2}{4}\left[\tilde{g}_{W'}^2 \widehat{W}_\mu'^{\,+}\widehat{W}'^{\,-\mu} + \tilde{g}_L^2 \widehat{W}_\mu^+ \widehat{W}^{-\mu} + \tilde{g}_{W'}\tilde{g}_L\left(\widehat{W}_\mu'^{\,+}\widehat{W}^{-\mu} + \widehat{W}_\mu'^{\,-}\widehat{W}^{+\mu}\right)\right] \\ &+ \frac{\tilde{\upsilon}^2}{8}\left(\tilde{g}_{W'}\widehat{Z}'_\mu + \tilde{g}_L \widehat{W}_\mu^3 - \tilde{g}_Y X_\mu\right)^2 \end{aligned} \tag{B.15}$$

As we do in the case of the standard model, we can define a rotation between the neutral gauge bosons

$$\begin{pmatrix} \widehat{Z} \\ A \end{pmatrix} = \begin{pmatrix} \cos\tilde{\theta}_w & -\sin\tilde{\theta}_w \\ \sin\tilde{\theta}_w & \cos\tilde{\theta}_w \end{pmatrix}\begin{pmatrix} \widehat{W}^3 \\ X \end{pmatrix}. \tag{B.16}$$

where the angle $\tilde{\theta}_w$, the analog of the standard model Weinberg angle, is defined by

$$\cos\tilde{\theta}_w = \frac{\tilde{g}_L}{\sqrt{\tilde{g}_L^2 + \tilde{g}_Y^2}}, \quad \sin\tilde{\theta}_w = \frac{\tilde{g}_Y}{\sqrt{\tilde{g}_L^2 + \tilde{g}_Y^2}}, \quad \text{and} \quad \tan\tilde{\theta}_w = \frac{\tilde{g}_Y}{\tilde{g}_L}. \tag{B.17}$$

Once these rotations are made, we obtain

$$\begin{aligned} \left|D_\mu \langle\phi\rangle\right|^2 =& \frac{\tilde{\upsilon}^2}{4}\left[\tilde{g}_{W'}^2 \widehat{W}_\mu'^{\,+}\widehat{W}'^{\,-\mu} + \tilde{g}_L^2 \widehat{W}_\mu^+ \widehat{W}^{-\mu} + \tilde{g}_{W'}\tilde{g}_L\left(\widehat{W}_\mu'^{\,+}\widehat{W}^{-\mu} + \widehat{W}_\mu'^{\,-}\widehat{W}^{+\mu}\right)\right] \\ &+ \frac{\tilde{\upsilon}^2}{8}\left[\tilde{g}_{W'}^2 \widehat{Z}'_\mu \widehat{Z}'^\mu + 2\tilde{g}_{W'}\sqrt{\tilde{g}_L^2 + \tilde{g}_Y^2}\,\widehat{Z}'_\mu \widehat{Z}^\mu + \left(\tilde{g}_L^2 + \tilde{g}_Y^2\right)\widehat{Z}_\mu \widehat{Z}^\mu\right]. \end{aligned} \tag{B.18}$$

After the second sage of symmetry breaking, we find that the photon field, A_μ, remains massless, by design, and electromagnetism remains unbroken. As in the standard model, the electric charge, $\tilde{e}$, is given by

$$\frac{1}{\tilde{e}^2} = \frac{1}{\tilde{g}_L^2} + \frac{1}{\tilde{g}_Y^2} \tag{B.19}$$

The VEV of the standard model ϕ field gives masses to the $\widehat{W}^{\pm}$ and $\widehat{Z}$ bosons, but it also induces further $\widehat{W} - \widehat{W}'$ and $\widehat{Z} - \widehat{Z}'$ mixing. Combining Eq. (B.10) and Eq. (B.18), we can write the piece of the Lagrangian involving the gauge boson masses as

$$\begin{aligned}\mathcal{L}_{\text{gauge,mass}} = &\begin{pmatrix} \widehat{W}^{+}_{\mu} & \widehat{W}'^{+}_{\mu} \end{pmatrix} \begin{pmatrix} \tilde{m}^2_W & \delta\tilde{m}^2_W \\ \delta\tilde{m}^2_W & \tilde{m}^2_{W'} + \Delta\tilde{m}^2_{W'} \end{pmatrix} \begin{pmatrix} \widehat{W}^{-\mu} \\ \widehat{W}'^{+\mu}_{\mu} \end{pmatrix} \\ &+ \frac{1}{2} \begin{pmatrix} A_{\mu} & \widehat{Z}_{\mu} & \widehat{Z}'_{\mu} \end{pmatrix} \begin{pmatrix} 0 & 0 & 0 \\ 0 & \tilde{m}^2_Z & \delta\tilde{m}^2_Z \\ 0 & \delta\tilde{m}^2_Z & \tilde{m}^2_{Z'} + \Delta\tilde{m}^2_{Z'} \end{pmatrix} \begin{pmatrix} A^{\mu} \\ \widehat{Z}^{\mu} \\ \widehat{Z}'^{\mu} \end{pmatrix}\end{aligned} \tag{B.20}$$

where the masses and splittings are

$$\begin{aligned} \tilde{m}^2_W &= \frac{1}{4}\tilde{g}^2_L\tilde{v}^2, \quad \delta\tilde{m}^2_W = \frac{1}{4}\tilde{g}_L\tilde{g}_{W'}\tilde{v}^2, \quad \Delta\tilde{m}^2_{W'} = \frac{1}{4}\tilde{g}^2_{W'}\tilde{v}^2, \\ \tilde{m}^2_Z &= \frac{1}{4}\left(\tilde{g}^2_L + \tilde{g}^2_Y\right)\tilde{v}^2, \quad \delta\tilde{m}^2_Z = \frac{1}{4}\tilde{g}_{W'}\sqrt{\tilde{g}^2_L + \tilde{g}^2_Y}\,\tilde{v}^2, \quad \Delta\tilde{m}^2_{Z'} = \frac{1}{4}\tilde{g}^2_{W'}\tilde{v}^2. \end{aligned} \tag{B.21}$$

To remove the mixing term between the primed and unprimed gauge bosons, we can write the Lagrangian in Eq. (B.20) in terms of the mass eigenstates. Diagonalizing the mass matrices in Eq. (B.20), we find the mass eigenvalues to be (without the tilde)

$$\begin{aligned} m^2_{W,Z} &= \frac{1}{2}\left(\tilde{m}^2_{W',Z'} + \tilde{m}^2_{W,Z} + \Delta\tilde{m}^2_{W',Z'} - \sqrt{\left(\tilde{m}^2_{W',Z'} - \tilde{m}^2_{W,Z} + \Delta\tilde{m}^2_{W',Z'}\right)^2 + 4\delta\tilde{m}^4_{W,Z}}\right) \\ m^2_{W',Z'} &= \frac{1}{2}\left(\tilde{m}^2_{W',Z'} + \tilde{m}^2_{W,Z} + \Delta\tilde{m}^2_{W',Z'} + \sqrt{\left(\tilde{m}^2_{W',Z'} - \tilde{m}^2_{W,Z} + \Delta\tilde{m}^2_{W',Z'}\right)^2 + 4\delta\tilde{m}^4_{W,Z}}\right). \end{aligned} \tag{B.22}$$

We assume that the scale of the first breaking, f, is much larger than the electroweak scale, $\tilde{v}$, so that $\frac{\tilde{v}}{f^2} \ll 1$. With this assumption, the masses of the primed gauge bosons are larger than the mass terms in Eq. (B.21), and we can take the

approximation

$$\tilde{m}^2_{W',Z'} \gg \tilde{m}^2_{W,Z},\ \Delta\tilde{m}^2_{W',Z'},\ \delta\tilde{m}^2_{W,Z} \tag{B.23}$$

After making this approximation, we can write the mass eigenvalues in Eq. (B.23) as

$$\begin{aligned} m^2_{W,Z} &\approx \tilde{m}^2_{W,Z} - \frac{1}{\tilde{m}^2_{W',Z'}}\left(\delta\tilde{m}^4_{W,Z} + \frac{1}{4}\left(\tilde{m}^2_{W,Z} - \Delta\tilde{m}^2_{W',Z'}\right)^2\right) \\ m^2_{W',Z'} &\approx \tilde{m}^2_{W',Z'} + \Delta\tilde{m}^2_{W',Z'} + \frac{1}{\tilde{m}^2_{W',Z'}}\left(\delta\tilde{m}^4_{W,Z} + \frac{1}{4}\left(\tilde{m}^2_{W,Z} - \Delta\tilde{m}^2_{W',Z'}\right)^2\right) \end{aligned} \tag{B.24}$$

which is accurate up to $O\left(\tilde{m}^{-2}_{W',Z'}\right)$. We can also write out the mass eigenstates (without the hat) as

$$\begin{aligned} W_\mu &= -\widehat{W}_\mu + \tfrac{\delta\tilde{m}^2_W}{\tilde{m}^2_{W'}}\,\widehat{W}'_\mu \\ W'_\mu &= \tfrac{\delta\tilde{m}^2_W}{\tilde{m}^2_{W'}}\,\widehat{W}_\mu + \widehat{W}'_\mu \end{aligned} \quad \text{and} \quad \begin{aligned} Z_\mu &= -\widehat{Z}_\mu + \tfrac{\delta\tilde{m}^2_Z}{\tilde{m}^2_{Z'}}\,\widehat{Z}'_\mu \\ Z'_\mu &= \tfrac{\delta\tilde{m}^2_Z}{\tilde{m}^2_{Z'}}\,\widehat{Z}_\mu + \widehat{Z}'_\mu \end{aligned} . \tag{B.25}$$

Once we have the masses of the gauge bosons, we can write out the effective Lagrangian for interactions between the gauge bosons and the fermion fields (ignoring the strong interaction) as

$$\begin{aligned} \mathcal{L}_{\text{gauge},\psi} = &\left(\tilde{g}_{W'} + \tilde{g}_L\frac{\delta\tilde{m}^2_W}{\tilde{m}^2_{W'}}\right)\left(W'^+_\mu J^\mu_{W^+} + W'^-_\mu J^\mu_{W^-}\right) - \left(\tilde{g}_L - \tilde{g}_{W'}\frac{\delta\tilde{m}^2_W}{\tilde{m}^2_{W'}}\right)\left(W^+_\mu J^\mu_{W^+} + W^-_\mu J^\mu_{W^-}\right) \\ &+ Z'_\mu\left(\tilde{g}_{W'}J^\mu_{Z'} + \tilde{g}_L\frac{\delta\tilde{m}^2_W}{\tilde{m}^2_{W'}}J^\mu_Z\right) - Z_\mu\left(\tilde{g}_L J^\mu_Z + \tilde{g}_{W'}\frac{\delta\tilde{m}^2_W}{\tilde{m}^2_{W'}}J^\mu_{Z'}\right) + \tilde{e}A_\mu J^\mu_A \end{aligned} \tag{B.26}$$

with the currents

$$
\begin{aligned}
J^{\mu}_{W^+} &= \frac{1}{\sqrt{2}}\left(\bar{\nu}^i_L \gamma^\mu e^i_L + V^{ij}\bar{u}^i_L \gamma^\mu d^j_L\right) \\
J^{\mu}_{W^-} &= \frac{1}{\sqrt{2}}\left(\bar{e}^i_L \gamma^\mu \nu^i_L + V^{ij*}\bar{d}^j_L \gamma^\mu u^i_L\right) \\
J^{\mu}_{Z} &= \frac{1}{\cos\theta_w}\sum_f \bar{f}\gamma^\mu\left(T^3 - \sin^2\theta_w Q\right) f \\
J^{\mu}_{A} &= \sum_f \bar{f}\gamma^\mu Q f \\
J^{\mu}_{Z'} &= \sum_f \bar{f}\gamma^\mu T^3 f \ .
\end{aligned}
\tag{B.27}
$$

where $J^{\mu}_{W^\pm}$, J^{μ}_{Z}, and J^{μ}_{A} are the same as in the standard model. Note that the current associated with the W' and the W are the same, while the same is not true for the Z' and the Z.

Following the work of Han and Skiba [73], we assume that the effective Lagrangian at energies just above the electroweak scale can be written as

$$
\mathcal{L}_{\text{eff}} = \mathcal{L}_{\text{SM}} + a_i O_i \tag{B.28}
$$

where O_i are dimension six operators and a_i are coefficients with dimension of inverse mass squared. In this way, we can investigate constraints from electroweak precision measurements by considering the effect of our new physics model on these dimension six operators. For this analysis, we will focus on contributions due to heavy gauge boson exchange. Instead of calculating the shift in each of the relevant electroweak precision measurements, we can compare the standard model predictions to all relevant experimental data and calculate the χ^2 distribution as a function of a_i. Since we assume that the coefficients a_i are small, and our effective Lagrangian in Eq. (B.28) is linear in a_i, the χ^2 distribution

is quadratic in a_i with

$$\begin{aligned}\chi^2 &= \chi^2_{\text{min}} + (a_i - \hat{a}_i)\,\mathcal{M}_{ij}\left(a_j - \hat{a}_j\right) \\ &= \chi^2_{\text{SM}} + a_i\hat{v}_i + a_i\mathcal{M}_{ij}a_j\end{aligned} \tag{B.29}$$

where $\hat{a}_i$ are the values of a_i that minimize χ^2. The numerical values of $\hat{v}_i$ and $\mathcal{M}_{ij}$ are given in [73]. Using Eq. (B.26) and Eq. (B.27), we can integrate out the gauge bosons to obtain the effective four-fermion interactions. After this, we can identify the relevant couplings, a_i, as

$$a^t = -\frac{1}{4}\frac{\tilde{g}^2_{W'}}{\tilde{m}^2_{W'}} = -\frac{1}{4}\frac{g^2_{W'}}{m^2_{W'}}, \tag{B.30}$$

again accurate to $O\left(\tilde{m}^{-2}_{W'}\right)$. At 95% CL, corresponding to $\Delta\chi^2 = 3.84$, we obtain the bound on $g_{W'}$ as a function of $m_{W'}$. This bound from electroweak precision measurements and the 95% CL limit obtained in the analysis presented in the main text of this document are shown in Fig. B.1.

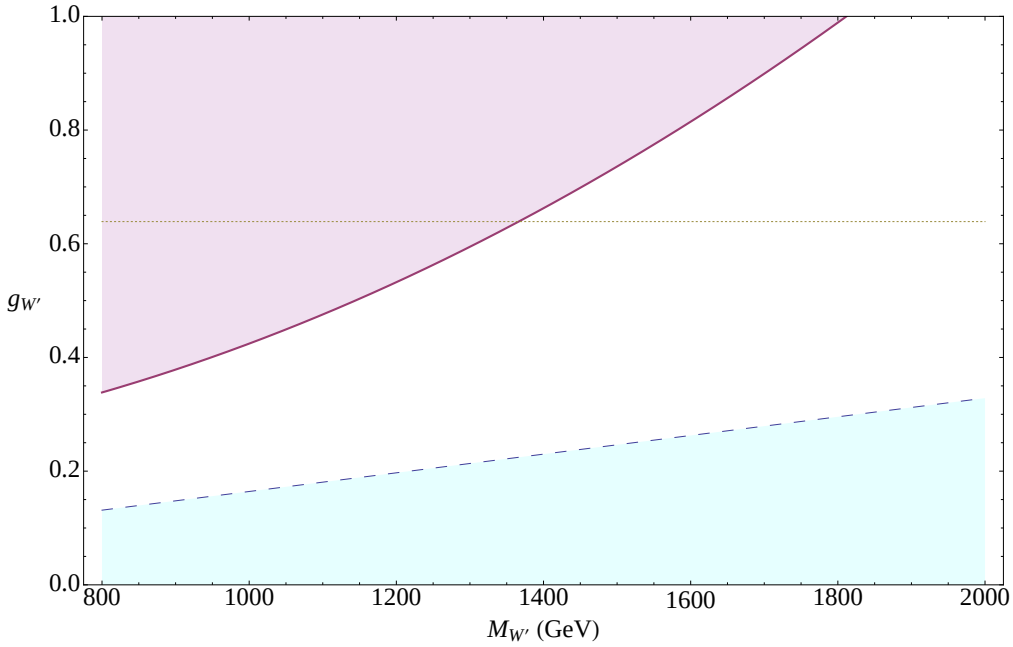

Figure B.1: The preferred value of the W' coupling, $g_{W'}$, as a function of the mass of the W', $m_{W'}$, from the electroweak precision fit at 95% CL (dotted blue line and below). Also shown is the exclusion from this analysis (solid line and above). For reference, the horizontal dotted line corresponds to the standard model value of g_L.

BIBLIOGRAPHY

[1] K Nakamura and Particle Data Group, Journal of Physics G: Nuclear and Particle Physics **37**, 075021 (2010), http://stacks.iop.org/0954-3899/37/i=7A/a=075021.

[2] N. Jarosik, C. L. Bennett, J. Dunkley, B. Gold, M. R. Greason, M. Halpern, R. S. Hill, G. Hinshaw, A. Kogut, E. Komatsu, et al., The Astrophysical Journal Supplement Series **192**, 14 (2011), http://stacks.iop.org/0067-0049/192/i=2/a=14.

[3] LEP Collaborations and LEP Electroweak Working Group (2010), http://lepewwg.web.cern.ch/LEPEWWG/plots/summer2010/.

[4] H.-L. Lai, M. Guzzi, J. Huston, Z. Li, P. M. Nadolsky, J. Pumplin, and C.-P. Yuan, Phys. Rev. D **82**, 074024 (2010), arXiv:hep-ph/1007.2241v3.

[5] X. Cid Vidal and R. Cid Manzano, *Taking a Closer Look at the LHC* (2011), http://www.lhc-closer.es/.

[6] S. White, *Determination of the absolute luminosity at the LHC* (2010), http://tel.archives-ouvertes.fr/tel-00537325/fr/.

[7] CMS Collaboration, JINST **3** (2008).

[8] CMS Collaboration, *CMS ECAL Technical Design Report* (1997).

[9] L. Tuura, A. Meyer, I. Segoni, and G. D. Ricca, Journal of Physics: Conference Series **219**, 072020 (2010), http://stacks.iop.org/1742-6596/219/i=7/a=072020.

[10] CMS Collaboration, *Missing transverse energy performance of the CMS detector* (2011), arXiv:1106.5048.

[11] J. W. F. Valle, Journal of Physics: Conference Series **53**, 473 (2006), http://stacks.iop.org/1742-6596/53/i=1/a=031.

[12] M. E. Peskin and D. V. Schroeder, *An Introduction To Quantum Field Theory (Frontiers in Physics)* (Westview Press, 1995), ISBN 0201503972.

[13] LEP Collaborations: ALEPH Collaboration and DELPHI Collaboration and L3 Collaboration and OPAL Collaboration and the LEP Electroweak Working Group and the SLD Electroweak and Heavy Flavour Groups, *A Combination of Preliminary Electroweak Measurements and Constraints on the Standard Model* (2003), arXiv:hep-ex/0312023.

[14] J. D. Wells, *TASI Lecture Notes: Introduction to Precision Electroweak Analysis* (2005), arXiv:hep-ph/0512342.

[15] A. H. Chamseddine, R. Arnowitt, and P. Nath, Phys. Rev. Lett. **49**, 970 (1982).

[16] L. Randall and R. Sundrum, Phys. Rev. Lett. **83**, 3370 (1999).

[17] L. Randall and R. Sundrum, Phys. Rev. Lett. **83**, 4690 (1999).

[18] M. J. Strassler and K. M. Zurek, Physics Letters B **651**, 374 (2007), ISSN 0370-2693, http://www.sciencedirect.com/science/article/pii/S0370269307007721.

[19] G. Altarelli, B. Mele, and M. Ruiz-Altaba, Z. Phys. **C45**, 109 (1989).

[20] H.-C. Cheng, C. T. Hill, S. Pokorski, and J. Wang, Phys. Rev. D **64**, 065007 (2001).

[21] M. Schmaltz, Journal of High Energy Physics **2004**, 056 (2004).

[22] R. N. Mohapatra and J. C. Pati, Phys. Rev. D **11**, 566 (1975).

[23] R. N. Mohapatra and J. C. Pati, Phys. Rev. D **11**, 2558 (1975).

[24] G. Senjanovic and R. N. Mohapatra, Phys. Rev. D **12**, 1502 (1975).

[25] M. Schmaltz and C. Spethmann, *Two Simple W' Models for the Early LHC* (2010), arXiv:1011.5918.

[26] Y. Zhang, H. An, X. Ji, and R. N. Mohapatra, Phys. Rev. D **76**, 091301 (2007).

[27] R. H. Cyburt, B. D. Fields, K. A. Olive, and E. Skillman, Astroparticle Physics **23**, 313 (2005), ISSN 0927-6505, http://www.sciencedirect.com/science/article/pii/S092765050500006X.

[28] R. Barbieri and R. N. Mohapatra, Phys. Rev. D **39**, 1229 (1989).

[29] K. Hsieh, K. Schmitz, J.-H. Yu, and C. P. Yuan, *Global Analysis of General SU(2) x SU(2) x U(1) Models with Precision Data* (2010), arXiv:1003.3482.

[30] CDF Collaboration, Phys. Rev. D **83**, 031102 (2011).

[31] D0 Collaboration, *Search for $W \to tb$ resonances with left- and right-handed couplings to fermions* (2011), arXiv:1101.0806.

[32] G. Beall, M. Bander, and A. Soni, Phys. Rev. Lett. **48**, 848 (1982).

[33] G. Ecker and W. Grimus, Nuclear Physics B **258**, 328 (1985), ISSN 0550-3213, http://www.sciencedirect.com/science/article/pii/0550321385906169.

[34] D. Chang, Nuclear Physics B **214**, 435 (1983), ISSN 0550-3213, http://www.sciencedirect.com/science/article/pii/0550321383902432.

[35] J. M. Frère, J. Galand, A. Le Yaouanc, L. Oliver, O. Pène, and J. C. Raynal, Phys. Rev. D **46**, 337 (1992).

[36] G. Barenboim, J. Bernabéu, and M. Raidal, Nuclear Physics B **478**, 527 (1996), ISSN 0550-3213, http://www.sciencedirect.com/science/article/pii/0550321396004415.

[37] P. Ball, J. M. Frère, and J. Matias, Nuclear Physics B **572**, 3 (2000), ISSN 0550-3213, http://www.sciencedirect.com/science/article/pii/S055032139900824X.

[38] F. I. Olness and M. E. Ebel, Phys. Rev. D **30**, 1034 (1984).

[39] P. Langacker and S. U. Sankar, Phys. Rev. D **40**, 1569 (1989).

[40] R. H. Cyburt, B. D. Fields, K. A. Olive, and E. Skillman, Astroparticle Physics **23**, 313 (2005), ISSN 0927-6505, http://www.sciencedirect.com/science/article/pii/S092765050500006X.

[41] R. Barbieri and R. N. Mohapatra, Phys. Rev. D **39**, 1229 (1989).

[42] E. Boos, V. Bunichev, L. Dudko, and M. Perfilov, Physics Letters B **655**, 245 (2007), arXiv:hep-ph/0610080.

[43] A. Papaefstathiou and O. Latunde-Dada, Journal of High Energy Physics **2009**, 044 (2009).

[44] T. G. Rizzo, Journal of High Energy Physics **2007**, 037 (2007).

[45] CERN, *LHC: The Guide* (2008), http://cdsweb.cern.ch/record/1092437/files/CERN-Brochure-2008-001-Eng.pdf.

[46] M. L. Mangano, Contemporary Physics **51**, 211 (2010), http://www.tandfonline.com/doi/pdf/10.1080/00107510903367902.

[47] CMS Collaboration, Journal of Instrumentation **5**, T03005 (2010), http://stacks.iop.org/1748-0221/5/i=03/a=T03005.

[48] S. Stapnes, Nature **448**, 290 (2007).

[49] A. Tricomi, The European Physical Journal C - Particles and Fields **33**, s1023 (2004), ISSN 1434-6044, 10.1140/epjcd/s2004-03-1801-1, http://dx.doi.org/10.1140/epjcd/s2004-03-1801-1.

[50] CMS Collaboration, CMS Note 2007/012 (2007).

[51] O. Kortner, *Muon Identification at ATLAS and CMS* (2007), arXiv:0707.0905.

[52] L. Tuura, G. Eulisse, and A. Meyer, Journal of Physics: Conference Series **219**, 072055 (2010), http://stacks.iop.org/1742-6596/219/i=7/a=072055.

[53] W. Badgett, *CMS Online Web-Based Monitoring and Remote Operations* (2007).

[54] T. Sjöstrand, S. Mrenna, and P. Skands, JHEP **2006**, 026 (2006).

[55] J. Alwall, P. Demin, S. Visscher, R. Frederix, M. Herquet, F. Maltoni, T. Plehn, D. Rainwater, and T. Stelzer, JHEP **2007**, 028 (2007).

[56] S. Agostinelli et al., Nucl. Instrum. Meth. A **506**, 250 (2003), ISSN 0168-9002.

[57] R. Hamberg, W. van Neerven, and T. Matsuura, Nucl. Phys. B **644**, 403 (2002).

[58] R. Hamberg, W. van Neerven, and T. Matsuura, Nucl. Phys. B **359**, 343 (1991).

[59] H. Bethe and W. Heitler, Proc. R. Soc. **A146**, 83 (1934).

[60] W. Adam, R. Frühwirth, A. Strandlie, and T. Todorov, Journal of Physics G: Nuclear and Particle Physics **31**, N9 (2005), http://stacks.iop.org/0954-3899/31/i=9/a=N01.

[61] D0 Collaboration, Phys. Rev. D **76**, 012003 (2007).

[62] CMS Collaboration, *Measurement of the Inclusive W and Z Production Cross Sections in pp Collisions at sqrt(s) = 7 TeV* (2011), arXiv:1107.4789.

[63] G. Giacomelli and B. Poli, *Results from high energy accelerators* (2002), arXiv:hep-ex/0202023.

[64] M. J. Oreglia, Ph.D. Thesis **SLAC-R-236** (1980), appendix D.

[65] CMS Collaboration, CMS Physics Analysis Summary JME-09-010 (2009).

[66] CMS Collaboration, CMS Physics Analysis Summary: PFT-09-001 (2009).

[67] CMS Collaboration, CMS Physics Analysis Summary JME-10-005 (2010).

[68] CMS Collaboration, CMS Physics Analysis Summary **CMS-PAS-EWK-10-004** (2010).

[69] CMS Collaboration, Journal of High Energy Physics **2011**, 1 (2011), 10.1007/JHEP05(2011)093, http://dx.doi.org/10.1007/JHEP05(2011)093.

[70] CMS Monte Carlo and Generator Tools Group (2010), https://twiki.cern.ch/twiki/bin/viewauth/CMS/StandardModelCrossSections.

[71] CMS Collaboration, Physics Letters B **695**, 424 (2011), ISSN 0370-2693, http://www.sciencedirect.com/science/article/pii/S037026931001333X.

[72] I. Bertram et al. (D0 Collaboration) (2000), FERMILAB-TM-2104.

[73] Z. Han and W. Skiba, Phys. Rev. **D71**, 075009 (2005), hep-ph/0412166.